SAPIENZA
UNIVERSITÀ DI ROMA

FACULTY OF INFORMATION ENGINEERING, INFORMATICS, AND STATISTICS

PhD Studies in Information and Communication Technologies

Enabling Indoor Internet through Visible Light Communications: when Data bring Light

PhD Candidate
Stefano Pergoloni

Advisor
Prof. Mauro Biagi

XXIX Ciclo

ACKNOWLEDGMENTS

A big thank you to my advisor Prof. Mauro Biagi, who has been a great mentor to me and to Prof. Gaetano Scarano, from whom I have learned a lot. Thanks to Prof. Zabih Ghassemlooy for letting me visit his lab at Northumbria University and to Andy, Navid and Geetika. Thanks to Andrea Petroni, for his friendship and support during the last few years. Thank you Davide, Felice, Danilo, Rosa and Chien for all the time we spent toghether on breaks. A special thank you to my family, I couldn't have made it without them. And Francesca, thank you for your love, encouragement and inspiration.

ABSTRACT

In Visible Light Communications (VLC) there is the opportunity of using the same infrastructure for both providing illumination service and data transmission. As a consequence, a good communication system has to guarantee good illumination quality and, in order to obtain energy saving and deployment cost reduction, the driving circuitry of the communication part should be kept similar to the existing one. At the same time, in order to enable high data rate indoor applications, as well as location based services, due to the limited bandwidth of off-the-shelf Light Emitting Diodes (LEDs), Multiple-Input Multiple-Output (MIMO) techniques should be used, exploiting the high number of LED array present in indoor lighting infrastructure. However the use of spatial diversity techniques can lead to spatial intersymbol interference at the receiver. In this thesis are investigated several research challenges that need to be addressed in order to enabling indoor Internet through VLC. They are: trichromatic modulation techniques which satisfy color rendering constraint, exploiting the metameric property; indoor positioning estimation through an hybrid lateration scheme; MIMO together with a space-time coding technique to provide gains in spectral efficiency; semiblind adaptive spatial equalization to diminish spatial intersymbol inteference when MIMO techniques are used.

Contents

List of Figures

List of Tables

Chapter 1

Introduction

The greed for wireless data has risen considerably in the last few years, especially because, with the rise of new human centric applications, people need to be always connected to the internet, everywhere and at any time. Moreover, the number of devices created with internet connection capabilities is improving, while their costs is going down, enabling what is called the Internet of Things (IoT), paving the way for new services that will improve the quality of everyday life, leading to smarter city, transportation system, health and much more. In addition, what will be the next invention that will drive new connectivity, computing and consumption paradigms, is unpredictable, as it is the future need of data traffic.

For this reasons, for the successful deployment of the next generation of communication infrastructure, namely 5G, there are several challenges to be addressed in order to meet the main engineering requirements (see Fig. 1.1). The most important requisites for 5G are commonly the following: higher system capacity, the ability to serve an higher number of devices, the decrease of the latency and the energy consumption and costs of the network, the improvement of data rate per user, meeting 100 Mbps for 95% of users and having 10 Gbit/s as peck rate.

Fulfilling these requirements will be extraordinarily challenging, but to get an higher improvement in aggregate data rate (bit/s per unit area) the key consists in using more band, considering other frequencies in the upper and lower spectrum and making spatial reuse. That means smaller cells, moving towards heterogeneous networks and deploying distributed low-power and cost-efficient small cells.

Considering these possibilities, Visible Light Communications (VLC), which transmit data by changing the light intensity of ordinary light-emitting diodes (LEDs) in a way that is not perceived by the human eye, can be a powerful complementary technology to the existing radio frequency

(RF) wireless systems. Indeed, VLC is characterized by very small cells (called atto-cells) that can lead to high densification and offloading of the network. Its channel has THz of unregulated and unlicensed band (visible spectrum), and plenty of LED array in indoor lighting infrastructure that, for its transmitting sources directivity, can provide higher data rate densities [$Mbit/s/m^2$] through the spatial reuse. In addition, VLC systems can be used in sensitive environments where conventional radio wave transmission is not allowed, like hospitals and airplanes.

Thanks to advances in solid state lighting, LEDs are foreseen to become the dominant source for general illumination in the near future, because LED is more advantageous than the existing incandescent lamps in terms of long life expectancy, high tolerance to humidity, low power consumption, minimal heat generation lighting and now are becoming increasingly cheaper. Another aspect related to the energy efficiency of VLC systems is the possibility to transmit data while illuminating. Moreover, thinking about IoT, VLC can be used as a communications medium for ubiquitous computing, because light-producing devices (such as indoor/outdoor lamps, TVs, traffic signs, commercial displays, car headlights/taillights, etc.) are nowadays widely present.

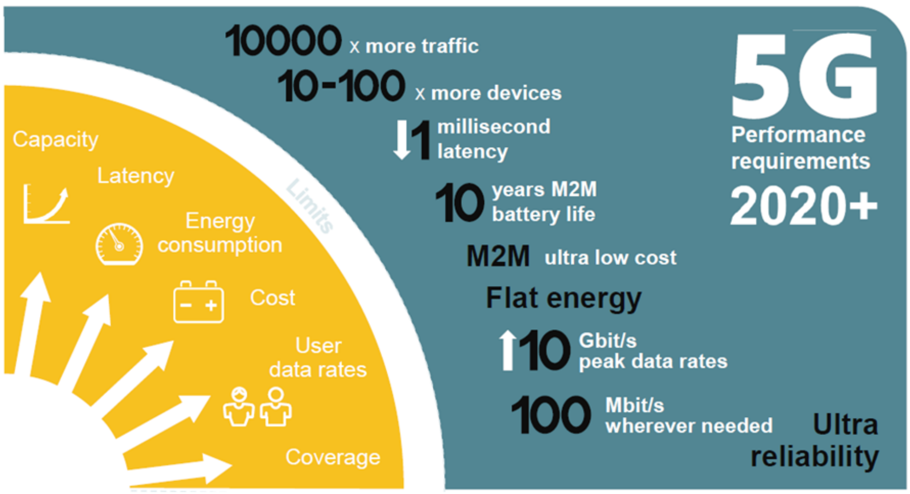

Fig. 1.1: 5G Challenger. Source 5G PPP.

The VLC technology can be adopted for both indoor and outdoor applications. For instance, a typical outdoor application is vehicular-to-vehicular communication, where cars can exchange information about traffic conditions or possible accident event, using their LED-based headlights/taillights. Instead, a typical indoor application is the internet access for mobile users. The topics covered in this thesis deal with indoor environment, even if some analysis can be extended also to outdoor VLC applications.

In the following chapters are addressed different issues regarding VLC communication systems that can be seen as pieces of a single communication system framework.

First of all, it is tackled the problem of having good color quality perception when the transmitting source is composed by trichromatic LEDs (Red, Green, Blue), since the transmitted signal is used for both providing illumination and bringing data. Therefore VLC communication system has to guarantee a sufficient colour rendering quality in the transmitting light.

The LEDs used for indoor lighting and communication can be also used to localize mobile users within a network. Indoor localization is investigated in order to improve the position estimation accuracy and, at the same time, to provide knowledge on how many and which LEDs are able to serve an end-user. The information about the light sources that can reach an end-user, indeed, can also improve the transmission performances when Multiple-Input Multiple-Output (MIMO) schemes are taken into account, especially in large rooms.

For achieving higher energy savings, thanks to the dual use paradigm (illumination & communication), the LED driver used for data transfer should be not so different from the one used for the sole purpose of providing light. In general, in the lighting system, the light control can be performed with either an analog dimming, which changes LED light output by simply adjusting the DC current, or digital dimming with Pulse Width Modulation (PWM) that achieves the same effect by varying the duty cycle of a constant current. Consequently, to reduce the cost of deployment of VLC systems, the use of impulsive modulations, like On-Off Keying (OOK) or Pulse Position Modulation (PPM), should be preferred because they can be easily adapted, with a subtle changes, from PWM.

For this reason, throughout the thesis, are considered impulsive modulations, such as PPM. Moreover such a modulation, which conveys information using delayed pulses, has been extensively used for both positioning and data transmission. PPM is known to be a power efficient modulation, but it is bandwidth inefficient. However, in indoor lighting infrastructure it is usually possible to find a great amount of LEDs arrays, thus bandwidth gain can be obtained with the use of MIMO techniques.

Unfortunately, there is an issue of primary importance that is the spatial intersymbol interference. When it is used a MIMO imaging receiver, as a camera, the interference that rise, due to the optical channel effect, would result in blurred images at the receiver. This issue can drastically decrease the achievable distance of the communication link or worsen the performance when the end-user is in mobility. So to obtain a sufficient low bit error rate (BER) it is necessary to study the spatial equalization at the receiver.

In this thesis the above mentioned research challenges are investigated. The key contributions to knowledge that are derived in this thesis are given from chapter three. The overall thesis is organized as follows:

- In chapter 2 an overview of the main VLC system properties is given, with a brief introduction on human image perception and how this affects the engineering design of the communication system; then the fundamental blocks of the VLC communication link are shown and discussed, highlighting the main difference in comparison with RF.

- In chapter 3 a modulation technique that uses trichromatic LEDs is investigated, taking into account the metameric property; in the second part of the chapter it is studied how colors, belonging to the same source, interfere with each other.

- In chapter 4 indoor users localization through visible light is studied, an hybrid lateration scheme is presented, with a brief discussion on atto-cells coverage aspects.

- In chapter 5 a MIMO PPM block coding scheme under the constraint of matrices to be trace orthogonal is studied, compared with other competitor schemes. The presented MIMO scheme can be used in the same framework of the localization task presented in chapter 2.

- In chapter 6 optical camera communication systems, a subgroup of VLC, are introduced; after explaining this systems main features, the spatial intersymbol interference issue is addressed, and the use of a semiblind adaptive spatial fractionally spaced equalizer, which takes into account the high number of receiving elements present in cameras, *i.e.* high number of pixels, is investigated.

Chapter 2

Visible Light Communication Principles

As early mentioned in the Introduction, VLC systems can provide wireless data transmission through the use of the visible spectrum. The wavelengths producing the visible light are those ranging from 350 nm to 780 nm (Fig. 2.1). The peculiarity of this part of the electromagnetic spectrum is to have waves with the ability of activate photoreceptor in the human cornea. This characteristic allows people to perceive the (light) signal behaviour, even if, as it is explained later in this chapter, the perception of the signals is limited by physiological constraints of the human eye.

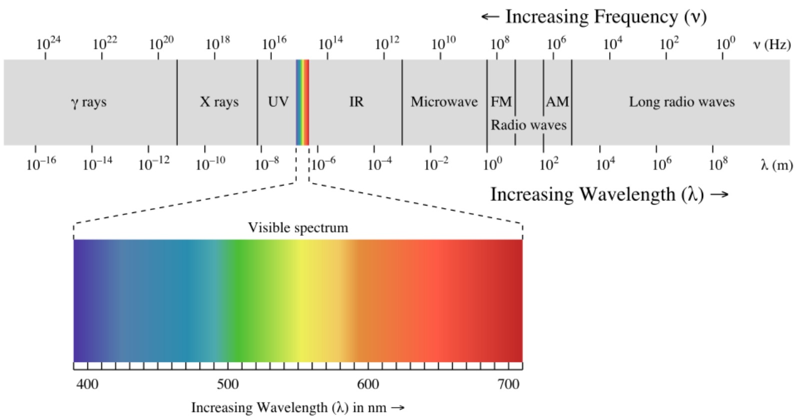

Fig. 2.1: EM spectrum

Over the last three centuries, two main theories have been raised with the aim of investigating the nature of light. The first was initially studied by Sir. Isaac Newton (1642 - 1727), who believed that the light was essentially a stream of tiny particles, later on called photons. This theory was in contrast with the wave theory of light of Christiaan Huyghens (1629 - 1695).

In the history of light investigation, an important experiment was carried out in 1807 by Thomas Young demonstrating the wave nature of light. This Young's interference experiment showed that lights (waves), passing through two slits (double-slit), add together or cancel each other and then interference fringes appear. This phenomenon cannot be explained unless light is considered as a wave. But at the start of the 20th century, became evident that the wave theory was unable to explain all the light phenomena. In 1905 Albert Einstein (1879 – 1955) succeeded in explaining the photoelectric effect which had been unexplainable if one only considers light as a wave. It is now believed that light is at the same time constituted by particles and waves, thus the wave-particle duality of photons.

This chapter gives an overview of the basic principles of VLC systems, trying to emphasize the most important aspects that this technology introduces, starting off with fundamental human vision characteristics, which are deeply related to the communication aspects and impose strong constraint on (light) signals transmission.

2.1 Image Perception

Many information reaches the eye, but along the path through the brain a lot of it is lost due to limits of human sensors. In other words the information gathered via the eye has poor-quality. The vision perception is the ability to interpret the surrounding environment by processing those poor-quality information data. Following the studies of Hermann von Helmholt (1821 – 1894), the vision is a result of some form of unconscious inferences: a matter of making assumptions and conclusions from incomplete data, based on previous experiences, a decision-making process of intellectual type, based on a limited sensory evidence [12]. Sensory signals are not suitable to get immediate perceptions; to see objects the intellect has to make a number of conjectures.

The human sensory limitations have been extensively exploited in source coding and compression, with application to all different fields of information and communication technologies in order to create a more efficient way to represent the information, *i.e.* for reducing the size of the data to be transmitted or stored. For instance, the incomplete data analysis performed by the eye is widely used in the lossy compression method for digital images, the JPEG, in order to discard the information linked to higher spatial frequency of an image.

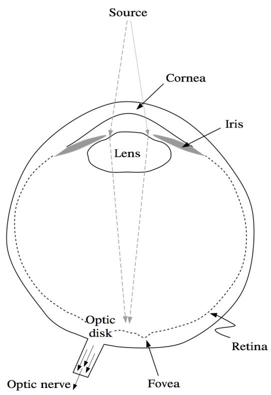

Fig. 2.2: The imaging components of the eye.

How are perceptual information represented quantitatively? To answer to this question, first of all are investigated the sensors composing the eye, the photoreceptor, which are rods and cones contained in the retina (see Fig. 2.2). The rods provide scotopic vision, the cones instead provides photopic vision, which is the visual response at a higher illumination level. In comparison to the scotopic vision the difference in the illumination levels has 5-6 orders of magnitude.

For studying VLC system, an important quantity is the relative luminous efficiency function of the visual system, reported in Fig. 2.3. From this can be written the relation among illuminance and the transmitted power of a VLC solid state light. In fact, the luminous intensity is given as:

$$I = \frac{d\Phi}{d\Omega} \tag{2.1}$$

where Ω is the spatial angle, and Φ is the luminous flux, which can be given from the energy flux Φ_e as:

$$\Phi = K_m \int_{380}^{780} V(\lambda)\Phi_e(\lambda)d\lambda \tag{2.2}$$

where $V(\lambda)$ is the standard luminosity curve, K_m is the maximum visibility, which is about $683lm/W$ at $\lambda = 555nm$.
The integral of the energy flux Φ_e in all directions is the transmitted optical power P_t, given as:

$$P_t = \int_{\lambda_{min}}^{\lambda_{max}} \int_0^{2\pi} \Phi_e d\theta d\lambda \tag{2.3}$$

where λ_{min} and λ_{max} are determined by the sensitivity curve of the photodiode.

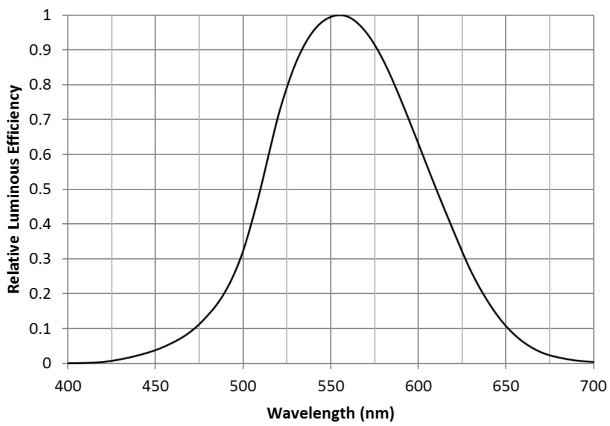

Fig. 2.3: Relative luminous efficiency function.

2.1.1 Temporal Properties of Vision

An extensive survey on the temporal sensitivity of the human eye can be found in [13]. Here, are introduced only few aspects, which are the most important for a better understanding of the theoretical investigation carried out in the next chapters.

In order to produce stable images of the environment, the human eye has an integration time during which it sums up all the samples of information reaching the eye. For instance, two flashes of light can be fused in one if the distance, in time, among them is smaller than this integration time.

In this regard, Critical Fusion Frequency (CFF) is the frequency at which visual rapidly repeated stimulus are perceived as a continuous source. In other words, if the light flashes at rates above CFF, it is indistinguishable from a steady light of the same average intensity. A threshold level for CFF is 50- 60 Hz as can be seen in Fig. 2.4. The CFF value explains the refreshing rates used for displaying images in TV screen and monitor, which is of 60 frames/s. From Fig. 2.4 it is possible to see how this threshold frequency varies also with the level of luminance. Moreover, the eye is more sensitive to flickering of high spatial frequencies [14]. A related, interesting property is the temporal law of summation, *i.e.* Bloch's law, which states that the total luminous energy is a constant value, that is the product of luminance and stimulus duration.

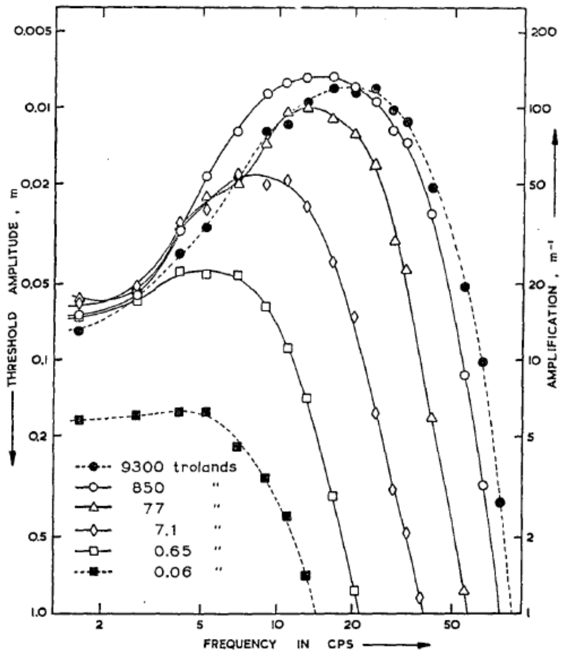

Fig. 2.4: Relative amplitude sensitivity versus modulation frequency for various adaptation levels.

2.1.2 Colorimetry

In the experiment carried out by Newton, the spectrum, obtained by refracting light through a prism, shows a number of characteristic regions with color red, orange, yellow, green, blue, indigo, and violet. Color representation is based on the classical theory of Thomas Young (1773 – 1829) that any color can be reproduced by mixing an appropriate set of three primary colors. The cones are also responsible for color vision. In the human eye there are three receptors, three type of cones, each one especially sensitive to one part of the spectrum; the three sets of cones are named short (S), medium (M) and long (L). In Fig. 2.5 it is shown the typical photon normalized absorbency of the three cones, each one with its own peak response. Different wavelengths of the light are absorbed differently by the rods and the three sets of cones. In this sense it can be seen as a wavelength selective filter weighting differently the various wavelengths of light.

Optical stimulus with a spectral power distribution (SPD) $C(\lambda)$ will induce optical sensation α_S, α_M and α_L within the cones as follows [15]:

$$\alpha_i = \int_0^\infty C(\lambda) S_i(\lambda) d\lambda. \tag{2.4}$$

Colors with different spectral power distributions can appear chromati-

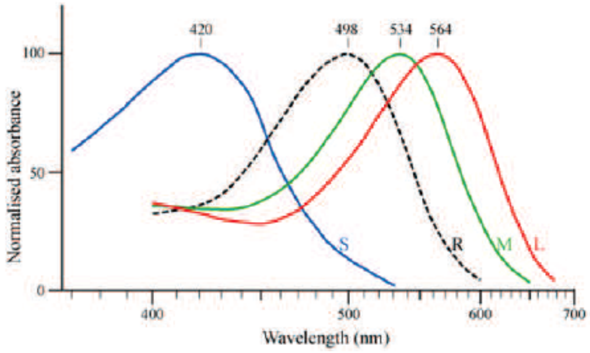

Fig. 2.5: Normalized absorbance of Rods and Cones.

cally identical to the human eye. In fact if

$$\alpha_i(C_i) = \alpha_i(C_2) \qquad i = 1, 2, 3$$

then the two color C_1 and C_2 even if can appear identical, they have different spectral distribution.

Colors are reproduced using a set of light sources, typically three, in order to match with the three receptor model of the eye. Every light source is characterized by a spectral power distribution $P_k(\lambda)$, $k = 1..., 3$, normalized in order to have unity power:

$$\int P_k(\lambda) d\lambda = 1$$

Indicating with β_k the power that drives the k-th light source, controlling the mixing proportion, then the produced color is obtained as

$$R(\lambda) = \sum_{k=1}^{3} \beta_k P_k(\lambda)$$

Given an arbitrary color spectral distribution $C(\lambda)$, it is possible that modifying the amount of β_k for the three sources, different set of combination provides the same color sensation $R(\lambda)$ to the human eye, *i.e.* $C(\lambda)$ and $R(\lambda)$ are visually indistinguishable.

Considering the human eye cone response, color matching equations are written as:

$$\sum_{k=1}^{3} \beta_k a_{i,k} = \alpha_i(C) = \int S_i(\lambda) C(\lambda) d\lambda$$

where $a_{i,k}$ is the i-th cone response generated by one unit of the k-th primary.

The metameric matching can be written also as:

$$C(\lambda) \sim \sum_{k=1}^{3} \beta_h(C) P_k(\lambda)$$

Where the operator $\sim$ indicates metameric equivalence.

Another normalization is necessary and it is provided with the calibration of the three primary sources against a reference white light with known spectral power distribution $W(\lambda)$

$$W(\lambda) \sim \sum_{k=1}^{3} \beta_h(W) P_k(\lambda)$$

thus, applying the normalization $T_k(C) = \beta_(C)/\beta_k(W)$, the color matching equation becomes:

$$C(\lambda) \sim \sum_{k=1}^{3} T_k(C) \beta_k(W) P_k(\lambda)$$

where $T_k(\lambda)$ are called the spectral tristimulus values. Given $T_k(\lambda)$, the tristimulus values of an arbitrary color $C(\lambda)$ are calculated as [16]:

$$T_k(C) = \int C(\lambda) T_k(\lambda) d\lambda$$

2.2 VLC History

Transmitting information using light has a long history, indeed the first system employing optical wireless transmission can be considered the one used by ancients Greeks and Romans, around 800 BC, which used fire beacons for signalling. More advanced signalling techniques, such as the semaphore, were used by the French sea navigators in 1790s [17]. But what can be termed as the first optical communication in an unguided channel was the photophone experiment by Alexander Graham Bell. On June 3, 1880, Bell's assistant transmitted a wireless voice telephone message from the roof of the Franklin School to the window of Bell's laboratory, about 213 meters away. Data were transmitted by the use of a plane mirror of flexible material, against the back of it the speaker's voice was directed. The mirror becomes alternatively convex and concave under the action of the voice and thus alternatively scatters and condenses the light. The brightness of a reflected beam of light, observed at the receiver side, is related to the

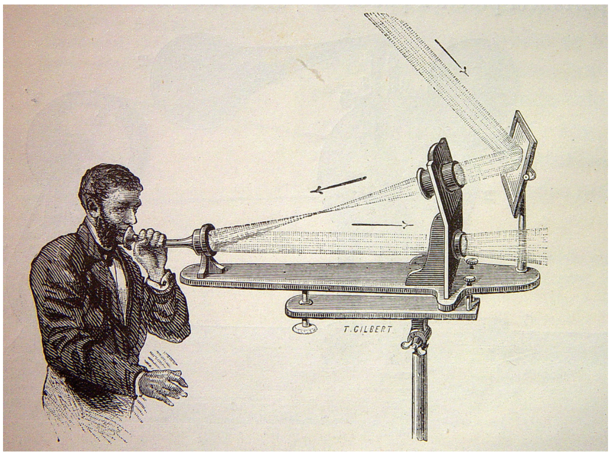

Fig. 2.6: Illustration of a photophone transmitter, showing the path of reflected sunlight, before and after being modulated.

audio-frequency variations in air pressure. Bell believed the photophone was his "greatest achievement".

A ground-breaking innovation for optical wireless communications happened in $1960s$, with the discovery of optical sources like lasers and LEDs. Following this innovation, several free space optics demonstrations was established in the $1960s$. Some of these included the spectacular transmission of television signal over a 48 Km distance using GaAs LED by researchers working in the MIT Lincolns Laboratory in 1962; the first TV-over-laser demonstration in March 1963 by a group of researchers working in the North American Aviation. The first laser link to handle commercial traffic was built in Japan by Nippon Electric Company (NEC) around 1970 [17].

Instead, solid state lighting for illumination purpose has a relatively short history. In the $1990s$, there was the introduction of high-brightness LEDs for general illumination. Within only a few years, LED's luminous efficacy has improved rapidly from less than 0.1 lm/W to over 230 lm/W and with a lifetime as high as $100,000$ h. This aspect helps the growth of LEDs as the main candidate as efficient source of illumination of the present years.

The Nakagawa Laboratory, in Keio University, Japan began work on VLC in 2003. Since then there have been numerous research activities focussed on VLC.

In June 2007, the Japan Electronics and Information Technology Industries Association (JEITA) issued two visible light standards, JEITA $CP-1221$ and JEITA $CP-1222$, based on Visible Light Communication Consortium (VLCC) proposals. In October 2008, the VLCC started cooperation with the Infrared Data Association (IrDA) and the Infrared Communication Systems Association (ICSA). In March 2009, a VLCC specification standard adopting and expanding the IrDA physical layer was announced. A standard for VLC local area network (LAN) based on full duplex by the aid of wavelength-division multiplexing (WDM) (IR and visible) is being pursued by the ICSA.

In early 2009, the task group IEEE 802.15.7 was working on a VLC standard encompassing both new physical and medium access control (MAC) layers. In November 2010 the P802.15.7 IEEE draft standard was published [18]. In July 2011 a live demonstration of high definition video being transmitted from a standard LED lamp was shown at TED Global. Recently the IEEE 802.15 has formed a task group to write a revision to IEEE 802.15.7-2011 that accommodates infrared and near ultraviolet wavelengths, in addition to visible light, and adds options such as Optical Camera Communications (OCC) which enables scalable data rate, positioning/localization, and message broadcasting using devices such as the flash, display and image sensor as the transmitting and receiving devices.

2.3 VLC System Model

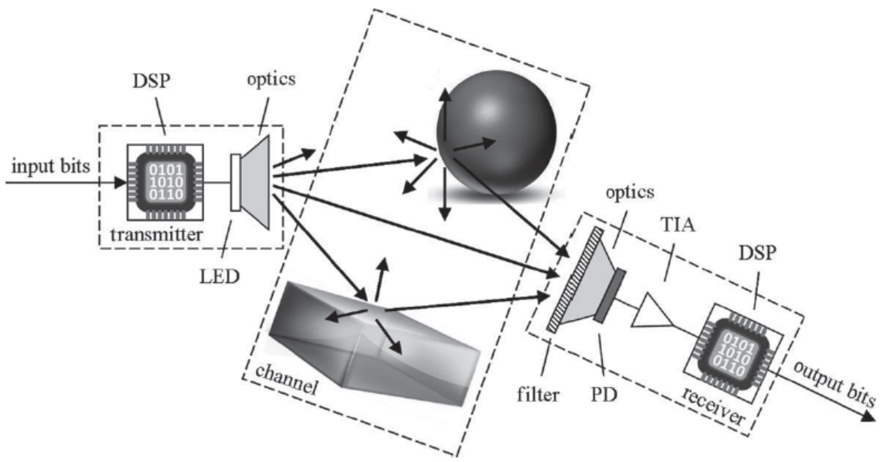

Fig. 2.7: Transmission link in VLC [1].

The general communication link of a VLC system is represented in Fig. 2.7. The lighting source, the optical wireless channel and the photo detector represent the fundamental blocks. For the applications that are relevant to this thesis, the light source adopted are LEDs, since they have lower cost and relaxed eye safety regulations in comparison to Lasers.

The transmission technique used in VLC is intensity modulation with direct detection (IM/DD). This incoherence method is used principally for its simplicity and lower cost of implementation in comparison to coherence schemes usually adopted in guided fibre optics.

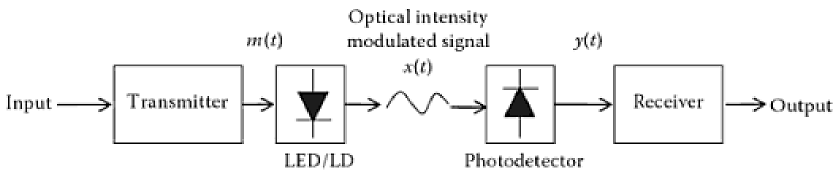

Fig. 2.8: Block diagram of an optical intensity, direct detection communication channel.

In IM/DD systems, the drive current of the optical source is directly modulated by the modulating signal $m(t)$, which in turn varies the intensity of the optical source $x(t)$. The response of a photodetector is the integration of tens of thousands of very short wavelengths of the incident optical signal, that generates a photocurrent $y(t)$ [17]. This is directly proportional to the instantaneous optical power incident on it, that is proportional to the square of received electric field, whose expression is:

$$y(t) = RA_e x(t) * h(t) + n(t), \tag{2.5}$$

where R [A/W] is the responsivity of the photodiode, A_e [m^2] is the effective receiver area, $h(t)$ is the baseband channel impulse response and $n(t)$ is the noise, modelled as the additive white Gaussian noise (AWGN) with a double-sided power spectral density (PSD) of $N_0/2$.

In VLC, as in any optical wireless communication system, the noise is the result of several types of interference. Among these, the shot noise, produced by the ambient light, and the thermal noise, arisen in the transimpedance amplifier (TIA), dominate the additive noise at the receiver. The high intensity shot noise is the result of the summation of many independent, Poisson distributed random variables. The cumulative distribution approaches a Gaussian distribution, resulting, as anticipated, in Additive White Gaussian Noise (AWGN). The noise power spectral density is [19]:

$$N_0 \cong N_{shot} = 2qRP_n \sim 10^{-22} A^2/Hz \tag{2.6}$$

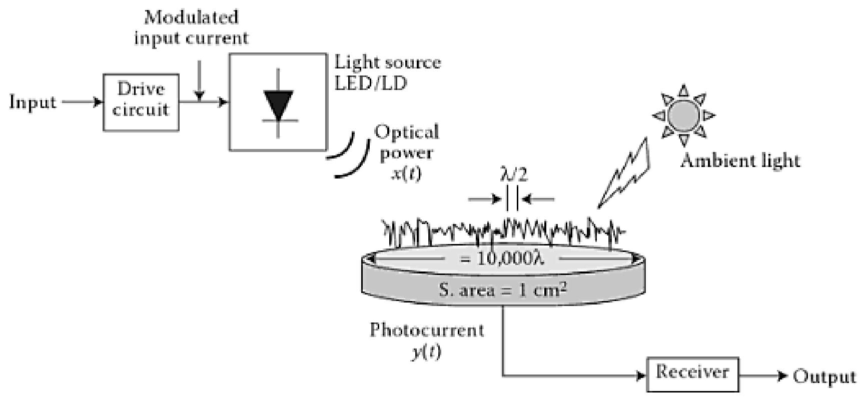

Fig. 2.9: Equivalent baseband model.

where q is the electronic charge and P_n is the average power of ambient light.

About the impact of different factors, A_e depends on the actual photodiode area, the angle of light incidence, and the concentrator used [3], [20]. Also, the responsivity R varies with the color spectrum of the light that is incident on the photodiode surface, which in turn depends on the spectrum of the LED source, as well as on any color filter used at the receiver[17].

One substantial difference of optical wireless systems over the RF ones is the absence of multipath fading. Even if the effects of multipath propagation in non line of sight (LOS) links can be the same of RF systems, and the link can suffer from severe propagation multipath, it causes the electric field to suffer from intense amplitude fades on the scale of a wavelength. The detector would experience multipath fading only if the detector size is proportional to the wavelength of the transmitted signal. Fortunately VLC receivers use detectors with a surface area typically millions of square wavelengths. The total photocurrent generated is proportional to the integral of the optical power over the entire photodetector surface, as can be seen in Fig. 2.9. Due to the high spatial diversity at the receiver, there is no fast fading, but only slow fading that appear in the form of shadowing. Indoor VLC links do not suffer from the effects of multipath fading, but they do suffer from the effects of dispersion, which manifests itself in a practical sense as the intersymbol interference (ISI). For sufficiently low rates, *i.e.*, bit/s of the order of few Mb/s, the channel is close to be ideal, while for higher rates, the signal distortion becomes important and not negligible, since it may cause inter-pulse (and/or inter-symbol) interference. A very good short-hand predictor of optical link performance in the presence of distortion is Root Mean Square (RMS) delay spread of the response $h(t)$. The delay spread of dispersive optical wireless channels can be modelled by a rapidly decaying exponential impulse response function. The typical values for the RMS delay spread are between 1.3 ns and 12 ns for LOS link, instead for non LOS (NLOS) links the values are between 7 ns and 13 ns [1]. The channel characteristic of a VLC link is fixed for a given position of transmitter, receiver and intervening reflecting objects, hence the channel characteristic only changes when these components are moved by distances of the order of centimetres.

Optical wireless systems differ from electrical or radio systems since the istantaneous optical power is proportional to the generated electrical current. $x(t)$ represents the power rather than the amplitude signal. This imposes two constraints on the transmitted signal:

- $x(t)$ must be nonnegative, $x(t) \geq 0$;
- the eye safety requirements limits the maximum optical transmit power that may be used.

Than the eye safety lead to limit the average power, hence the average value of $x(t)$ must not exceed a specified maximum power value P_{max}. This is in contrast to the time-averaged value of the signal $|x(t)|^2$, which is the case for the conventional RF channel when $x(t)$ represents amplitude.

These differences have a profound effect on the system design. On conventional RF channels, the signal-to-noise ratio (SNR) is proportional to the average received power, whereas on optical wireless links, it is proportional to the square of the average received optical signal power given by:

$$SNR = \frac{R^2 H^2(0) P_r^2}{R_b N_0} \tag{2.7}$$

In Tab.2.1 a comparison between RF and VLC system is reported.

Table 2.1: Comparison between RF and VLC systems.

	RF	VLC
Bandwidth	Regulated	Not Regulated
Multipath Fading	Present	Not Present
Input $x(t)$ represents	Amplitude	Power
Average power proportional to	$\int \vert x(t)\vert^2 dt$	$\int \vert x(t)\vert dt$

Thus, in optical systems relatively high optical transmit power are required, and only a limited path loss can be tolerated. Having a limited average optical transmit power indicates that in VLC systems are preferred modulation techniques with a high peak-to-mean power ratio. This is generally achieved by trading off the power efficiency against the bandwidth efficiency.

2.3.1 Link Configuration

Six different indoor link configurations have been defined by Kahn and Barry in [3] and are classified according to the existence of a LOS between the transmitter and the receiver as well as the degree of directionality, that is, source beam-angle and detector field of view (FOV). In [3], the authors classify the link according to two main criteria.

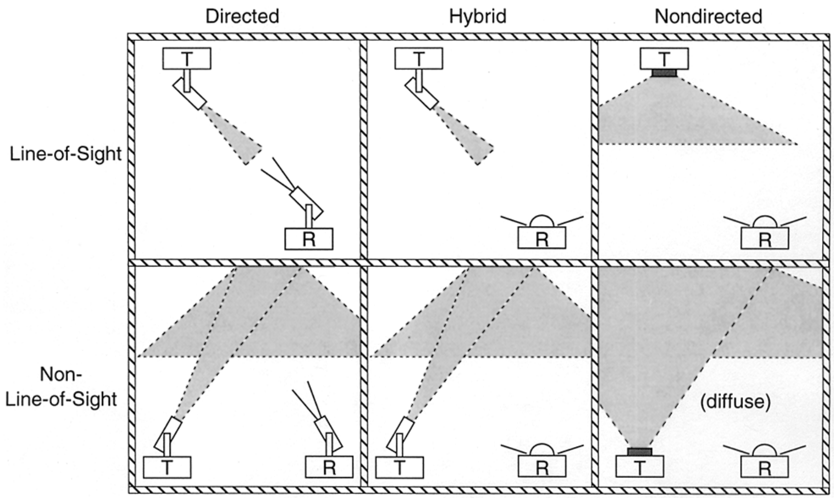

Fig. 2.10: Classification of simple OWC links according to the degree of directionality of the transmitter and receiver and whether the link relies upon the existence of a LOS path between them

The first criterion is the degree of directionality of the transmitter and receiver. Directed links employ directional transmitters and receivers, which must be aimed in order to establish a link, while nondirected links employ wide-angle transmitters and receivers, alleviating the need for such pointing. Directed link design maximizes power efficiency, since it minimizes path loss and reception of ambient light noise. On the other hand, nondirected links may be more convenient to use, particularly for mobile devices, since they do not require the alignment of the transmitter an the receiver. It is also possible to establish hybrid links, which combine transmitters and receivers with different degrees of directionality.

The second classification criterion relates to whether the link relies upon the existence of an uninterrupted LOS path between the transmitter and receiver. LOS links rely upon such a path, while non-LOS links generally rely upon reflection of the light from the ceiling or some other diffusely reflecting surface. LOS link design maximizes power efficiency and minimizes multipath distortion. Non-LOS link design increases link robustness and ease of use, allowing the link to operate even when barriers, such as people or cubicle partitions, stand between the transmitter and the receiver. The greatest robustness and ease of use are achieved by the nondirected-non-LOS link design, which is often referred to as a diffuse link.

The three main case of interest for channel modelling, for the next chapters, are the follows:

1. *Directed LOS channel* (*LOS*), with attenuation but negligible multipath component. This type of channel occurs with short distance LOS links (around tens of centimeters), [21];

2. *Non-Directed LOS channel* (*ND-LOS*), with LOS component but also significant delayed components due to reflected secondary paths. The energy is spread over time, resulting in a reduction of the converted current at the photodiode. This scenario matches well with a transmission at $1-2$ meters so the diversity gain is expected to be higher than that of *LOS*;

3. *NLOS channel or diffuse* (*NLOS*), with no LOS paths due to shadowing. The link relies on collecting only the reflected paths, leading to intersymbol and inter-pulse interference.

2.3.2 Sources

In VLC the source is represented by LEDs, which, as the acronym implies, is a source of semiconductor light. Two important factors characterise LEDs illumination: color rendering index and luminous efficiency.

The color rendering index is a measure of the capacity of the LED to produce color compared to an ideal light source. The luminous efficiency, instead, is the measure of the efficiency with which the source produces visible light from electricity, that is equal to the luminous flux to the total electric power ratio. As electrical power is considered the total consumed by the source, then the unit of measure is lumens per watt.

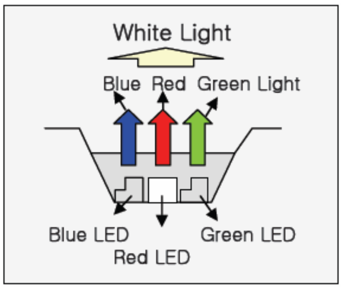

Fig. 2.11: RGB LED

LEDs devices produce white light suitable for lighting and data modulation. Generally, LEDs generating white light are classified into two types: trichromatic and blue-chip phosphor coated LEDs.

One easy way to generate white light is to mix colors Red, Green and Blue (RGB) with suitable portions as shown in Fig. 2.11. The LEDs produced in this way are often referred as RGB LEDs or trichromatic one. These LEDs have the flexibility to mix different colors and have a greater light efficiency (more than 90) compared to LEDs phosphorus, discussed later. However, they have been quite expensive so far.

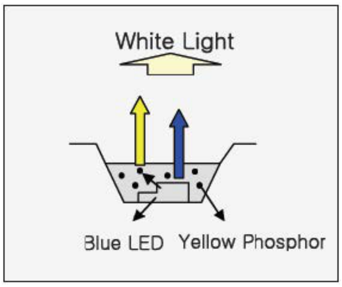

Fig. 2.12: Phosphor LED

The phosphor-based LEDs can be used as alternative to the RGB counterpart. This method involves the coating of a blue LED with a yellow phosphors (Fig. 2.12).

The phosphor-based LED has a lower luminous efficacy compared with RGB LED (about 80) due to problems related to the degradation of the phosphor. However, most of the white LEDs which are now in commerce are realized using this technology. In addition to the advantage of requiring just a single color, these types of LEDs are easier to design and are less expensive than RGB.

The modulation bandwidth available of these LEDs can be improved by at least an order of magnitude through the blue filtering. Due to the

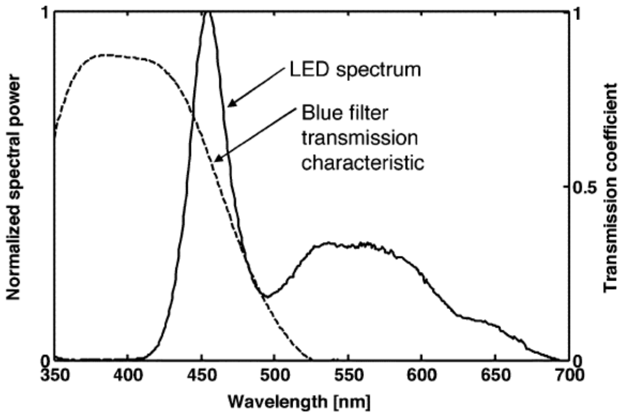

Fig. 2.13: Measured radiation spectrum of a phosphorescent white-light LED together with the transmission characteristic of the used blue filter

long decay time of the phosphor, the modulation bandwidth of the white emitter is limited to about 2 Mhz. On the other hand the blue component has a modulation bandwidth larger than the white one, about 20 Mhz (as shown in Fig. 2.14). Therefore, to obtain a bandwidth modulation larger and thus more data-rates, a common method is to detect just the blue part of the spectrum to the receiver, with a blue filter.

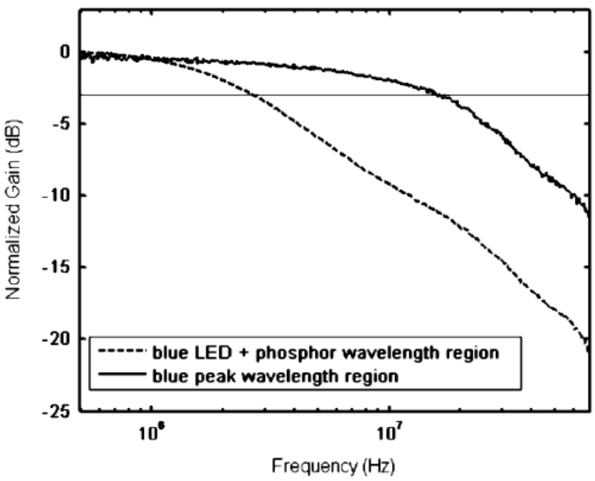

Fig. 2.14: Measured modulation spectrum of a phosphorescent white-light LED. The gain represents the electrical gain of the detector. The solid horizontal line tags the 3-dB modulation bandwidth

For both technology, the LED radiation characteristic is generally modeled by means of a generalized Lambertian radiation pattern [22]. A VLC transmitter can be formed by a single LED or an array of LEDs. This latter solution provides a higher radiant intensity in a given direction, when their radiation patterns are constructively aligned [?], however the intensity cannot exceed a threshold level imposed by the standard for photo biological safety of lamps and lamp systems (EN 62471). Fortunately, incoherent diffuse continuous-wave-modulated LEDs, differently from infrared emitters, have a loose constraint on photo biological hazard for the human eye.

2.3.3 Optical Channel

The optical wireless channel is a linear, time-invariant, memoryless system with finite impulse response. The characterization of a communication channel is performed by its impulse response, which is then used to analyse and combat the effects of channel distortions.

The power penalties directly associated with the channel may be separated into the optical path loss and multipath dispersion. For directed LOS configuration (Fig. 2.10) the reflections does not need to be taken into account. In a non LOS configuration (Fig. 2.10 diffuse system) the reflections off the room surfaces and furniture are also considered, these could be seen as unwanted signals or multipath distortions which make the prediction of the path loss more complex.

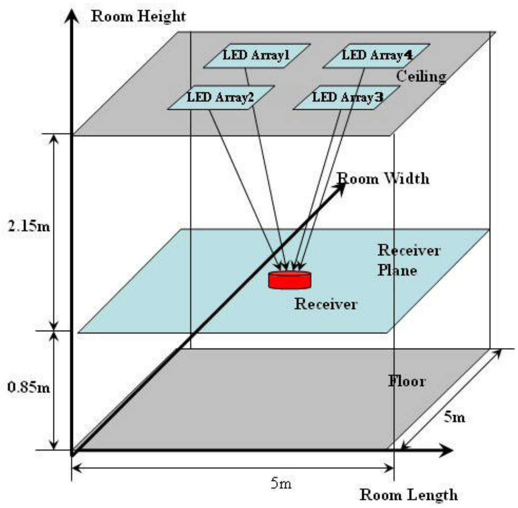

Fig. 2.15: A visible-light indoor optical wireless system utilizing LEDs [2]

The frequency responses of optical wireless channels are relatively flat near DC, so the majority of purposes, the more interesting quantity characterizing a channel is the DC gain $H(0)$, which relates the transmitted and received average powers via $P_r = H(0)P_t$.

The optical wireless channel transfer function is defined by

$$H(f) = H_{LOS} + H_{DIFF}(f) \tag{2.8}$$

In LOS links (either directed, hybrid, or nondirected), the DC gain can be computed fairly accurately by considering only the LOS propagation path that is:

$$H(0)_{LOS} = \begin{cases} \frac{A_{rx}}{d^2} R_0(\phi) cos(\psi), & 0 \leq \psi \leq \psi_c \\ 0, & \psi > \psi_c \end{cases} \tag{2.9}$$

Where A_{rx} is the detector area, d is the distance between the transmitter and the receiver, ψ is the angle of incidence, ψ_c is the FOV of the photodiode, and $R_o(\phi)$ is the transmitter radiant intensity given by:

$$R_o(\phi) = \frac{m+1}{2\pi} cos^m(\phi) \tag{2.10}$$

where m is the order of Lambertian emission, and is related to $\phi_{1/2}$, the transmitter semi-angle(at half power) as $m = -ln_2/ln(cos\phi_{1/2})$. This approximation is particularly accurate in directed-LOS links. The total power of i LEDs in the directed path is:

$$P_{rx,LOS} = \sum_{i=1}^{LEDs} P_{tx} H(0)^i_{LOS} \tag{2.11}$$

where $H(0)^i_{LOS}$ is the i-th LED channel DC gain.

For characterizing the diffuse component alone, the properties of the channel are found using Ulbricht's integrating sphere [19].
The first diffuse reflection of a wide-beam optical source emits a intensity I_1 over the whole room surface A_{room} is given by

$$I_1 = \rho_1 \frac{P_{total,LED}}{A_{room}} \tag{2.12}$$

where ρ_1 is the reflectivity of the surface and $P_{total,LED}$ is the total power of all the LEDs.

The average reflectivity $< \rho >$ is defined as

$$< \rho >= \frac{1}{A_{room}} \sum_i A_i \rho_i \tag{2.13}$$

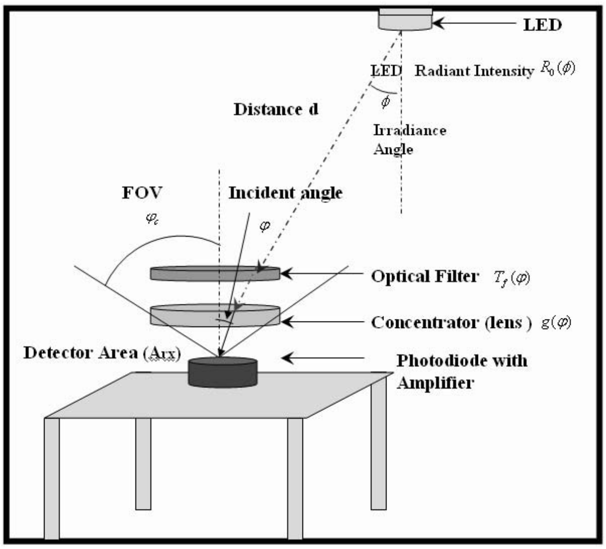

Fig. 2.16: Wireless system utilizing one LED

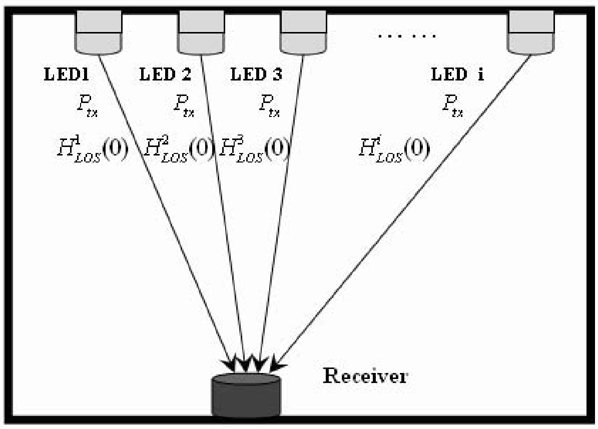

Fig. 2.17: System model with LED arrays

where the individual reflectivity $< \rho >$ of walls, windows and other objects in the room are weighted by their individual areas A_i.

Therefore, the total intensity is given by summing up a geometrical series

$$I = I_1 \sum_{j=1}^{\infty} < \rho >^{j-1} = \frac{I_1}{1 - < \rho >} \tag{2.14}$$

where the index j is the number of reflections.

The receiver is assumed as a small part of the room surface, so the received diffused power P_{diff} with the receiving area A_{rx} is

$$P_{diff} = A_{rx} I \tag{2.15}$$

Therefore, the diffuse channel loss is

$$\eta_{diff} = \frac{P_{diff}}{P_{totalLED}} = \frac{A_{rx}}{A_{room}} \frac{\rho_1}{1 - \rho} \tag{2.16}$$

A very good short-hand predictor of optical link performance in the presence of distortion is RMS delay spread of the optical impulse response, in fact, exist an inverse relation between the channel delay spread and the channel bandwidth. Another interesting aspect is related to the path loss and the reflective geometry of the propagation scenario, since when there is a high reflectivity, it is likely that there is a low path loss at receiver, however it means that the power of rays coming from different propagation path is higher, thus high delay spread and low channel bandwidth it is expected.

LOS and NLOS optical wireless channels can be modeled by a rapidly decaying exponential impulse response function. The 3-dB coherence bandwidth of the channel can be expressed from the RMS delay spread and values between $1.3ns$ and $12ns$ are reported for LOS links, while for NLOS links are between $7ns$ and $13ns$.

2.3.4 Receiver

The VLC receiver is composed of receiving optical elements including lens and optical filter, photodiode, amplifier, and signal recovery circuit (Fig. 2.18).

A single photodiode has a detection characteristic that is generally modeled by mean of a Lambertian detection pattern. In the selection of a suitable photodiode for a VLC communication system, it is important to take into account that using one with large detecting area it is possible to collect more radiated signal optical power, however it reduces the electrical modulation bandwidth. To mitigate this trade-off it is possible to use an array of photodiode, improving the system cost. The receiver optical spectral response is the result of the spectral response of photodiode and the optical filters. For a photodiode it is given by the responsivity:

$$R = \frac{I_p}{P_p} \tag{2.17}$$

where I_p is the average photocurrent generated and P_p is the incident optical power. The responsivity of the photodiode depends on the physical structure of the photodiode and it is expressed in units of amperes per watt of incident radiant optical power. Typical maximum responsivity values are within the range of 0.6-0.8 A/W, and typically the spectral range goes from 320 to 1100 nm, for this reason optical filters are usually employed to separate the different spectral components transmitted. The receiver has an electrical bandwidth that is larger than the electrical bandwidth of the transmitter, in fact, for usually it is in excess of 100 MHz [1]

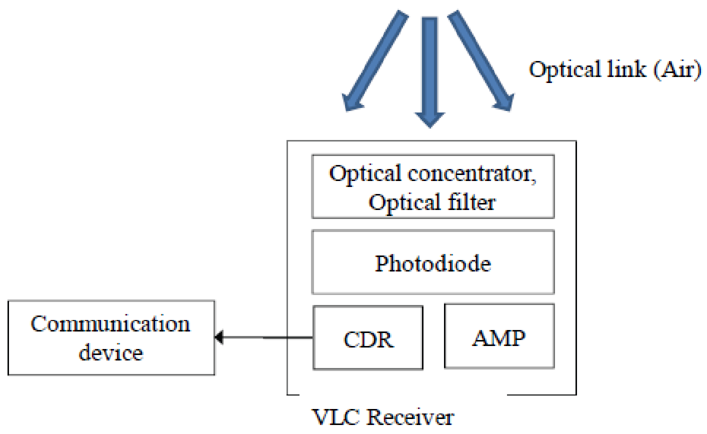

Fig. 2.18: VLC Receiver (CDR: clock and data recovery, AMP: amplifier)

2.4 Challenges and Opportunities

To take full advantage from VLC some research challenges need to be addressed, as the limited bandwidth and slow modulation response of LEDs, and the achievable transmitting distance limited due to the sharp decrease in illumination with distance. Moreover, the use of the visible spectrum implies certain challenges, such as the background noise and the reflections from other light sources like the sun or the fluorescent lamps, which interfere at the receiver side. However, at the same time, the frequency of the visible light spectrum is very high and it has the potential to achieve an enormous data capacity, even if it is not yet possible to exploit this capacity with suitable electronics.

VLC can be used in various interesting application areas, as: [23]:

- **Smart Lighting**

VLC provides the infrastructure for illumination, control and communications and will greatly reduce wiring and energy consumption within a building.

- **Mobile Connectivity**

By pointing a visible light at another device it is possible to create a very high speed data link with inherent security. This overcomes the problems of having to pair or connect and provides a much higher data rate than Bluetooth or WiFi.

- **Hazardous Environments**

Communicating in areas where there is risk of explosions can be a problem (e.g. in mines, petro-chemical plants, oil rigs etc.) . VLC is inherently safe and provides both safe illumination and communications.

- **Vehicle and Transportation**

Many cars already have LED lamps. Traffic signage, traffic lights, and street lamps are adopting the LED technology, so there are massive application opportunities in this field.

- **Defence and Security**

The ability to send data quickly and in a secure way is the key to many applications. The fact that the visible light cannot be detected on the other side of a wall had great security advantages.

- **Hospitals and Healthcare**

There are advantages for using VLC in hospitals and in healthcare. Mobile phones and WiFi's are undesirable in certain parts of hospitals, especially around Magnetic Resonance Imaging (MRI) scanners and in surgery rooms.

- **WiFi Spectrum Relief**

VLC can provide data rates greatly in excess of current WiFi and this can be done at low cost since the RF components and antenna system have been eliminated.

- **Aviation**

Radio is undesirable in passenger compartments of aircraft. LEDs are already used for illumination and can also be used instead of wires to provide media services to passengers. This would reduce the aircraft construction costs and its weight.

- **Underwater Communications**

RF is highly attenuated underwater but visible light can support high speed data transmission over short distances in this environment. This could enable divers and underwater vehicles to communicate to each other.

- **Location Based Services**

Each visible light information source can be uniquely identified, so the location of any VLC device can be identified quickly and accurately.

Chapter 3

Metameric Transmission

The use of RGB LEDs, instead of white phosphor based (white) LEDs, as transmitting device, can improve the achievable data rate of a VLC system. There are two main reasons that justify this improvement, one is the higher transmission bandwidth of off-the-shelf trichromatic LEDs in comparison with white LEDs counterpart. In fact, in this latter case, the white light is produced by phosphor coating a blue LED, which results in having only few MHz of modulation bandwidth. Moreover, in RGB LEDs, Wavelength Division Multiplexing (WDM) can be exploited in order to send parallel stream of data. In other words, the information is separately sent over different colors. In this regard, supporting this trend, in the literature can be found experimental works that present data throughput in the order of Gbit/s, using just a single LED [24] [25].

The use of trichromatic transmitters introduces new issues absent when white LEDs are adopted: the color perception of light. In fact, a good VLC communication system has also to guarantee a sufficient color rendering quality of the transmitted light. In order to better understand this issue, in Sect. 2.2 has been introducef the theoretical aspect of human color perception.

In the IEEE 802.15.7 third layer is implemented a trichromatic LED based modulation, Color Shift Keying (CSK), which encodes data in the instantaneous output color of the LEDs by varying the instantaneous optical power of each color band, while maintaining constant the total intensity to ensure flicker-free operation and avoid dimming. The physical layer standard specifies all the possible colors band combinations (CBC) and the relative modulation constellation design. However, the symbols choice is made without considering a thorough color rendering evaluation.

This issue has been addressed in [26, 27] and more recently in [28], where an optimization in the constellation design is investigated. In those works, two important parameters have been taken into account: *i)* luminous efficiency, which characterizes illumination of the LEDs, and *ii)* color rendering index, which is a measure of the capacity of a LED to produce a color comparable with an ideal light source.

In [4], for the first time, the concept of metamerism has been applied in VLC by using a minimum of four LEDs, and four independent detection channels. That method reduces color flicker by maintaining constant perceived ambient lighting and improves color rendering. As a drawback, the receiver is based on conversion (optical-to-electrical) current distance with respect to pre-stored ideal values so that it fails to achieve robust performance with respect to impairments (channel and external optical disturbances).

In this chapter, which is based on the publication [29], the CSK symbols are transmitted as a combination of different colors by using the principle of metamerism. Using different triplet of colors, in order to have a continuously perceived white, the different spectrum representation should be metamerically equivalent. Therefore, when the intensity of three LEDs is modulated, the color perception of the white light is used as a constraint. Moreover, it is introduced a modulation format that descends from PPM, namely Complementary Pulse Position Modulation (CPPM) signalling which differs from PPM, since information is carried by the absence of an energy component rather than its presence. CPPM is used jointly with CSK in order to improve the link data rate. Specifically, CPPM-CSK can be interpreted as a sort of Not-Return-to-Zero (NRZ) signaling since it is characterized by having a conventional CSK symbol with an on-off-on transition in time. Moreover, it is used a single photodiode at the receiver, in place of having multiple ones, since, in this way, it is possible to apply a broad spectrum analysis of the received signal. A bank of pass-band filters are able to detect the CSK symbols while the CPPM is based on time-based matched filters.

3.1 Transmitting different colors

As anticipated in the introduction of this chapter, when RGB LEDs are used to obtain a white light source, it is possible to use the triplet of LEDs as transmitter, each one able to transmit with a very specific set of wavelengths, related to red, green and blue, respectively. In the work presented in [29] it is considered the possibility of transmitting K different symbols, each one characterized by 3 wavelengths so the k-th CSK symbol is univocally defined by a spectrum with a peak centred on the wavelengths-triplet $[\lambda_k^{(1)},\ \lambda_k^{(2)},\ \lambda_k^{(3)}]$. Basing on this modulation, the number of bits that can be carried per symbol is $\log_2(K)$ as for Frequency Shift Keying (FSK) modulation even if this scheme requires 3 different wavelengths (bands) so it is a bit spectrally-inefficient with respect to RF FSK.

Formalizing the K-CSK description, the T_s-length signal driving the emission of the LED can be written as follows

$$x_k(t) = \sum_{m=1}^{3} \sqrt{\beta_{m,k}} g_{m,k}(t), \quad k = 1, ..., K, \tag{3.1}$$

where $\beta_{m,k}$ refers to the power associated with the emission of the color $\lambda_k^{(m)}$ related to the k-th CSK symbol that corresponds also to the m-th transmitting LED, while $g_{m,k}(t)$ is the shaping filter that drives the emission of the m-th LED on $\lambda_k^{(m)}$ wavelength. The signals $g_{m,k}(t)$ constitute an *orthogonal basis*. More, the signals $g_{m,k}(t)$ must be chosen in order to guarantee separation in the wavelength domain once converted in an optical emission. As it will be shown in the numerical results of this chapter, increasing the modulation order of CSK will lead to lose perfect orthogonality so leading to increase BER. The relationship between $\beta_{m,k}$ and $g_{m,k}(t)$ are tackled in [26,27] and [4] and now under recommendation of IEEE 802.15.7.

The work by the task group of IEEE 802.15.7 specifies the wavelengths that can be used to obtain a white light. In this regard, let each $\Gamma_{m,k}(\lambda)$ be the normalized emission spectra related to m-th of the three sources and to the k-th CSK symbol such that the following constraint is met

$$\int_0^\infty \Gamma_{m,k}(\lambda) d\lambda = 1. \tag{3.2}$$

Defining α_i^m as the spectral response induced by the m-th primary on the i-th class of cones of the human eye, that as the follows equation:

$$\alpha_{m,k}^{(i)} = \int_0^\infty \Gamma_{m,k}(\lambda) S_i(\lambda) d\lambda, \tag{3.3}$$

$S_i(\lambda)$ being the i-th cone response (see chapter 2).

Furthermore, let $C(\lambda)$ be the color stimulus of the ambient color that is in need to maintain.

So, by considering the aggregate response evoked by the primaries on the i-th class of cones regarding the k-th CSK symbol and by recalling the Grassmann's laws of color matching (see chapter 2), the following equations for all i values are given:

$$\sum_{m=1}^{3} \beta_{m,k}\alpha_{m,k}^{(i)} = \int_0^\infty C(\lambda)S_i(\lambda)d\lambda \ k = 1, ..., K. \tag{3.4}$$

Hence, the $\beta_{m,k}$ coefficients give the relative amount of each primary that is needed to achieve a metamerical match with $C(\lambda)$.

3.2 Complementary PPM over Different Colors

The order of magnitude of data rates requested for VLC applications is tens (and hopefully hundreds) of Mb/s [5], as a consequence the symbol duration T_s is of the order of tens of μs. In this regard, the properties of the human vision grant that the perceived optical stimulus generated by $x_k(t)$ remains substantially unaltered if a high flashing rate (beyond the critical fusion frequency, usually around $50-60$ Hz) is generated by a lamp or a LED (Block's law, see chapter 2). Thus, in order to increase transmission rate, it is possible to merge K-CSK and a modified version of PPM. Usually L-PPM signal can be represented in the following way

$$p_l(t) = u(t - l\Delta_p), \quad l = 0, ..., L-1, \tag{3.5}$$

where $u(t)$ is the T_p-length template signal, that is, the one that can be emitted by the LED while Δ_p is the time shift of PPM usually set to $\Delta_p = T_p + T_g$, T_g being the guard time so that $T_s = L\Delta$:

$$u(t) = \begin{cases} 1 & t < |T_p/2| \\ 0.5 & t = |T_p/2| \\ 0 & t > |T_p/2| \end{cases} . \tag{3.6}$$

One drawback of PPM, if used with K-CSK and, more, in the context of illumination, is duty cycle defined as the ratio between the percentage on one period in which the signal is non zero and the signal period. Duty cycle is $\delta_{dc}^{\mathrm{L-PPM}} = 1/L$, possibly giving rise to flickering and, worse, dimming.

In fact especially when a high cardinality in the PPM modulation is used, within a symbol period there is a considerable amount of time in which the signal is equal to zero.

Dealing with the solution based on VPPM described in [5], where different symbols present different duty cycles, the average duty cycle under the assumption of transmission of equally distributed symbols is $\overline{\delta_{dc}^{\mathrm{VPPM}}} = 50\%$. Expurgated PPM (EPPM) is considered in [6] to control the illumination level by controlling the peak to average power ratio (PAPR) with a proper symmetric balanced incomplete block design (BIBD) code and its duty-cycle is $\delta_{dc}^{\mathrm{EPPM}} = 3/7$ when the configuration with 7 slot is considered.

CPPM is of simple implementation and guarantee a low level of PAPR with higher-order modulation. It is defined as follows

$$p_n(t) = \sum_{l=0, l\neq n}^{L-1} u(t - l\Delta_p). \tag{3.7}$$

The above expression means that the signal has a constant pulse with the exception of the transition to zero. As previously indicated, differently from PPM, the information is not carried out by the position of a pulse but by the *location* on the time axis where no energy component is present. This modulation format is less power saving with respect to L-PPM, since it uses $L-1$ times the power spent by L-PPM. This is not an issue since a good illumination level must be granted in indoor environments. It is worth noting that CPPM avoids dimming/flickering since its duty cycle is given by $\delta_{dc}^{\mathrm{L-CPPM}} = (L-1)/L$.

The L-CPPM - K-CSK generic symbol can be defined as follows

$$s_{n,k}(t) = x_k(t)p_n(t) \tag{3.8}$$

The above introduced CPPM-CSK is based on the transmission of a simple CSK symbol with only one *on-off-on* transition whose slope depends on the LED capability to react to the on-off-on electrical stimulus. Differently from RF systems where, in general, a quick amplitude slope in time reflects on large bandwidth, here the optical application (in the visible spectrum) implicitly limits the bandwidth since VLC LEDs are in general not able to spread their own band beyond the visible one. As a consequence, if the slope of the on-off-on transition of the electrical driving signal is too fast to be performed by the LED, the optical radiation does not fall to zero in correspondence of the hole. This reflects on the *power distance* between the full power level and the hole and this effect increases BER as it will be shown later in the numerical results section.

As detailed in Fig. 3.1, the transmitter is characterized by the Color Mapper and the CPPM Mapper managing the signals driving the three LEDs. In particular the transmitter gathers blocks constituted by $\log_2 K + \log_2 L$ bits, where the Color Mapper controls the mapping of the first $\log_2 K$ bits of the block while CPPM Mapper maps the following $\log_2 L$ bits by introducing the hole on the CSK symbol. Hence, basing on (3.8), the transmission combines K wavelength-triplets with L-CPPM symbols. This is equivalent

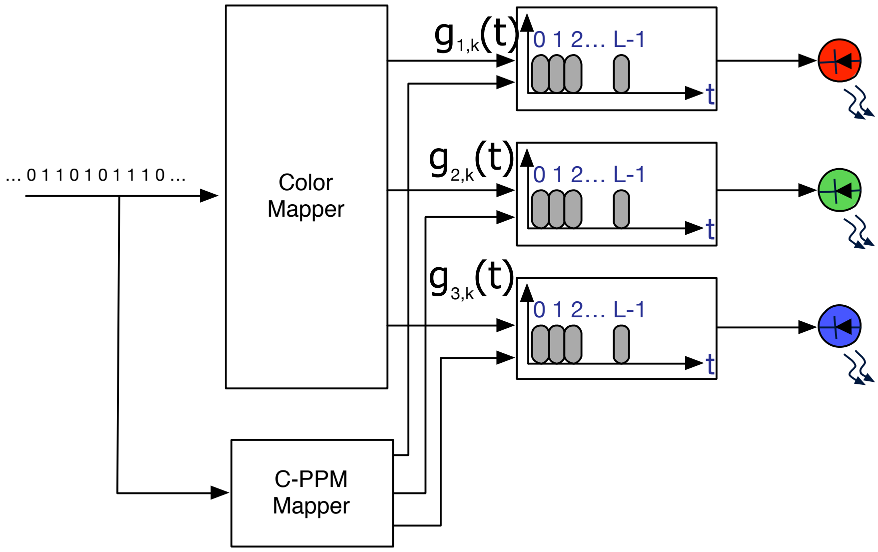

Fig. 3.1: Transmitter Scheme for the proposed modulation.

to transmit an K-CSK symbol of T_s length, as for CSK modulations from the literature, with a zero transition for a time length equal to T_s/L that equates T_p in (3.5) and (3.8). By representing the signal $s_{n,k}(t)$ as a L-length sequence (L elements vector), the possible transmitted pseudo-codeword is of the following kind

$$\mathbf{c}_u = [1...0...1] \tag{3.9}$$

with all ones with exception of a zero in the u-th position. By considering, for example, K=4 and L=4, the mapping is described in Table I.

About the rate that can be achieved by the L-CPPM - K-CSK modulation, by recalling that the time need to transmit a CPPM-CSK symbol is T_s, the transmission rate can be evaluates as in the following expression

$$\mathcal{R} = \frac{\log_2(LK)}{T_s}. \tag{3.10}$$

From (3.10) it is possible to note that the length of a CSK symbol influences the transmission rate. In fact, increasing T_s reduces rate as expected. On the other hand, by increasing K a rate increase it is obtained, even if orthogonality in the wavelength domain is not always possible for each K value with the consequence of worse BER. Another way of increasing

first $\log_2 K$ bits	successive $\log_2 L$ bits	transmitted pseudo-codeword
00	00	0111 on 1st CSK triplet
00	01	1011 on 1st CSK triplet
00	10	1101 on 1st CSK triplet
00	11	1110 on 1st CSK triplet
01	00	0111 on 2nd CSK triplet
01	01	1011 on 2nd CSK triplet
01	10	1101 on 2nd CSK triplet
01	11	1110 on 2nd CSK triplet
10	00	0111 on 3rd CSK triplet
10	01	1011 on 3rd CSK triplet
10	10	1101 on 3rd CSK triplet
10	11	1110 on 3rd CSK triplet
11	00	0111 on 4th CSK triplet
11	01	1011 on 4th CSK triplet
11	10	1101 on 4th CSK triplet
11	11	1110 on 4th CSK triplet

Table 3.1: Mapping of colors and CPPM symbols on pseudo-codeword

rate, from (3.10), is to increase the L order. However, having large L values will induce a technological effort since LEDs able to perform fast on-off-on transition are required. Nevertheless, the rates considered in the numerical results are in line with the LEDs currently available on the market.

The achievable rates for different values of L and K are reported in Fig. 3.2. The maximum rate, by considering a bandwidth of 24MHz (as in [5]) is achieved for 32-CSK (maximum allowed by IEEE 802.15.7 is 16-CSK) and 32-CPPM (in line with the technological possibility of driving LED with on-off-on transition and the same for photodiode) and equates 240Mb/s.

3.2.1 Receiver Architecture

The signal received after the photodiode is given by

$$z(t) = \rho A_e p_{nk}(t) * h^{(\mathrm{LED})}(t) * h^{(\mathrm{ch})}(t) * h^{(\mathrm{PH})}(t) + N(t) + W(t) \qquad (3.11)$$

where $h^{(\mathrm{LED})}(t)$ is the LED response, $h^{(\mathrm{ch})}(t)$ is the channel impulse response and $h^{(\mathrm{PH})}(t)$ is the response of photodiode. The symbol $*$ is the convolution operator, $N(t)$ is shot noise due to ambient light, Poisson distributed, and $W(t)$ is the Additive White Gaussian Noise due to the electrical components in the receiver. In wireless optical, as opposed to fiber, a large amount

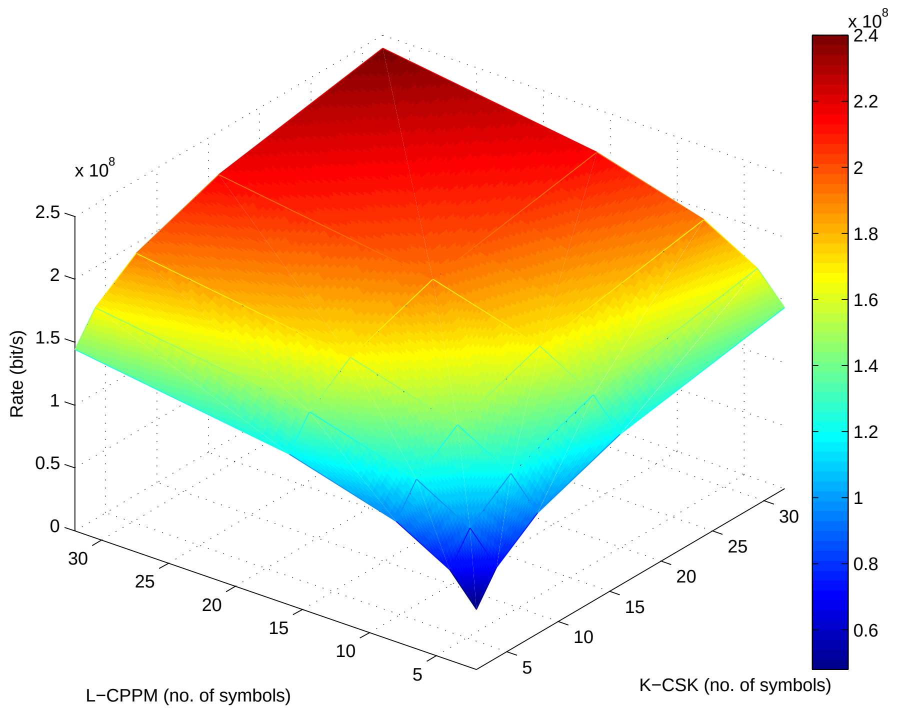

Fig. 3.2: Achievable rates for different values of L and K.

of ambient light is collected, therefore it is appropriate to model this noise as white and Gaussian [30]. The term ρ indicates the responsivity of the photodiode (A/W) and A_e is the effective receiver area (m^2).

Fig. 3.3 details the receiver architecture. After the photodiode, the receiver is composed by K different branches each one tuned on three different $g_{m,k}, \ m = 1, ..., 3$ corresponding to the k-th CSK symbol. Hence, in order to evaluate the power component in the sub-interval $[lT_s/L, (l+1)T_s/L]$ with $l = 0, ..., L-1$, so as to detect where the *hole* is located, the following metric is considered

$$\eta_{kl} = \int_{lT_s/L}^{(l+1)T_s/L} z(t) g'_k(t) dt \quad k = 1, ..., K, \ l = 0, ..., L-1, \tag{3.12}$$

where

$$g'_k(t) = \sum_{m=1}^{3} \sqrt{\beta_{m,k}} g_{m,k}(t), \quad k = 1, ..., K. \tag{3.13}$$

It is noticeable that, the joint effect of LED response, channel and photodiode is represented as $h(t) = h^{(\text{LED})}(t) * h^{(\text{ch})}(t) * h^{(\text{PH})}(t)$, and it allows to hold the presence of the hole, thus meaning that the delay spread of the overall $h(t)$ is sufficiently short with respect to T_s/L, that is the length of a hole.

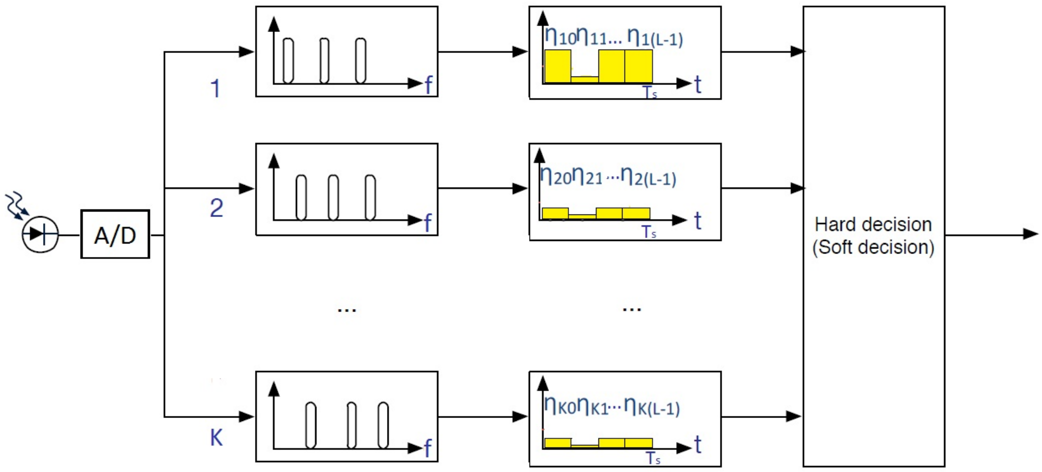

Fig. 3.3: Receiver Scheme for the CSK-CPPM modulation format.

3.2.2 Decision mechanism

As reported in Fig. 3.3, the decision process can be performed according to Hard Decision (HD) mechanism or Soft Decision (SD) one. Once available the $K \cdot L$ metrics η_{kl}, these must be compared with a threshold ϑ_k in order to decide for 0 or 1, and this depends on k since the symbols are not at the same energy level. This approach is allowed by the above cited assumption about the delay spread of $h(t)$ required to be sufficiently short, otherwise equalization must be performed. So, once operated thresholding mechanism, the hard decision metrics become

$$\eta_{kl}^{HD} = \begin{cases} 1 & \eta_{kl} \geq \vartheta_k \\ 0 & \eta_{kl} < \vartheta_k \end{cases} \qquad k = 1, ..., K, \; l = 0, ..., L-1. \tag{3.14}$$

Those metrics are then gathered in K vectors composed by L elements defined as follows

$$\boldsymbol{\eta}_k^{HD} = [\eta_{k0}^{HD} \; \eta_{k1}^{HD} ... \eta_{k(L-1)}^{HD}]. \tag{3.15}$$

So, each L-ple is compared (in the Hamming distance sense) with all the possible transmitted *pseudo-codewords*. So the decided codeword is given by

$$(\hat{k}^{\star}, \hat{u}^{\star}) = \arg \min_{\substack{k=1,..,K,\\ u=0...L-1}} \sum_{l=1}^{L} \mathbf{c}_u(l) \oplus \boldsymbol{\eta}_{kl}^{HD} \quad (3.16)$$

where $\oplus$ is the exclusive OR operator.

Regarding the Soft Detection the metrics in (3.12), they are gathered in the following K vectors defined as

$$\boldsymbol{\eta}_k^{SD} = [\eta_{k0}\ \eta_{k1}...\eta_{k(L-1)}] \quad k = 1, ..., K,\ l = 0, ..., L-1. \quad (3.17)$$

and the decision mechanism works according to the following rule

$$(\hat{k}^{\star}, \hat{u}^{\star}) = \arg \min_{\substack{k=1,..,K,\\ u=0...L-1}} ||E_k \cdot \mathbf{c}_u - \boldsymbol{\eta}_k^{SD}||^2 \quad (3.18)$$

where E_k is the reference expected signal level at the transmitter by considering the channel effect. Details about thresholds are detailed later in a specific remark.

The inverse operation with respect to pseudo-code mapping is the pseudo-code demapping. Once determined the indexes $k^{\star}$ and $u^{\star}$, the demapping will lead to have the first $\log_2 K$ bits characterized by the binary representation of $k^{\star}$ and the successive $\log_2 L$ bits are obtained by the binary representation of $u^{\star}$. This is equivalent to read Table **??** from right to left.

Remark - Threshold and channel knowledge
Both threshold ϑ_k for HD in (3.16) and E_k term in (3.18) must be properly, and in general adaptively, set in order to take care of the effect of the channel. Indeed, without taking into account the channel attenuation/distortion, the error rate can be high since it is possible to have misdetection events. This effect can be counterbalanced by channel estimation performed on the basis of a specific training sequence transmitted with a proper time interval, that means, not so frequent since it induces rate loss, and not so sporadic since channel changes. In this regard, sending pilot symbols every second is in line with the above consideration since channel changes are essentially due to different reflections coming from the room due to reflecting objects and/or receiver movements). By performing a channel estimation using pilot symbols, one for each and every CSK symbol, the received signal is

$$z_k^{[T]}(t) = \rho A_e x_k^{[T]}(t) * h(t) + N(t) + W(t) \quad (3.19)$$

and, where $x_k^{[T]}(t)$ (the superscript $[T]$ stands for training) is known at the receiver and it is of the same kind of symbols emitted for data downstream, with the difference that they are only CSK (not CPPM) symbols. So, the term E_k is

$$E_k = \frac{1}{L} \sum_{l=0}^{L-1} \int_{lT_s/L}^{(l+1)T_s/L} x_k^{[T]}(t) g_k'(t) dt. \tag{3.20}$$

The relationship in (3.20) shows that the estimated received power can be considered as the superposition of three different components given by the pulse filtered by channel plus the effect of noise. That value is the expected one when the transmission of the k-th CSK symbol is operated. Regarding the HD, the threshold can be set according to

$$\vartheta_k = E_k/2. \tag{3.21}$$

It is possible to recognize how in (3.20) the effect of $h(t)$ is important. It reflects both on the amplitude value to be compared with and also the technological behavior of LEDs and photodiode. So, imperfect evaluation of the thresholds leads to imperfect threshold setting and consequent BER performance degradation.

3.2.3 Numerical Results

To evaluate the performance of the CPPM-CSK modulation, computer modeling is used. The model used is CandLES, an open-source framework described in large part in [31] and used in several papers in the literature. Before proceeding, the main aspects of the propagation scenario are the follow:

- For LED optics, a wide intensity pattern (45^o Full Width at Half Maximum - FWHM) that is common for lighting LEDs.
- The light signal encounters a realistic indoor environment with many barriers as shown in Fig. 3.4. The walls and surfaces are simulated as being strongly reflective across the visible light spectrum (0.8 reflectivity factor, similar to light colored or white walls). The direct Line of Sight - LOS path and all indirect paths of light, up to and including four reflections, were included in all propagation scenarios since this is required for accurate approximation of the multipath impulse response [32].
- Noise sources modelled include shot noise from the LED light and from a level of sunlight in the room that is considered high, as well as thermal and amplifier noise from receiver electronics [33].

- The receiver effective area A_e includes the actual photodiode area, and accounts for angle of light incidence, and the concentrator used [20, 33]. The model has a wide Field of View - FOV hemispherical lens.

The parameters used for computer simulations are detailed in Table II.

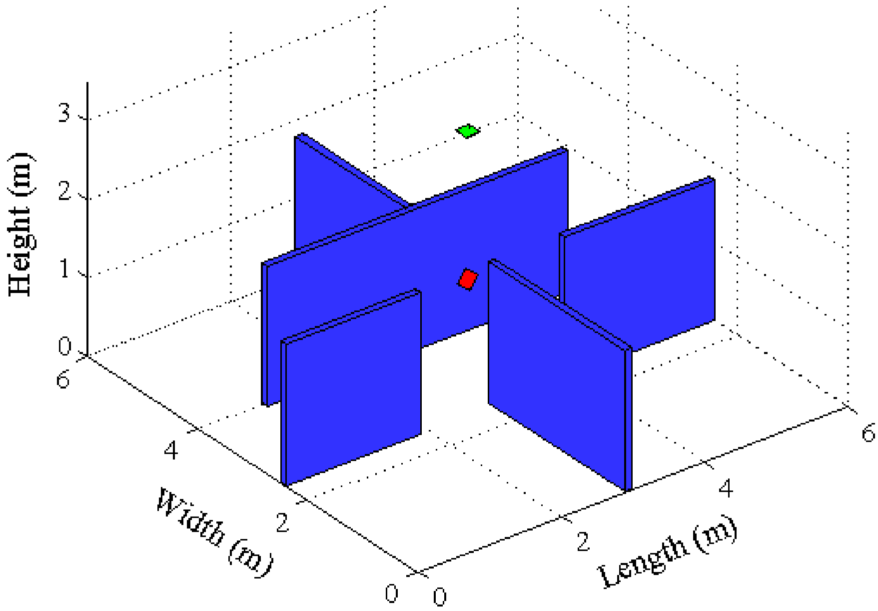

Fig. 3.4: A model of a small cubicle office in which a VLC transmitter light bulb is deployed at the ceiling pointed down. The receiver is mobile and occupies different positions and orientations. The three representative cases are as follows: (1) a short distance (1.5m) aligned case, LOS link, (2) a long distance (2.5 m) aligned case, Non-Direct LOS link (ND-LOS) which is dominated by the direct path but also exhibits a significant multipath tail due to reflected components, and (3) a case in which the receiver is pointed away from the transmitter resulting in Non Line-of-Sight (NLOS) link that only relies on reflected signal components. Channels classification, LOS, ND-LOS and NLOS is referred to work by [3].

Fig.3.5 details BER as a function of noise level when different LEDs are used at the transmitter. It is evident that the best performance in terms of BER is that achieved by LED CREE CLP6C-FKB (see [?] for specifications), since it is able to be more power efficient and presents better performance with respect to the other three cases that are THOR LABS LEDRGBE, KING BRIGHT KAA-3528RGBS and HEBEI LTD 540R2GBC-CA, whose specifications can be found in [?], [?] and [?] respectively and in Table II. The gain

LED Transmitter	
LED	Red, Green, Blue (nm) [bandwidth]
CREE CLP6C-FKB	24 , 38 , 28
KINGBRIGHT KAA-3528RGBS	20 , 30 , 25
THORLABS LEDRGBE	20 , 36 , 15
HEBEI IT LTD 540R2GBC-CA	20 , 22 , 30
Maximum transmit sum power P_t	7 W
Beam angle	$45°$ Full Width Half Maximum
Room setup	
Dimensions ($l \times w \times h$)	6 m $\times$6 m $\times$3.2 m
Surface reflectivities	0.8
Ambient (DC) irradiance	5.8μW/(cm$^2\times$ nm)
3 LEDs coordinates	$(3.05, 3.05)$, $(3.05, 3)$, $(3, 3)$,
Receiver	
FOV	$90°$
Area	15 mm^2
Lens gain factor	2.2
Effective area A_e	33 mm^2
Optical filter	450 ± 20 nm, 60% through
Responsivity @450 nm	0.2 A/W
Responsivity @650 nm	0.4 A/W
Load resistor	750 Ohm

Table 3.2: Simulations parameters about LEDs, propagation and Receiver.

offered by LED CREE can be justified with its bandwidth since it presents higher spectral components with respect to the others so increasing the Signal-to-Noise Ratio (SNR). This suggests to use, also for performance comparison with another solution adopted in the literature, the LED CREE.

The behavior of LEDs with respect to the signal driving the optical radiation can be of paramount importance. In fact, some LEDs may be unable to present a hole achieving zero-emission as previously stated and detailed in Fig. **??**. For this reason, in Fig. 3.6 the performance of different LEDs slope, in terms of hole percentage, is presented. It is possible to appreciate that, as expected, the best performance is exhibited by the full-zero transition represented by 100% hole. However, the SNR loss of the 50% depth hole is limited to 2.5dB, while the 25% depth hole (that is a transition till to 75% of the maximum power level) is around 7dB.

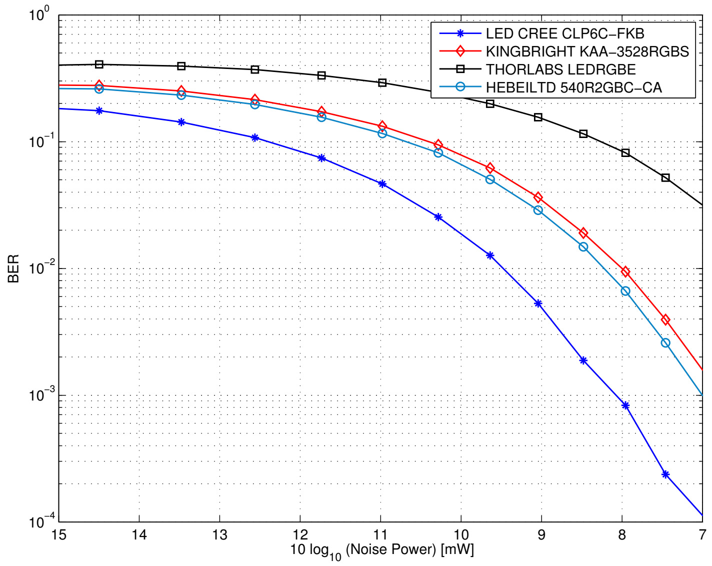

Fig. 3.5: BER values for different LEDs used at the transmitter with hard detection.

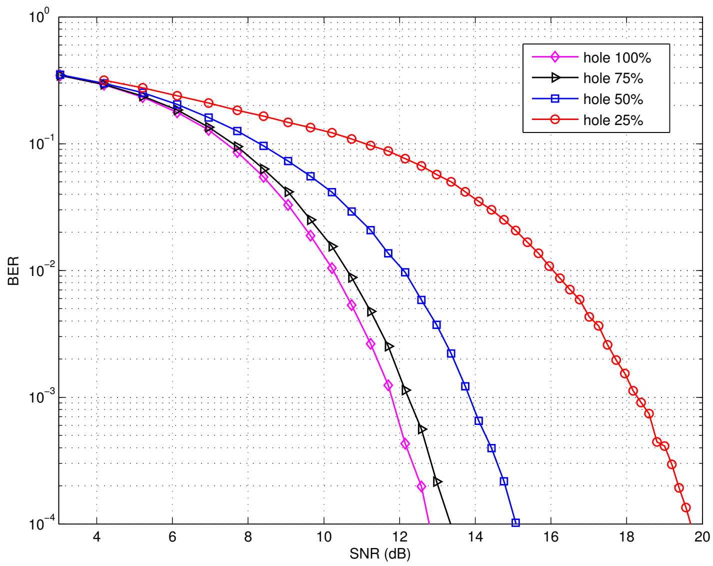

Fig. 3.6: BER values for different slops and holes.

By considering the performance in terms of BER offered by 4-CSK and 8-CSK modulations combined with 2-CPPM, 4-CPPM and 8-CPPM, in Fig. 3.7 it is possible to appreciate how increasing the CPPM order leads to a BER reduction.

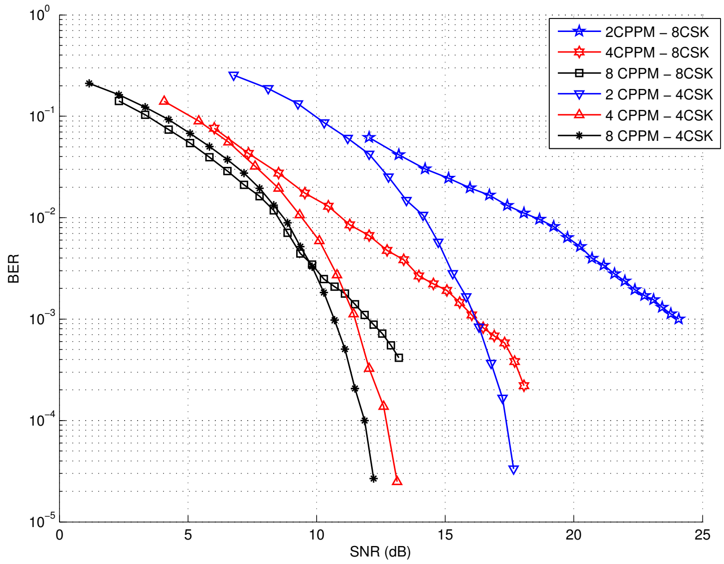

Fig. 3.7: BER values for different L and K valeus.

One example is related to the maximum SNR gain achieved by 8-CPPM - 4-CSK with respect to 2-CPPM - 8CSK. The gain is of about 12dB. Differently from the conventional RF orthogonal modulations, having 8-CSK is not preferable with respect to 4-CSK (for the same CPPM format). This result is justified by observing that when K increases, perfect separation in the wavelength domain may be not granted. The proof is that the presence of the error is experienced in the first $\log_2 K$ bits, while the successive $\log_2 L$ are error free. However, as anticipated, since a good illumination level must be granted, looking for power saving strategies is not an issue, so it is possible to increase power if a target transmission rate must be achieved.

In order to test the robustness of this scheme with respect to channel behavior and its knowledge, in Fig. 3.8 BER is reported as a function of SNR and, more, comparison with the achieved performance are given, under the assumption of 24MHz bandwidth and 96Mb/s rate with those relative to the scheme proposed in [4] (same bandwidth and 48Mb/s rate),

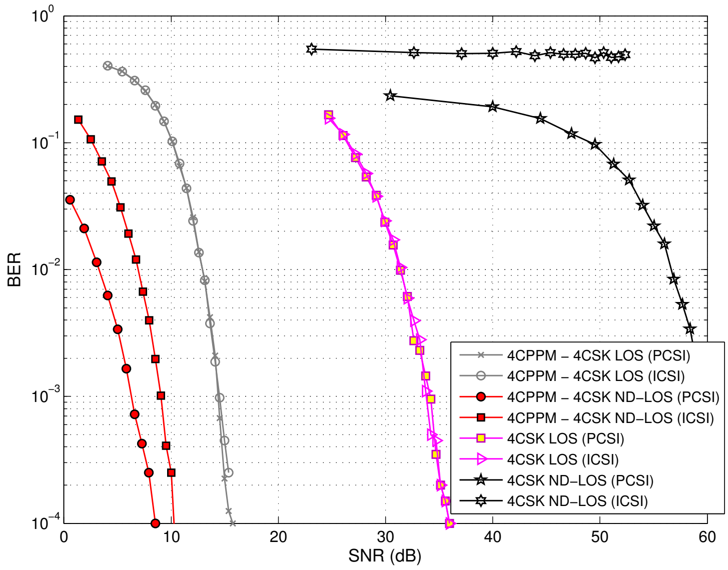

Fig. 3.8: BER values for LOS propagation and ND-LOS one with the scheme proposed in [4] by considering also the effect of channel state information (CSI) perfect (PCSI) or imperfect (ICSI).

in two different propagation scenarios that are LOS and ND-LOS. Before proceeding, it is mandatory to specify that ND-LOS means that some reflective paths are present and their amplitudes are comparable with the main component (numerically the 60% of power is on the main path). For evaluating performance under the assumption of ND-LOS channel, are considered reflective components as those output by CandLES simulator (see [31]) correspondent to be close to the wall of the room (80cm from the wall).
Performance in LOS is better than that exhibited in ND-LOS channel for the 4-CSK scheme presented in [4], while it is not the same for the CPPM-CSK proposed in this work.

In fact this scheme presents better performance in the ND-LOS due to the energy captured by the photodiode due to direct component and reflections falling (from a temporal point of view) in the reception window. The whole effect is quite similar to that of a RAKE receiver (see [34]) since the delay spread of the channel is sufficiently short.

Another valuable aspect to underline for CPPM-CSK is about the impact of channel state information (CSI). Channel knowledge is more important in the ND-LOS channel where it is observed a BER degradation mainly due

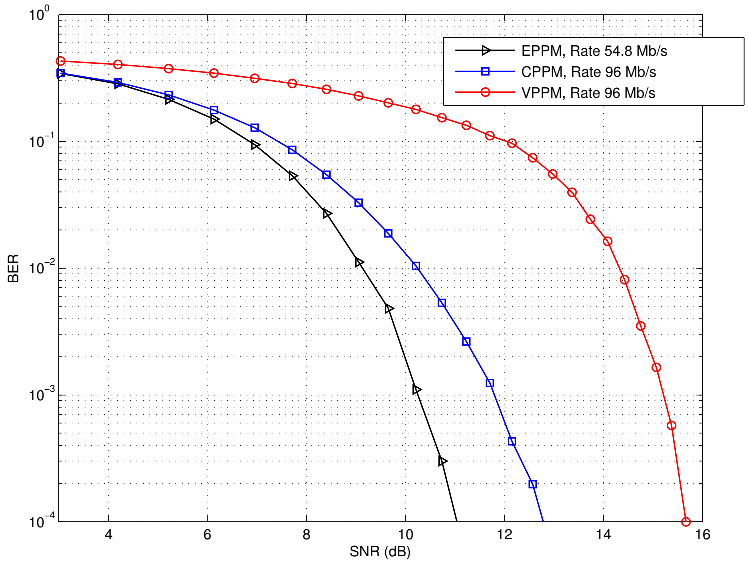

Fig. 3.9: BER values for CSK modulation merged with the proposed CPPM, VPPM as in [5] and EPPM as in [6].

to the error threshold setting (since it is adaptive) and this heavily reflects also on 4-CSK ND-LOS since a BER floor is present. It is important to note that the imperfect channel state information (ICSI) reflects directly on the thresholding operations since the receiver needs channel knowledge. ICSI means to have a rough estimated version of the channel, that is an error of 15% on the coefficients.

In Fig. 3.9 is plotted BER of the CPPM-CSK scheme in comparison with the above mentioned VPPPM and EPPM (both merged with CSK in order to have a fair comparison), it is possible to note that EPPM, in the version proposed in the paper [6] with Q parameter equating 7, is the best among the three compared schemes. This is paid in terms of rate, since EPPM achieves 54.8Mb/s while CPPM loses around 1dB having a rate of 96Mb/s. The rate achieved by VPPM, in this set of simulations, equates the one of CPPM but BER exhibited by VPPM is worse since it presents a SNR loss of 4dB and, more, VPPM has a low duty cycle as already stated.

3.3 RGB Spatial Multiplexing

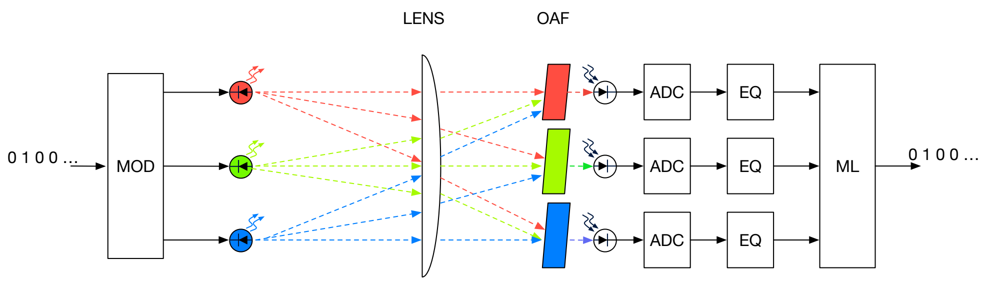

Fig. 3.10: Scheme of the RGB Spatial Multiplexing. Transmitter, channel and receiver.

One advantage on using trichromatic LEDs is the possibility to have data rate performance enhancement that relies on the use of multiple transmitters, each sending an independent data stream, so, using a MIMO nomenclature, having spatial multiplexing.

Regarding VLC schemes employing an RGB transmitter to improve communication data rate, in the literature can be found several works, such as [35],[36] and [25] are presented schemes . The solution proposed in [35] considers different modulations formats to achieve a very high data rate, of the order of Gb/s, by using a single commercial RGB-White LEDs and three RGB LEDs. At the transmitter perfect channel knowledge is required in order to perform bit-loading. So the experiment considers a preliminary channel measurement and an off-line optimization. The work in [36] measures the effect of interference of other colors on the main color (for example BER reduction due to green and blue component on a red channel). A pre-compensation filter at the transmitter is adopted as well as a digital feedback (DFE) equalizer at the receiver. DFE so requiring channel knowledge that is assumed present both at the transmitter and the receiver. A different and interesting mechanism is considered in [25], where least mean square with decision directed mechanism is considered with 3 LEDs and 3 photodiodes. Experimental results report that, using a 512-QAM scheme, a peak data rate of 4.22 Gb/s has been achieved, although measured at a 1 cm distance and considering a remarkable per channel bandwidth of about 156 MHz. That scheme still assumes to have perfect channel knowledge at the transmitter since pre-equalization is performed

In the system presented in the literature, high data rates are achieved mainly due to the large band of the system and rich modulation formats that often requires perfect channel knowledge at the transmitter. In the next section, instead, the simple amplitude shift keying (ASK) modulation is considered. Considering the scheme of Fig. 3.10, the presence of interference at each photodiode generated by the other two colors is used to improve detection since interference is symbol-dependent. Moreover, the capability of the photodiodes to follow the LEDs speed is considered by analyzing the possibility of equalizing the received signal and also self-interference mitigation is presented. An experimental setup based on Arduino-Due board is implemented and presented at the end of the chapter.

3.3.1 System model

Considering the presence of three LEDs (as depicted in Fig. 3.10), each tuned on a different wavelength, namely, red, green and blue (RGB), so to have as transmitted signal in the signalling interval T_P

$$s(t) = \sum_{c \in \mathcal{C}} A_c s_c(t) \tag{3.22}$$

where the set $\mathcal{C} = \{R, G, B\}$ collects the three different colors, the term $A_c \in \mathcal{A} = \{1, 2, ..., M\}$ can assume each of the M different amplitudes and $s_c(t)$ is the shape of radiation representing the light emitted by the c-th color LED in a NRZ way. It is important to note that different colors exhibit different $s_c(t)$.

The presence of the term A_c implicitly means that the R, G, B LEDs can, symbol by symbol, emit different light intensities. Since this reflects also on illumination service, it is important to analyze the relationship with respect to flickering of the light, dimming and color rendering [29]. To handle these three light emission aspects it is in need to resort to the human eye properties and behavior introduced in chapter 2.
Flickering effect, that is, the sensation of changes in light intensity is ruled by the second Bloch's law states that the human eye is able to perceive light intensity changes if the flashing frequency is of the order of 50÷ 100 Hz. In the scheme presented here, this would imply $T_P = 10ms \div 20ms$, and since such a high value of signaling time is not used, flickering is totally avoided in this system.

Regarding dimming, the important aspect is the (average) power, measured on a time interval that is the one the retina needs to measure light ($T_{retina} = 20ms$). The number of symbols transmitted by the LEDs within T_{retina} is $N_s = \lfloor T_{retina}/T_P \rfloor$ so the power is measured as:

$$\mathcal{P} = \frac{1}{T_{retina}} \int_{T_{retina}} \sum_{p=1}^{N_s} \sum_{c \in \mathcal{C}} A_c(p) s_c(t - pT_P) dt. \tag{3.23}$$

If this value is compared with the one obtained with a fixed light in the same interval

$$\mathcal{P}^{(ill)} = \frac{1}{T_{retina}} \int_{T_{retina}} \sum_{c \in \mathcal{C}} A_c^{(ill)} dt \tag{3.24}$$

$A_c^{(ill)}$ being the color light intensity used for illumination, so that the difference is

$$\Delta\mathcal{P} = \mathcal{P}^{(ill)} - \mathcal{P} =$$

$$\frac{1}{T_{retina}} \int_{T_{retina}} \sum_{c \in \mathcal{C}} \left(A_c^{(ill)} - \sum_{p=1}^{N_s} A_c(p) s_c(t - pT_P) \right) dt \tag{3.25}$$

Also in this case, it is referred to the time needed by retina to acquire a signal in order to evaluate the colors emitted by the LEDs. This can be easily evaluated via short time Fourier Transform. So the spectrum is essentially given by:

$$X(f) = \frac{1}{T_{retina}} \int_{T_{retina}} \sum_{p=1}^{N_s} \sum_{c \in \mathcal{C}} A_c(p) s_c(t - pT_P) e^{i2\pi f t} dt \tag{3.26}$$

Hence, as it is possible to note from (3.26), different color components are present and the perceived color is expected to be a *mixture* of different levels of white and other colors ranging from red to green and blue. Also in this case, for a fast blinking light, the second Bloch's law helps our discussion. In fact, when the maximum light level is emitted, a high light intensity (white) is obtained. Other colors, with lower light intensity are essentially not perceived due to the band-pass behavior of the eye with respect to the quick transition (of the order of milliseconds or less) of the light intensity.

Still regarding the system architecture presented in this section, at the receiver it is assumed to have 3 different photodiodes each one tuned on the corresponding R, G, B LEDs. This is possible thanks to the use of optical analog filters (OAFs) as depicted in Fig.3.10. Hence, the first photodiode is tuned on red, the second on green and the third one on blue. This is

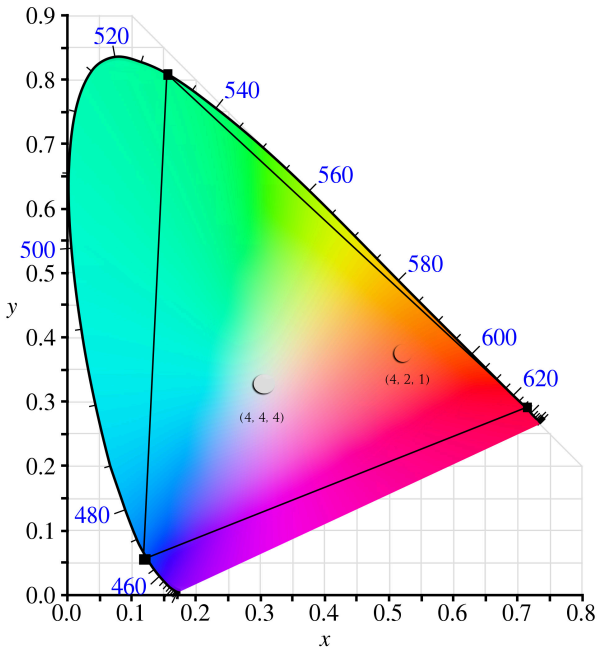

Fig. 3.11: CIE 1931 diagram with primaries and an example of symbol (4,4,4) and (4,2,1).

possible by using colored transparent stripes. Fig.3.12 represents the effect of OAF and shows, taken from a camera, the effect of using colored filters to try to isolate red component in the second image of Fig.3.12, green in the third image and blue one in the bottom image. It is possible to appreciate that isolating red is quite easy while it is not the same for blue and green. The white areas on the images are due to the saturation of illuminance of the camera.

A MIMO channel with 3 transmit LEDs and 3 receive photodiodes it is considered. The channel impulse response between the c-th LED and j-th photodiode is denoted as $h_{cj}(t)$. The composite MIMO channel response is

$$\mathbf{H}(t) = \begin{bmatrix} h_{RR}(t) & h_{RG}(t) & h_{RB}(t) \\ h_{GR}(t) & h_{GG}(t) & h_{GB}(t) \\ h_{BR}(t) & h_{BG}(t) & h_{BB}(t) \end{bmatrix} \tag{3.27}$$

As an example, the vector $[h_{RR}(t)\ h_{RG}(t)\ h_{RB}(t)]$ is essentially the spatio-temporal signature induced by the red light across the three photodiodes thus meaning that the pulse emitted by red LED from three different points of view can be measured. The matrix structure induces the following remark related to correlation among channels, both from a space and time

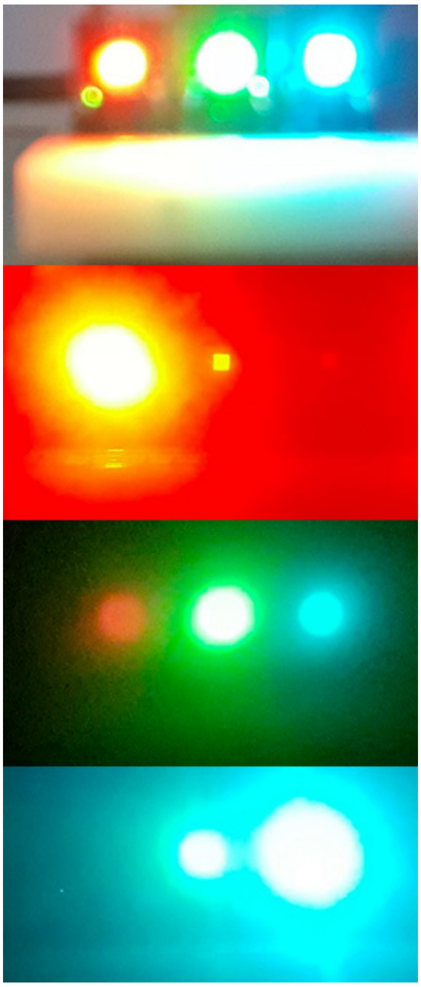

Fig. 3.12: RGB LEDs as emitted and filtered by the three OAFs tuned on red, green and blue.

point of view. With the above matrix, nine channels are present. If the channels are spatially correlated, it is not possible distinguish among the different components also in the presence of perfect channel knowledge at the receiver. This is essentially due to the impossibility of inverting the effect of channel matrix and process it to obtain a diagonal one. Proper spacing of LEDs can reduce correlation as reported in [Chapt.6][**?**] and this allows also a better light pointing if needed for illumination purposes [37]. The above formulation allows us to detail the received signal. In fact, given that the signal $A_c s_c(t)$ is emitted by the c-th LED, the whole signal received at the j-th photodiode (with $j \in \mathcal{C}$ is given by

$$y_j(t) = \sum_{c \in \mathcal{C}} A_c s_c(t) * h_{cj}(t) + w_j(t) \tag{3.28}$$

where $*$ is the convolution operator, $h_{cj}(t)$ is the whole channel impulse response, that is generic element of the matrix $\mathbf{H}(t)$, while $w_j(t)$ is the additive white Gaussian noise. Before proceeding, it is mandatory to explain the role played by $h_{cj}(t)$ and the different features that compose the channel impulse response. The term $h_{cj}(t)$ can be exploded as following

$$h_{cj}(t) = f_{FSP_{cj}}(t) * f_L(t) * f_{cj}(t) * f_{PD}(t) \tag{3.29}$$

where $f_{FSP_{cj}}(t)$ is the effect of free space propagation from the LED associated to the c-th color to the j-th photodiode that can be modeled according to geometrical parameters. More about free space propagation, by resorting to the work in [30], it is considered $f_{FSP_{cj}}(t)$ without reflectors, as follows:

$$f_{FSP_{cj}}(t) \approxeq \frac{m+1}{2\pi} \cos^m(\phi) d\Omega \, \mathrm{rect}_{FOV}(\theta) \delta\left(t - d_{c,j}/v\right), \tag{3.30}$$

where $d\Omega$ is the solid angle subtended by the receiver differential area, by assuming A_e (detector size) $<<$ $d^2_{c,j}$, with d distance between the transmitter and receiver and v the propagation speed,

$$d\Omega = \cos(\theta) A_e / d^2_{c,j}, \tag{3.31}$$

while ϕ is the angle of irradiance, θ is the angle of incidence with respect to the receiver axis, and m is Lambertian order that characterizes the light beam directivity. In this regard, it is possible to consider the amplitude of the received signal as:

$$a(d) = \frac{m+1}{2\pi} \cos^m(\phi) d\Omega \, \mathrm{rect}_{FOV}(\theta). \tag{3.32}$$

Moreover, $f_L(t)$ in (3.29) models the effect of a possibly present lens used to focus the light beam as depicted in Fig. 3.10 and its modeling can follow the work presented in [38]. Furthermore, $f_{cj}(t)$ in (3.29) is the impulse response of the OAF represented by the above mentioned colored transparent stripes tuned on LEDs. Last, $f_{PD}(t)$ in (3.29) is the channel impulse response of the photodiode. An ideal case for RGB components is $h_{cj}(t) = 0, c \neq j$ thus meaning that, for example, the red component is not received by the G and B tuned photodiodes so the interference between colors (named self-interference) is absent, thus meaning that the matrix

$\mathbf{H}(t)$ is diagonal. However, this is not true in general and self-interference is expected to be present at the photodiode as depicted in Fig. 3.12. This kind of interference is essentially the interference among spatial symbols, that is, spatial intersymbol interference (ISI). Still about non-idealities, it is also possible that the $f_{PD}(t)$ term is not able to *follow* the dynamic behavior of LED so introducing time dispersion, that is, temporal ISI.

3.3.2 Detection mechanism

Before detailing the detection mechanism, it is fundamental to consider one key point. In this system the interference generated by colors that differ from the one the photodiode is tuned to, has a twofold nature. From one hand interference is an impairment for the reliability of the communication while from the other side interference carries information since it is tied to the symbol emitted by other LEDs (with respect to the color-tuned photodiode). The detection of the symbol related to the c color on the $j = c$ photodiode depends on the received signal that is the sum of the effect of the channels on the symbols emitted by all the LEDs so leading to have the interference symbol-dependent as reported in (3.28). Hence, the idea for performing detection is taking into account not only the symbols that the c-th LED can emit but also all the possible symbols emitted by the other (two) LEDs and filtered by the channels. Moreover, joint detection it is performed (and not separated on the three branches), that means, having a joint measure of useful signal and interfering ones since what is emitted by a LED has three different versions at the photodiodes as previously disclosed.

The preliminary action to take into account is the transmission of a pulse by each LED (with the other LEDs turned off) so giving rise to a training sequence. From a matrix point of view it is the same of assuming that the transmitted matrix, that collects in the rows the symbols transmitted by the 3 LEDs, is the identity one. In this way, for example, when the red pulse is sent, the signal at the j-th photodiode will be

$$y_j(t) = A_R s_R(t) * h_{Rj}(t) + w_j(t) \tag{3.33}$$

Dealing with discrete time estimation, it is mandatory to preliminary sample the received signal $y_j(t)$ so to have $y_j(nT_s)$, T_s being the sample time. This operation is performed by the analog to digital converter (ADC) as depicted in Fig. 3.10. In this way, by extending this mechanism to all the RGB components, the estimation $\tilde{h}_{cj}(nT_s)$ of the discrete time channel $h_{cj}(nT_s)$ can be obtained thanks to the use of training.

Working in the frequency domain, so by considering $H_{cj}(k)$ as the Discrete Fourier Transform (DFT) of $h_{cj}(nT_s)$, the estimation $\tilde{H}_{cj}(k)$ is given by

$$\tilde{H}_{cj}(k) = \frac{Y_j(k)}{S_c(k)} \tag{3.34}$$

where $Y_j(k)$ is the DFT of $y_j(nT_s)$ and $S_c(k)$ is the DFT of the sampled pulse transmitted by the c-th color $s_c(nT_s)$. The discrete time version of the estimation can be obtained by applying the inverse DFT to $\tilde{H}_{cj}(k)$. The next step is related to the detection of data symbols. At the j-th branch, corresponding to the j-th photodiode chain, a ($N_P \times M^2$ matrix) named $\mathbf{Z}_j$ is built and it is defined as follows

$$\mathbf{Z}_j = [\mathbf{z}_j^{(A_{c_m}=1, A_{c_l}=1)} \; ... \; \mathbf{z}_j^{(A_{c_m}=M, A_{c_l}=M)}] \tag{3.35}$$

that is the collection of the column vectors $\mathbf{z}_j^{(A_{c_m}=m, A_{c_l}=l)}$ each one gathering N_P samples, where $N_P = \lfloor T_P/T_s \rfloor$. The generic element of the matrix $\mathbf{Z}_j$ is given by

$$\mathbf{Z}_j[n, v] = y_j(nT_s) - \sum_{c_v \in \mathcal{C}/\{j\}} A_{c_v} s_{c_v}(nT_s) * \tilde{h}_{c_v j}(nT_s). \tag{3.36}$$

that is the received sample where it is subtracted the value of interference by exploring all the M^2 values[1] for the symbol emitted A_{c_l} and A_{c_m}. It is worth noting that the term v is an auxiliary variable used to span the M^2 values and it is formally defined as $v = (m-1)M + l$ where m and l are the m-th and l-th symbols emitted by c_m-th and c_l-th interfering LEDs respectively, while c_v collects the pair of colors c_m and c_l. Hence the use of v helps to sort in the matrix $\mathbf{Z}_j$ the symbols emitted by the interfering LEDs.

As previously disclosed, it is possible that the j-th photodiode is unable to present raise and fall times comparable with LEDs speed, hence an equalization, operated on the sampled signal, must take place. A possible implementation is the Zero Forcing one, which consists in estimating the channel between the reference LEDs and the tuned photodiode $\tilde{H}_{jj}(k)$ obtaining its reciprocal $G_{jj}(k) = \tilde{H}_{jj}^{-1}(k)$ and then inverting it according to the inverse DFT, so as to arrive at $g_{jj}(nT_s)$. This allows to consider the equalization as the convolution between each of the columns of $\mathbf{Z}_j$ and $g_{jj}(nT_s)$. So, the output of the convolution can be organized in the ($N_L \times M^2$) matrix $\mathbf{X}_j$ defined as follows

$$\mathbf{X}_j = [\mathbf{x}_j^{(A_{c_m}=1, A_{c_l}=1)} \; ... \; \mathbf{x}_j^{(A_{c_m}=M, A_{c_l}=M)}] \tag{3.37}$$

[1] The number of values to be explored as possible emission for interfering colors is M^2 since each one can emit independently M symbols, so $m^"$ is the number of combinations.

where $N_L = N_P + N_{eq} - 1$ is the number of samples of the equalized sequence by considering also the equalizer length N_{eq}, and the general vector $\mathbf{x}_j^{(A_{c_m}=m, A_{c_l}=l)}$ is the output of the convolution

$$\mathbf{x}_j^{(A_{c_m}=m, A_{c_l}=l)} = \mathbf{z}_j^{(A_{c_m}=m, A_{c_l}=l)} * g_{jj}(nT_s). \tag{3.38}$$

Before proceeding two elements must be highlighted. First, the value assumed by $\mathbf{x}_j^{(A_{c_m}=m, A_{c_l}=l)}$ is influenced by several terms. In fact, by observing (3.28), (3.36) and (3.38) one can argue that $\mathbf{x}_j^{(A_{c_m}=m, A_{c_l}=l)}$ collects the samples of data emitted by the c-th LED, filtered by the channel $h_{cj}(t)$ and equalized with $g_{jj}(nT_s)$. Second, it contains also residual self-interference, filtered by the channels $h_{c_m j}(t)$ and $h_{c_l j}(t)$ and the above reported equalizer and, more, noise samples that are no more temporally white since colored by the equalizer. Since it is interesting to measure what happens every signaling time, it is possible to sum over N_L samples so as to obtain the energy of the signal, this corresponds to sum the elements of the matrix $\mathbf{X}_j$ on each column so as to obtain a single ($1 \times M^2$) row vector

$$\mathbf{q}_j = \sum_{n=0}^{N_L-1} \mathbf{X}_j[n, v] \tag{3.39}$$

whose generic element $\mathbf{q}_j[v]$ is

$$\mathbf{q}_j[v] = \sum_{n=0}^{N_L-1} \mathbf{x}_j^{(A_{c_k}=k, A_{c_l}=l)}. \tag{3.40}$$

In order to show how different elements of the transmission/reception chain impacts on term $\mathbf{q}_j[v]$, it is expanded so as to show the dependencies

$$\mathbf{q}_j[v] = \sum_{n=0}^{N_L-1} \left[\sum_{c \in \mathcal{C}} A_c s_c(nT_s) * h_{cj}(nT_s) * g_{jj}(nT_s) \right] -$$
$$\sum_{n=0}^{N_L-1} \left[\sum_{c_v \in \mathcal{C}/\{j\}} A_v s_{c_v}(nT_s) * \tilde{h}_{c_v j}(nT_s) * g_{jj}(nT_s) \right]$$
$$+ \sum_{n=0}^{N_L-1} w_j(nT_s) * g_{jj}(nT_s). \tag{3.41}$$

In order to perform detection, in the $(1 \times M)$ row vector $\mathbf{u}_j$ is gathered the useful signal at the j-th photodiode when all possible M symbol emitted by the c-th LED (with $c = j$) are considered. So, by assuming to indicate as $p = 1, ..., M$ the index of the ASK symbol emitted by the c-th LED ($c = j$), the generic element of $\mathbf{u}_j$ is

$$\mathbf{u}_j[p] = \sum_{n=0}^{N_L-1} A_j[p]s_j(nT_s) * h_{jj}(nT_s) * g_{jj}(nT_s). \tag{3.42}$$

This allow to evaluate the *distance* between two terms. The first one is the received sequence when interference subtraction is considered by accounting for all possible transmitted symbols, while the second one is the filtered version of useful signal as in (3.42). This distance, measured at the j-th photodiode depends on the symbol (p) emitted by the j-th LED (with $j = c$) and the possible interfering, from other colors, symbols (v)

$$\delta_{j,p,v} = (\mathbf{q}_j[v] - \mathbf{u}_j[p])^2. \tag{3.43}$$

By considering the three different branches, the joint measure $\Delta_{p,v}$ is defined as

$$\Delta_{p,v} = \sum_{j=1}^{3} \delta_{j,p,v}. \tag{3.44}$$

Now, by recalling that noise is Gaussian and that its components are spatially uncorrelated, the maximum likelihood criterion asking for maximizing the conditional probability can be solved according to the following criterion

$$\{\hat{A}_R, \hat{A}_G, \hat{A}_B\} = argmin_{A_R,A_B,A_G} \Delta_{p,v}, \tag{3.45}$$

by recalling that the indexes p and v in (3.44) contains p, l and m and that when j is the red photodiode, l and m refer to the symbol emitted by green and blue respectively, when j is the green photodiode, l and m refer to the symbol emitted by red and blue respectively, while if j is the blue photodiode, l and m refer to the symbol emitted by red and green respectively.

Remark - about optimality and complexity

The presented scheme is not the optimal one to solve the problem of interference mitigation and channel equalization since the optimal solution requires to have a 3×3 set of Wiener filters in order to equalize both the direct channel, for example $h_{RR}(t)$ and the interfering ones. However, the use of OAF filters allows the receiver to work with signals (on each branch) in the presence of reasonable signal to interference ratio. Moreover, as already specified, this solution with respect to the optimal one is less costly since it has 3 filters in place of 9. Moreover, even though the use of 3 equalization filters may appear more complex with respect to a single

Table 3.3: Model Parameters

LED Transmitters	
Red wavelength	627 nm
Green wavelength	530 nm
Blue wavelength	470 nm
Maximum transmit power	1.1 W
Beam angle	$125°$ Full Width Half Maximum
Focus lens angle	$60°$
Receiver Telstore C7718	
FOV	$65°$
wavelength range	400 nm - 700 nm
maximum sensitivity wavelength	500 nm
Area	1.75 mm^2
Effective area A_e	5 mm^2
Receiver Vishay BPW34	
FOV	$65°$
wavelength range	430 nm - 1000 nm
maximum sensitivity wavelength	850 nm
Area	0.78 mm^2
Effective area A_e	3.3 mm^2

equalizer operating on the three components, it can be argued that the channels are shorter if compared with the whole channel (RGB to a single photodiode) so reducing the complexity of each equalizer. Finally, the cost in the detection phase is M^3 since this latter is the number of elements to consider in (3.45). ■

3.3.3 Numerical results and implementation

The performance of the proposed system have been evaluated through numerical computer simulation especially for what concerns performance comparison with systems in the literature. Moreover are also presented performance evaluation by basing on tests held on the implemented version of the presented scheme. For what concerns LEDs, are used the Luxeon Star Rebel Red, Green and Blue whose features can be found in [39]. In Table 3.3 are summarized the key features. Regarding photodiodes two different families have been considered. The first one has a higher raise fall times with respect to the second one hence it can introduce ISI if the symbol rate is too high. This allows to test the equalization procedure. On the other hand the second kind of photodiode has lower raise fall time so reducing the need for equalization. In particular the first kind of photodiodes is Telstore C7718 whose features can be found in [40] while the second kind of photodiodes is Vishay BPW34 and presents the features described in [41]. It is worth to highlight here that the rise-fall time of the Telstore C7718 is 500 ns while the rise-fall values for Vishay BPW34 is 100 ns. Key features are summarized in Table 3.3. About the lens it is used a sixty degrees beam angle.

Performance comparison have been done with the work presented in [7] where a 4-ASK modulation is used. Recalling that white-light is used in [7], while RGB LEDs are considered for our system. The RGB LEDs characteristics are provided in Table 3.3. Furthermore the signal generation is driven with a square root raised cosine signal as in [7] with signalling period T_P equating 100ns. This assumption leads to have for the system

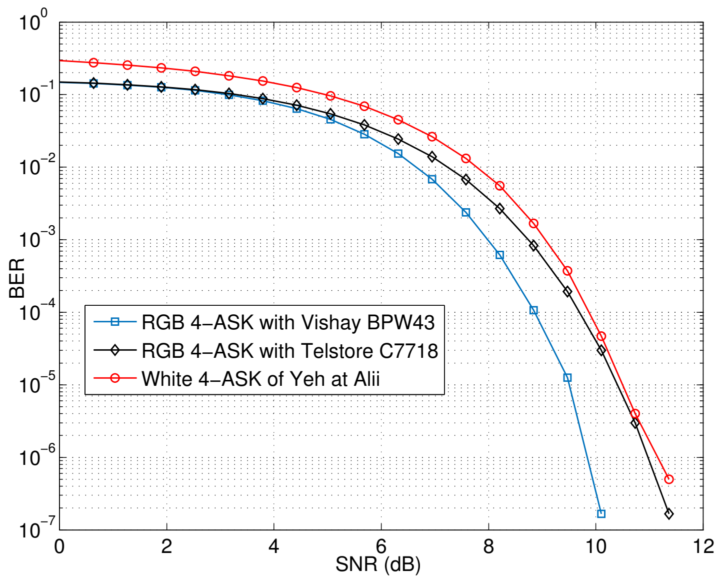

Fig. 3.13: BER comparison between the proposed scheme with Vishay BPW34 and Telstore C7718 photodiodes and work in [7].

three times the rate of the scheme in [7] when 4-ASK is used, that is 60 Mb/s since three LEDs are used in place of one while [7] achieves 20Mb/s. The channel is simulated by using MATLAB based CandLES tool [42]. While the Finite Impulse Response (FIR) filter proposed in [7] has 13-taps length and a particular setup is performed in order to guarantee convergence, no special setup is needed in the presented scheme and the periodical (i.e. every 2000 symbols) re-estimation is performed without memory, that is, from scratch. In Fig.3.13 is reported BER by considering different illumination levels for the light sources. Fig. 3.8 shows that the proposed RGB-ASK system achieves lower BER values. In particular using a Vishay BPW34 photodiode leads to better performance with respect to use Telstore C7718 since the equalizer is shorter and more reliable so equalization performs better. The gain offered by the proposed scheme can be justified by observing that the presence of self-interference can help the detection since it is based on the knowledge of possible amplitudes associated to the other color components.

Some schemes proposed in the literature are able to achieve higher rates. This is essentially due to two aspects. First, the bandwidth used is higher, thus meaning, higher symbol rate. Moreover, high-order constellations are used at very few centimetres and the performance falls short when distance increases. In order to measure the performance of the presented system

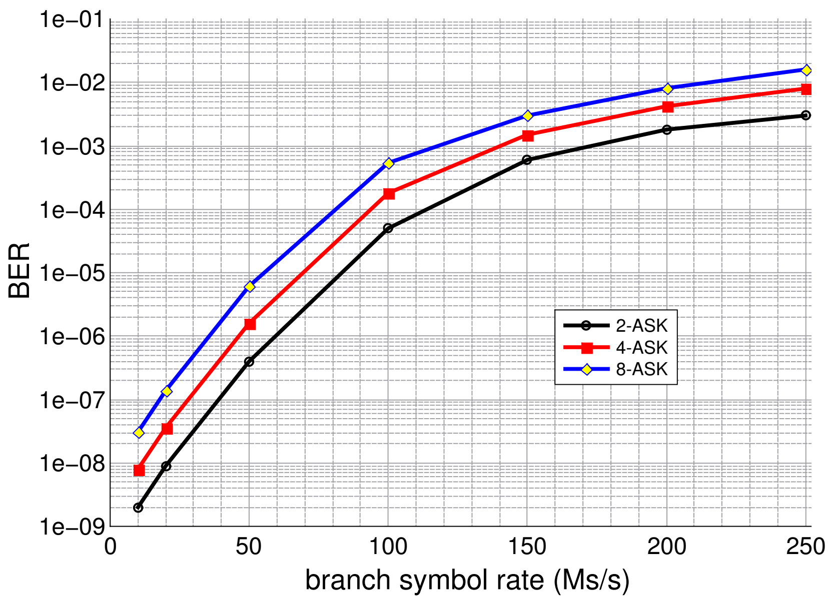

Fig. 3.14: BER for different values of symbol rates on each transmitting branch and modulation order.

with respect to the symbol rate, since this latter aspect both consider higher transmitting rates and, more, channel impairments, in Fig. 3.14 is reported the achieved BER when 2-ASK, 4-ASK and 8-ASK are considered and symbol rate on each branch is on the horizontal axis. Hence the transmitted rate is given by the product of symbol rate and the term $3\log_2 M$ where M is the modulation order, so when 10Ms/s is considered it is ranged from 30 Mb/s of 2-ASK to 90 Mb/s of 8-ASK. On the extreme right side, a symbol rate of 250 Mb/s deals to a rate of 750 Mb/s for 2-ASK till to 2.25 Gb/s for 8-ASK. The computer simulations refer to a distance of 80 cm while for increasing the symbol rate the signaling time is reduced. Fig. 3.14 shows that for relatively low rates (values below 50 Mb/s, that is rates ranging from 150 Mb/s to 450 Mb/s) BER is below 10^{-5} while it increases when considering higher rates. It is worth to highlight that no coding is present here thus meaning that, in example, the error rate can be reduced with a coding scheme as block coding even though a the expense of reducing net rate.

Implementation

In Fig.3.15 is reported a picture of the implemented system as schematically reported in Fig. 3.10 when the transmitter and receiver have 30 cm distance for sake of picture representation. It is possible to recognize the LEDs and the lens as well as the OAFs with the Arduino (receiving) board. The emission is driven via a Arduino-Due signal generator and control

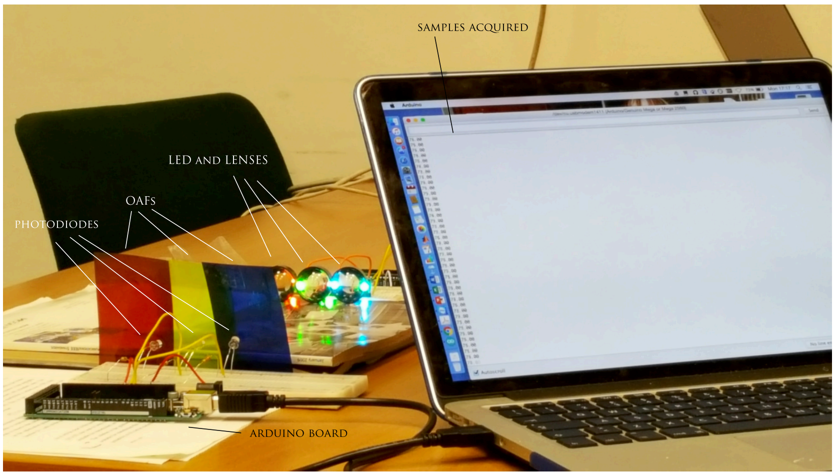

Fig. 3.15: Picture of the implementation of the system. On right hand side transmitter, on left side receiver with AOFs.

board. Also the receiver is reported and it is possible to recognize that the photodiodes have an OAF each tuned on a different color. The three lenses are posed at 3 cm from each LEDs and in the reported results the receiver is posed at 97 cm from the transmitter if not differently specified. The signal is acquired with a Arduino-Due board sampled with 10 quantization bits via the USB/serial port. The data are then visualized and saved on a dialog windows controlling the serial port. After all the data are imported on Matlab where operations like, channel estimation, channel equalization and data detection are performed.

In order to both test the performance in terms of BER and check the validity of simulations in the previous subsection, in Fig. 3.16 is reported BER as a function of distance between transmitter and receiver, when Vishay BPW34 photodiodes are used for 2-ASK, 4-ASK and 8-ASK. More in detail, about simulation set up, the illumination level is the same while the rate is different. In fact, for 2-ASK is achieved 28 Mb/s, for 4-ASK 56 Mb/s and 8-ASK 84 Mb/s. It is possible to appreciate that the difference between the implementation results (continuous lines) and simulated ones (dash lines) is really limited. As expected, 8-ASK performs worse with respect to 4-ASK and 2-ASK even though 8-ASK achieves higher bit rate. By recalling that the power is only 1 Watt, at 1 meter the performance for 2-ASK and 4-ASK are around/below a BER of 10^{-3}. In Fig.3.17 it is discussed

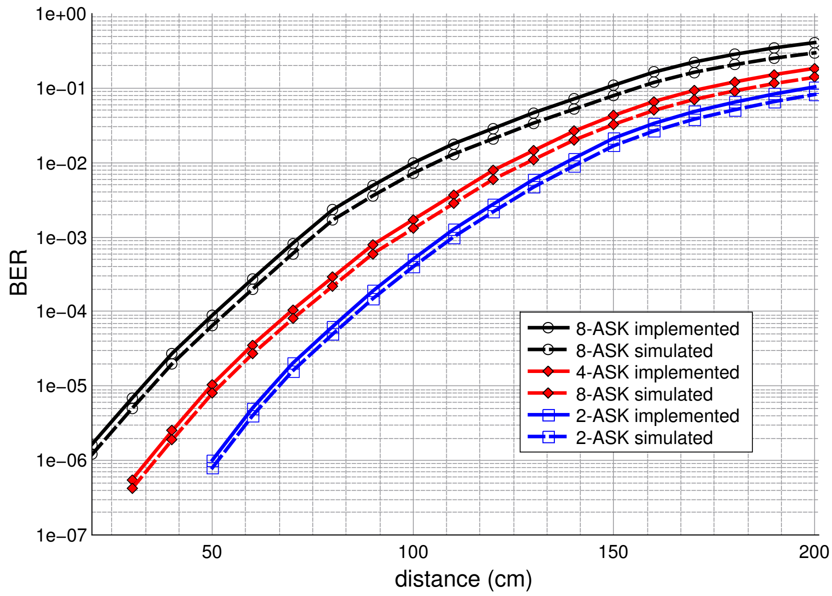

Fig. 3.16: BER evaluation as a function of distance.

the role played by training. In fact, BER is detailed when the frequency of training symbols decreases. Having a low training frequency means that the receiver is not updated about possible channel changes, while a frequent training signaling allows to be updated at the cost of lowering the net transmission rate. In order to test the behavior of the system when channel changes, the receiver is slightly moved with respect to its initial position that is 40 cm, 10 cm ahead and 10 cm back on a small carriage at a speed of approximately 5cm/s so as to induce changes in the channel and test the behavior of the system. In this case the use of Vishay $BPW34$ and Telstore $C7718$ photodiodes is compared for 2, 4 and 8-ASK. It is possible to appreciate in Fig. 3.17 BER as a function of much frequent estimation is performed. So, a value of ten means that training symbols are sent every 10 data symbols (and this reduces the data rate of 9%). In Fig. 3.17, all the configurations, that is, photodiodes used and modulation format, present constant BER values till to the case of training symbols sent every 1000 data symbols (rate reduction 0.1%). When the case of 10000 symbols sent without any training is considered, BER increases till to achieve values of the order of $10^{-7} \div 10^{-6}$. When the training becomes more and more sporadic the performance falls short since BER achieves values around $10^{-2} \div 10^{-5}$. From this, it is possible to conclude that sending training every 1000 symbols is a very good compromise when the movement of the receiver is in line with the above described behavior. Vishay photodiodes performs better since the equalizer is shorter (in terms of number of samples) with respect to that required by Telstore one, since the former is able to *follow* the symbol rate. However its gain with respect to a less performing photodiode is limited. Higher BER values achieved for sporadic signaling are due to the outdated version of the channel available at the receiver since it uses for detection mechanism an *old knowledge* of the channel and, by considering that changes in distance and angle incurs, the variations can be sensible.

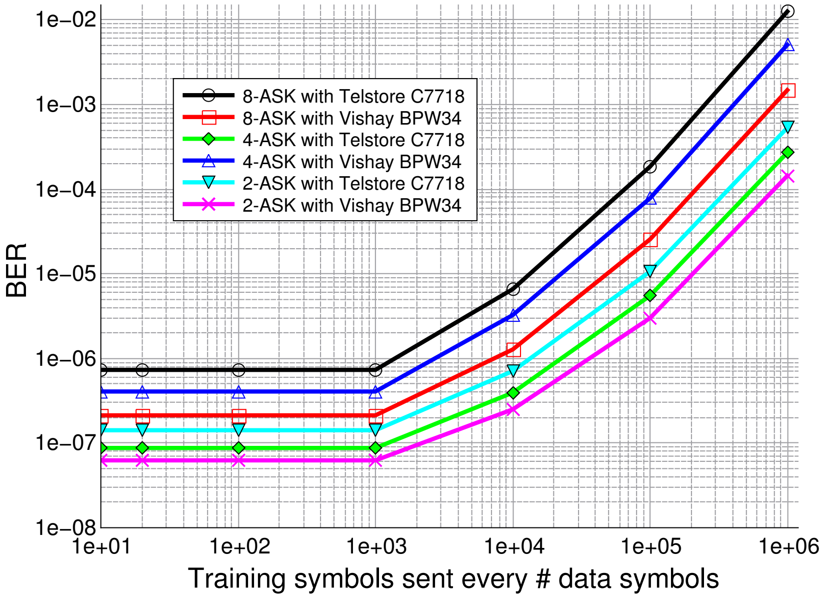

Fig. 3.17: BER evaluation as a function of training sequence frequency when the receier is moving.

Chapter 4

Visible Light Localization

In Sec. 2.4 the application areas where VLC technology can create the major benefit were presented. Among them, there are location based services, which take into account the device's geographical location to offer addition services as navigation, dedicated advertaising, safety information and much more.

Generally speaking, it is challenging to acquire a device position when it is not located in an open field. In other words, localize in an indoor environment can be more difficult than outdoor, while the global positioning system (GPS) performs well outdoor and it is widely used for this purpose. The walls attenuate RF signals and can limit the accuracy of the position estimation of the receiver, thus for indoor positioning other technologies are preferred. The importance of having a reliable positioning system indoor is related to the availability of the amount of new automatic object location detection services [43], like location detection of products stored in a warehouse, medical personnel or equipment in a hospital, and localization based services for indoor navigation or dedicated marketing information, like indoor navigation in a large mall.

For this reasons the use of VLC for indoor localization has become very popular in recent years, and localization applications that use the signals coming from the ceiling lights, it is considered the pivotal application in order to led the widespread presence of VLC in the market [44].

Different technologies and products are available for indoor positioning and navigation. Before proceeding with the study of VLC-based positioning techniques, it is worth to summarize the different available technologies. Possible competitors of VLC are (*i*) fixed indoor positioning systems, *i.e.* infrared positioning systems [45], ultrasonic positioning systems [46], RF positioning systems [47], and Ultra Wideband (UWB) systems [48], and (*ii*) pedestrian indoor positioning systems, *i.e.* Beauregard's system [49], FootSLAM [50], and Fischer's system [51].

Differently from VLC, some systems, even if they can provide good localization accuracies, they cannot add to the network the possibility of using the same installed system also for high data rate communication purpose.

Considering infrared positioning systems, they must respect stricter eye safety requirements. Using passive infrared system has an addition drawback, it is not able to distinguish, for instance, between a person equipped with a device (*e.g.*, a smartphone) willing to connect with Li-Fi to the Internet, and any another person with no concern on the Internet connection at all. Regarding Ultrasonic Positioning Systems, in [46] the use of broadband ultrasound is explored by taking into account a direct sequence spread spectrum technique as opposed to narrowband one employed in the Bat system [52]. The performance achieved by such systems is good and reliable. However, the use of spread spectrum techniques is not affordable at low cost since the hardware is based on piezo-electric transducers. UWB solutions require a dedicated hardware with a very precise clock-synchronization and suffer for interference due to the large bandwidth. Other wireless solutions based on opportunistic signals *e.g.*, IEEE$802.11x$, may be convenient since nowadays all smartphones are equipped with a proper IEEE$802.11x$ module, even if the presence of access points is not always granted. Finally, for access points working on the same band, ambiguity issues in positioning estimation can occur.

By considering the pedestrian indoor positioning systems, some research effort looked for different approaches as Pedestrian Dead Reckoning (PDR). In [50] a Bayesian estimation approach that achieves simultaneous localization and mapping for pedestrians is presented. FootSLAM uses odometry obtained with foot-mounted inertial sensors. This technique is able to maintain an error in the range of one meter in typical indoor environments over extended periods of time, although for non-ideal sensors the errors are cumulative and the growth in uncertainty is unbounded over time. In [49], the authors show how a Backtracking Particle Filter can be combined with different levels of building plan detail to improve PDR performance. Using only external wall information, they yield positioning performance of 2.56 m mean two-dimensional (2D) error, that is greatly superior to the PDR-only *i.e.*, no map base case (7.74 m mean $2D$ error). However, in both cases, is not possible to reach very high-precision position estimation. To get better position estimation for pedestrian indoor positioning, the Fischer system's [51] uses ultrasound nodes as landmarks to correct the drift in PDR. Notice that in all the aforementioned pedestrian indoor positioning systems, users are compelled to wear foot-mounted inertial measurement units.

4.1 VLC Localization Literature

Dealing now with VLC, in the literature there are several techniques for VLC-based positioning, differentiating the metric that provides information on positioning (*i.e.*, power or time-based), and the algorithm for location estimation. A number of techniques have been proposed and studied for indoor location sensing, most using a positioning technique based on triangulation, fingerprinting, and proximity. To use the triangulation technique, it is required to measure the angle or distance between a reference point and a mobile terminal, such as Angle Of Arrival (AOA), Time Of Arrival (TOA) and Time Difference Of Arrival (TDOA) [53,54], and Received Signal Strength Intensity (RSSI) [55–58].

In [53], Nah *et al.* propose a localization scheme based on the TDOA coherent heterodyne detection method. They assume at least three LED lamps, each of them can transmit on a frequency ID. The TDOA is then measured by detecting the phase difference between the transmitted signals. Similarly, in [54] Jung *et al.* estimate the locations of an object in the room, by means of three LED lamps, where each LED lamp has a unique frequency address (F-ID). In [59], a location system for an underground mining environment is proposed, the positioning is provided by an algorithm that estimates the state of the optical channel prior the application of the trilateration technique using several fixed reference points. The goodness of this approach is related to the number of reference points; in fact, using 3 LEDs and with an hypothetically infinite number of reference points the estimation error can reach the order of few cm, while increasing up to 1 m even with 13 reference points.

Furthermore, many works have proposed a positioning technique based on RSS measurements. In [55], Yang *et al.* consider a positioning algorithm based on RSS measurements from at least three white LEDs arrays transmitters. The greatest advantage of RSS method is that the accuracy of the system is irrelevant with modulation scheme, and system bandwidth. In [56], the same authors have presented a 3D RSS-based positioning system comprised of a set of LEDs, each using a different RF subcarrier to reduce a possible inter-cell interference by adjacent LEDs. Results have shown a positioning error of less than 3 cm in indoor environment.

In [60], Hu *et al.* provide a few experiment results of an optical channel model suitable for indoor localization purpose. The authors adopt a

Binary Frequency Shif Keying (BFSK) modulation and channel hopping to achieve reliable location beaconing from multiple, uncoordinated light sources over a shared light medium. The system can provide a localization accuracy ranging from 0.4 m to 0.7 m. An other work is investigated by Kim *et al.* in [58]. The authors proposed an algorithm for estimating the position of a mobile station by comparing the received light intensity at the receiver with the pre-calculated light intensity at a t position. A very similar approach is proposed by Jung *et al.* in [57], where the proposed system uses strength ratio between received signals to obtain distance ratio, and provides accurate location information with low complexity.

Other approaches for positioning via VLC are based on the use of image sensors [61, 62]. In [61], Rahman *et al.* propose an algorithm for high precision indoor positioning and consider a LED lighting array as VLC transmitter, while two image sensors receive and demodulate the positioning information of all the reference LEDs. The system performs the optical intensity modulation of the LED illumination for data transmission, and receives the light by using image sensors. The unknown position is then calculated by using the position information of the reference LEDs, together with the geometric relationship of the images on the two image sensors.

Furthermore, in [63] Sertthin *et al.* consider a two-dimensional VLC-based positioning system, by using VLC Identification (VLC-ID), a photo detector and a 6-axes sensor (*i.e.*, a geomagnetic sensor and gravity acceleration sensor). This approach results presents higher accuracy than simple VLC-ID based positioning system, also due to a proposed Switching Estimated Receiver Position (SERP) scheme. In the conventional positioning scheme, a single Estimated Receiver Position (ERP) is used, where the only way to reduce the estimation error is by decreasing the receiver's FOV. On the other hand, SERP improves the positioning accuracy by optimizing estimated error distance, which is varied in proportion to the receiver's tilt angle. Indeed, the ERP is switched depending on the receiver's tilt angle, in order to limit the estimated error distance. Experimental results have shown the improvement of SERP with three types of FOV receivers. then obtaining more than 30% improvement of accuracy as compared with the conventional position estimation scheme.

Leveraging on all previous works on positioning via VLC, it is possible to see that approaches based on RSS measurements are the most investigated, as well as TDOA-based ones. However, approaches based on a single metric (*i.e.*, TDOA only, and RSS only) can present a few limitations and issues (*e.g.*, the inter-cell interference, and interfering signals). Other solutions should be considered as auxiliary approaches, in order to overcome such issues (*i.e.*, interference, synchronization, and timing). For example, in [64] the authors present a Carrier Allocation VLC system, where different radio frequency carriers are used for signal modulation, in order to overcome the inter-cell interference in indoor environments. Analogously, the transmission time of signals need to be managed to avoid the overlap of received signals without the inter-cell interference.

Last, even though segmented position sensing detectors can be used for localization purpose (see [65]), the major concern with this approach is that it is not compatible with communication aim as proposed in the literature for VLC systems, since it is unable to manage different users, as well as modulating signals.

4.2 Localize with RSS-TDOA

This chapter is based on the publication [66], where it is presented an hybrid centralised positioning scheme that is a combination of two metrics, RSS and TDOA. Rather than the absolute arrival time, like in TOA, the aim of TDOA is to determine the relative position of the mobile transmitter by examining the difference in time at which the signal arrives.

For describing the localization technique, it is considered a MIMO VLC system model according to the following expression, which identifies the k-th output signal of the k-th LED and its effect on the u-th node (photodiode):

$$Y_{ku}(t,\vartheta,\varphi) = rA_e(\vartheta,\varphi)X_k(t,\vartheta',\varphi') * h_{ku}(t) + N(t) + W(t), \tag{4.1}$$

where r [A/W] is the responsivity of the photodiode, A_e [m^2] is the effective receiver area, $X_k(t,\vartheta',\varphi')$ is the emitted power waveform [67], depending on time t and space (ϑ',φ'), and $N(t)$ is the shot noise due to ambient light, while $W(t)$ is the thermal noise.

This system model will be used also in the next chapter, dealing with MIMO transmission.

Under the assumption of the k-th channel impulse response $h_{ku}(t)$ is ideal *i.e.*, $h_{ku}(t) = a_{ku}\delta(t)$, with $a_{ku} \neq 0$ as a constant [1]:

$$Y_{ku}(t,\vartheta,\varphi) = rA_e(\vartheta,\varphi) \cdot a_{ku}X_k(t,\vartheta',\varphi') + N(t) + W(t), \tag{4.2}$$

and for $[N(t) + W(t)] \to 0$, (4.2) becomes

$$Y_{ku}(t,\vartheta,\varphi) = rA_e(\vartheta,\varphi) \cdot a_{ku}X_k(t,\vartheta',\varphi'), \tag{4.3}$$

[1]This refers to a directed Line-of-Sight (LOS) channel.

where the term a_{ku} and $X_k(t, \vartheta', \varphi')$ consider respectively the distance from the receiver to the transmitter, and the intensity emission on the angular directions (ϑ', φ'). By considering the presence of multiple LEDs and photodiodes in a number of n_T and n_R respectively, it is possible to represent in a discrete time fashion, the space-time samples received by the u-th node, as follows

$$\mathbf{Y}_u = \mathbf{X}\mathbf{H}_u + \mathbf{W} + \mathbf{N}, \tag{4.4}$$

where the $(n_T \times n_R)$ $\mathbf{H}_u$ matrix models the behavior of the channel, while the $(LT_s \times n_T)$ $\mathbf{X}$ matrix collects the symbols emitted by the n_T LEDs over L time slots, each of length T_s. The $(LT_s \times n_R)$ sum matrix $\mathbf{W} + \mathbf{N}$ gathers the noise terms as previously specified.

The above model is a discrete-time representation of what is present at the receiver photodiodes. Each of the n_R photodiodes receives n_T analog signals coming from the n_T transmitting LEDs and filtered by the channels. When multiple LEDs are available at the transmitter side, the columns of $\mathbf{X}$ are the discrete time representation of what is emitted by the LEDs. In particular, by selecting the i-th column and by spanning its elements, it is possible to identify what the i-th LED is transmitting. On the other side, by observing the n-th row, it is possible to appreciate what all the available LEDs are emitting at the n-th time.

The technique presented in this chapter, which is used to localize the nodes in the network, is based on the coordination of signaling by means of PPM, in order to sort the n_T LEDs, and to have the possibility of measuring the RSS and TDOA of the pulses. This allows to estimate n_T distances and detect the positions in the room. The displacement of the LEDs in the ceiling of the room and the number n_T of LEDs are important for avoiding or limiting ambiguity. In fact, if only one LED is used for estimating distance, this does not suffice for understanding where a node is located and, in general, it can lay on a circle, as a projection on the floor of a cone with the vertex on the LED [68]. Two LEDs reduce ambiguity since the node can be in two mirrored points with respect to the segment connecting the position of the two LEDs. So the minimum number of LEDs allowing the unambiguous estimation of the position is three [68].

Furthermore, the LEDs position is important in order to grant sufficient coverage to the room, thus meaning that it should be avoided the possibility of having some black zones, where the signal does not guarantee good localization and connectivity. Moreover, if the localization mechanism is considered in conjunction with a MIMO transmission scheme, it is important to have a true spatial diversity gain that depends on the LEDs displacement that should also assure the statistical independence of channel paths.

the pulse emitted by the k-th LED is expressed as:

$$X_k(t, \vartheta', \varphi') = P_{[loc]}(t - (k-1)T_s, \vartheta', \varphi'), \tag{4.5}$$

where T_s is the previously defined slot time. Each pulse (of T_p length) must be spaced apart for a time of the order of the propagation delay so as to avoid overlapping pulses due to different distances from LEDs. Fig. 4.1 shows how this coordination works for the n_T LEDs. It is possible to appreciate that each power waveform coming from a LED can exhibit different delay, in fact the transmitted sequence (upper Fig. 4.1) presents different horizontal distance (time) with respect to the received one (lower Fig. 4.1). The signal received by the u-th node is, in this case,

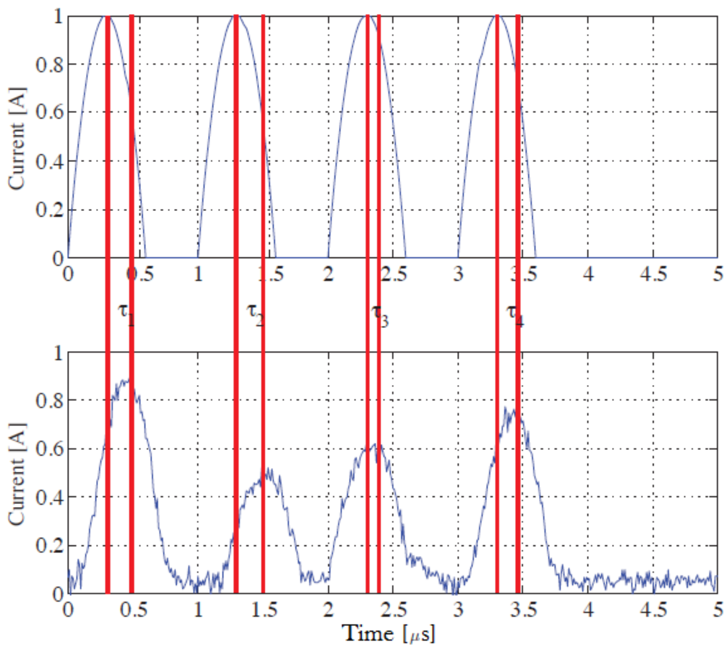

Fig. 4.1: Coordinated transmission for localization purposes. Upper and lower figure show the transmitted pulses, and the received ones, respectively

.

$$Y_u(t, \vartheta, \varphi) = \sum_{k=1}^{n_T} r A_e(\vartheta, \varphi) X_k(t, \vartheta', \varphi') * h_{ku}(t) + N(t) + W(t), \tag{4.6}$$

and is processed in order to detect the position. The position is obtained by estimating the distance d_{ku} of the u-th node from the k-th LED. Its estimation is obtained by linearly combining the information of RSS and TDOA of the pulses in the following way

$$\tilde{d}_{ku} = (1-\rho)\tilde{d}_{ku}^{(RSS)} + \rho\tilde{d}_{ku}^{(TDOA)}, \tag{4.7}$$

where the ρ parameter is a weighting factor ($\rho \in [0,1]$) used to balance the RSS estimation $\tilde{d}_{ku}^{(RSS)}$ with respect to the TDOA one $\tilde{d}_{ku}^{(TDOA)}$. The benefit of having this two metrics $\tilde{d}_{ku}^{(RSS)}$ and $\tilde{d}_{ku}^{(TDOA)}$ is that the former has performance degradation due to reflections generating overlapped pulses so increasing the pulse duration, while the latter is more sensible to amplitude fluctuations due to the presence of noise.

The localization task is performed as follows. Once available the n_T distances $\{\tilde{d}_{1u}, \tilde{d}_{2u}, \ldots, \tilde{d}_{n_T u}\}$, the coordinates are obtained thanks to the knowledge of the positions of the LEDs that, in a localization taxonomy, can be considered as anchor points. The procedure to obtain such coordinates, $(\tilde{x}_u, \tilde{y}_u)$, is based on multilateration [69], which exploits hyperboloids equations for determining the crossing points of those surfaces. So, it leads to the following system equations that can be solved via some numerical tools as Newton method (see [70]) or by linearizing the equations by summing/subtracting rows of the matrix at the left-hand-side:

$$\begin{bmatrix} (x_1-\tilde{x}_u)^2 + (y_1-\tilde{y}_u)^2 + (z_1-\tilde{z}_u)^2 \\ (x_2-\tilde{x}_u)^2 + (y_2-\tilde{y}_u)^2 + (z_2-\tilde{z}_u)^2 \\ \vdots \\ (x_{n_T}-\tilde{x}_u)^2 + (y_{n_T}-\tilde{y}_u)^2 + (z_{n_T}-\tilde{z}_u)^2 \end{bmatrix} = \begin{bmatrix} \tilde{d}_{1u}^2 \\ \tilde{d}_{2u}^2 \\ \vdots \\ \tilde{d}_{n_T u}^2 \end{bmatrix}, \tag{4.8}$$

where the general element $(x_k-\tilde{x}_u)^2 + (y_k-\tilde{y}_u)^2 + (z_k-\tilde{z}_u)^2$ equates $\tilde{d}_{ku}^2$, being $k = \{1, \ldots, n_T\}$.

About the procedures to arrive at evaluating the estimates in (4.7), the value $\tilde{d}_{ku}^{(RSS)}$ is obtained by observing the received signal strength and by storing the n_T local highest values. Analytically speaking, the receiver considers as $\tilde{d}_{ku}^{(RSS)}$ the following λ-dependent (*i.e.*, once fixed a λ value) quantity

$$\tilde{d}_{ku}^{(RSS)} = \mathcal{A}^{-1}\left(\frac{\max_{(k-1)T_s \le t \le kT_s} Y_{ku}(t,\vartheta,\varphi)}{rA_e(\vartheta,\varphi)P_{[loc]}(t-(k-1)T_s,\vartheta',\varphi')}\right)\Bigg|_{\lambda}. \tag{4.9}$$

In practice, once detected a peak *i.e.*,

$$\max_{(k-1)T_s \le t \le kT_s} Y_{ku}(t,\vartheta,\varphi), \tag{4.10}$$

within a time interval of $T_p + T_g$ seconds (equal to T_s, with T_p being the pulse duration, and T_g the guard time), a new peak is looked for in the next $T_p + T_g$ seconds till to have a single localization frame of length $n_T(T_p + T_g)$. On the basis of these measurements, by resorting to a proper attenuation model ($\mathcal{A}(\lambda, d)$) that must be available in advance, it is possible for a known value of λ to go back to the estimated distance.

On the other hand, the value $\tilde{d}_{ku}^{(TDOA)}$ is obtained by analyzing the received signal and by detecting the n_T local highest peaks. So, once detected a peak within a time interval of $T_p + T_g$ seconds, a new peak is looked for in the next $T_p + T_g$ seconds till to have a single localization frame of length $n_T(T_p + T_g)$. In this sense the estimation of the distance from the k-th LED and the u-th node can be represented by the following expression

$$\tilde{d}_{ku}^{(TDOA)} = \tau_{ku}^{(TDOA)}/v - (k-1)T_g, \tag{4.11}$$

where v [m/s] is the light speed, and the delay $\tau_{ku}^{(TDOA)}$ is given by

$$\tau_{ku}^{(TDOA)} = \arg \max_{(k-1)T_s \leq \tau \leq kT_s} Y_{ku}(t). \tag{4.12}$$

The term $(k-1)$ is due to the fact that the first LED (*i.e.* , $k = 1$) transmits a not shifted pulse. More, since there is no reference signal explicating the start of transmission (*i.e.* , a clock), the first delay is measured on the basis of the RSS criterion.

4.2.1 Localization Evaluation

The simulations of the work in [66] have been developed using the values of Table 4.1. All the performances, with the exception of those presented with a specific position of the receiver in a room, are obtained by spatially averaging the node position on the whole room.

About the SNR, it is formally defined as

$$SNR = \frac{(rP_r^{(opt)})^2}{2q(I_p + I_d)\Delta f + 4k_pTF\Delta f/R_f}, \tag{4.13}$$

that represents a worst case since optical and thermal noise components are simultaneously considered. In (4.13), r [A/W] is the already introduced photodiode responsivity and $P_r^{(opt)}$ is the received optical power, I_p [A] is the average current, I_d [A] the dark current, Δf [Hz] the detector bandwidth, q electron charge, k_p [JK^{-1}] the Boltzmann constant, T [K] the temperature, F the noise factor, and R_l [Ω] is the resistor (output) load.

Table 4.1: Model Parameters

LED Transmitter	
Maximum transmit sum power (white) P_t	1 W
Beam angle	45° Full Width Half Maximum
λ_1, λ_2, λ_3	450 nm, 530 nm, 630 nm
Room setup	
Dimensions ($l \times w \times h$)	3 m $\times$3 m $\times$3.2 m
Surface reflectivities	0.8
Ambient (DC) irradiance	5.8μW/(cm$^2\times$ nm)
4 LEDs coordinates	$(1,1)$, $(2,1)$, $(1,2)$, $(2,2)$
Photodiodes spacing	20 cm
Receiver	
FOV	$90°$
Area	15 mm^2
Lens gain factor	2.2
Effective area A_e	33 mm^2
Optical filter	450 ± 20 nm, 60% through
Responsivity @450 nm	0.2 A/W
Responsivity @650 nm	0.4 A/W

BER simulations are obtained via Monte-Carlo method. The channel model between each LED and photodiode has been obtained through CandLES simulator, [31] even if other tools can be obtained through the use of what has been presented in [17]. In the simulations it is assumed that the PPM time shift Δ equates $T_s = 12.98 \cdot 10^{-9}$ s.

Fig.4.2 shows the path of a node moving in the room (*i.e.*, red circles indicating the real position), and the position estimation (*i.e.*, blue diamonds) computed for $\rho = 0.1$. The four green squares represent the LEDs' positions *i.e.*, $(1,1)$, $(2,1)$, $(1,2)$, and $(2,2)$ meters from the origin. Additionally, the effect of a white lamp posed at $(2.4, 1.25)$ meters is considered [2].

By observing the node position, it is possible to appreciate that it is difficult to distinguish the node's real position and the estimated one, for the node moving from 0.25 m to 1.5 m along the horizontal axis. When the node approaches the lamp (*i.e.*, the node moving from 1.5 m ahead along the horizontal axis), a strong interference is present, and the performance of the localization procedure falls short.

Regarding the positioning error obtained for different values of ρ, in Fig. 4.3 are reported the behavior of the localization algorithm for $SNR = 20$

[2] In this case, only two coordinates are considered *i.e.*, x, and y.

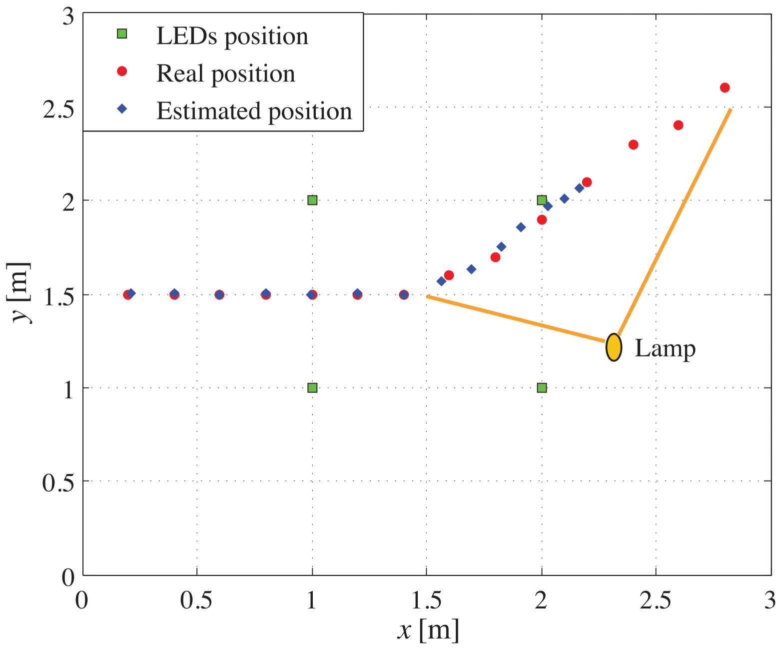

Fig. 4.2: Position estimation error (*blue diamonds*) and real position (*red circles*) of a receiver moving in a (3×3) m room, in the presence of a lamp generating disturbing white optical radiation.

dB in the room center. An interesting aspect is that performance is not monotonic with respect to ρ values. The color map reports an absolute error ranging from 5 mm to 60 mm.

In Fig. 4.3(a), the case of $\rho = 0$ *i.e.*, only RSS has been considered in the localization task, presents several red zones where the localization error is larger (*i.e.*, > 50 mm). In Fig. 4.3(b), considering the case of $\rho = 0.33$ *i.e.*, when also the estimation of the distance obtained with the TDOA is taken into account, it is possible to appreciate how the number of red points decreases so as to give evidence of a performance improvement. In fact, the area limited by the 4 LEDs achieves a cyan color that corresponds to an absolute error in the range of $[20, 25]$ mm. The case of $\rho = 0.66$ is reported in Fig. 4.3(c), thus meaning that more importance is given to TDOA with respect to RSS. The absolute error map contains several blue-cyan points, while red regions are still present at the room corners, since in such positions the local SNR is low and does not allow reliable performance, reaching values of 60 mm, as in the case of room center. Finally, when only TDOA is taken into account (*i.e.*, $\rho = 1$), the performance quality decreases, as shown by less blue-cyan points, and the map is quite similar to the case

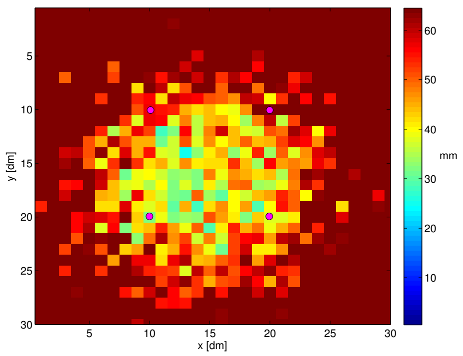

(a) $\rho = 0$

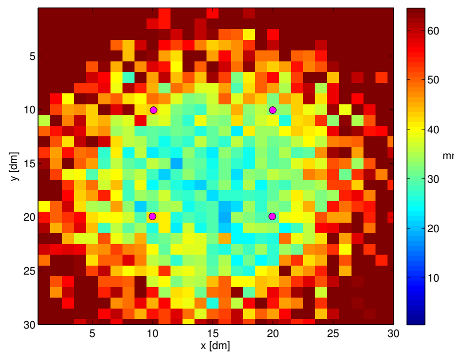

(b) $\rho = 0.33$

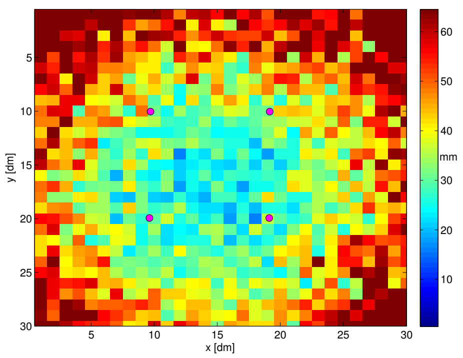

(c) $\rho = 0.66$

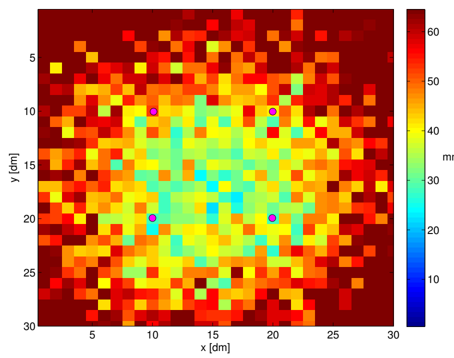

(d) $\rho = 1$

Fig. 4.3: Error Map for different values of ρ parameter and $SNR = 20$ dB at the center of the room. The red circles represent the positions of LEDs. Notice that [dm] stands for decimeters.

of $\rho = 0.33$, but with less blue-cyan points.

More, dealing with the error with different values of ρ, Fig. 4.4 shows the performance of the localization algorithm for $SNR = 40$ dB in the center of room. In particular, it is possible to observe that all the plots present only blue points so evidencing very reliable performance.

In fact, also in this case the color map reports an absolute error ranging from 5 mm to 60 mm. The case of $\rho = 0$ has been reported in Fig. 4.4(a) and, as anticipated, blue points are present even if they are bright. On the other hand, in Fig. 4.4(b) the case of $\rho = 0.33$ gives evidence of all blue points that are less bright so meaning that the absolute error is below 5 mm. The case of $\rho = 0.66$, reported in Fig. 4.4(c), confirms the absence of monoticity

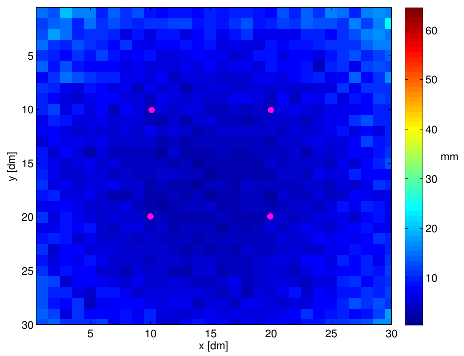

(a) $\rho = 0$

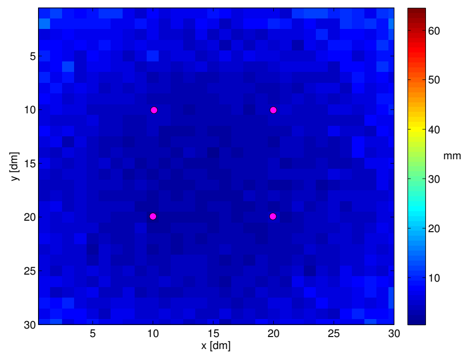

(b) $\rho = 0.33$

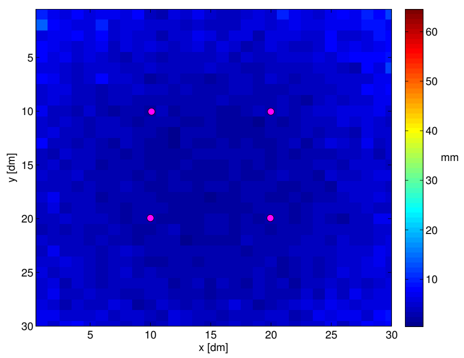

(c) $\rho = 0.66$

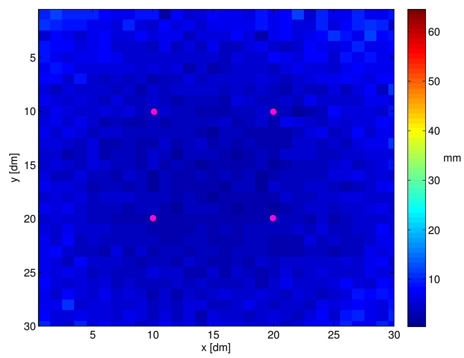

(d) $\rho = 1$

Fig. 4.4: Error Map for different values of ρ parameter and $SNR = 40$ dB at the center of the room. The red circles represent the positions of LEDs. Notice that [dm] stands for decimeters.

in the performance since the blue points are more bright with respect to those reported in Fig. 4.4(b). Finally, when only TDOA is taken into account (*i.e.*, for $\rho = 1$), the performance quality decreases since more bright blue points are present, and the map is quite similar to the case of $\rho = 0$, but with more blue-cyan points. In order to test the absolute this performance of the localization estimation, in Fig. 4.5 is reported the mean square error when $\rho = 0.33$ for 1, 2, 3, and 4 LEDs and compare them with the Cramer Rao Bound (CRB) obtained in [71]. As expected, the cases of 1, 2, and 3 LEDs are far from the CRB since this last considers the transmission of 4 LEDs. On the other hand, comparing the 4 LEDs LAST performance with CRB, the two curves are almost indistinguishable.

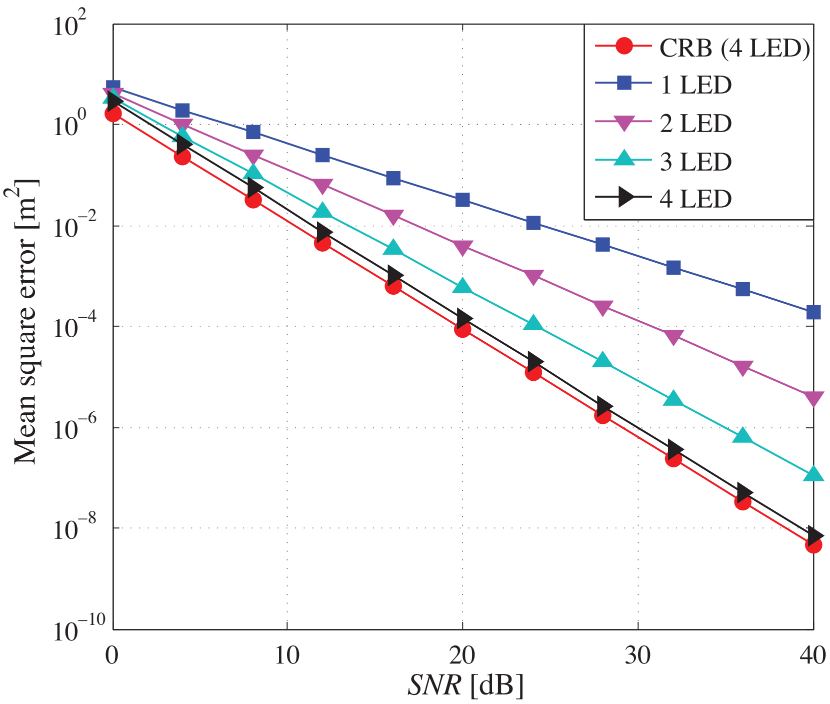

Fig. 4.5: Mean square error for different LED configurations (*i.e.*, from 1 to 4 LEDs), and Cramer-Rao Bound for 4 LEDs.

4.3 Coverage in Atto-Cells

As the number of devices that are willing to connect to the Internet increase, also the access becomes more challenging, especially when VLC networks composed by a very high number of small cells are considered. Potentially every LED can act as an access point. In the VLC indoor environment, the number of reference topologies adopted to share the medium among many users and to provide an effective coverage are basically three: I) a dedicated Access Point (AP) for every user, II) a single AP for a whole room, III) a cellular based architecture. For a very high-speed data rates, of course, the preferred option would be to use the AP topology, but the purpose here consists in providing high data rate, wider coverage area and link availability at all times for receivers that change position. So in this case a cellular structure would be the favoured option. Because of the dual use paradigm, illumination and communications, the LEDs placement affects the performances of the communications.

In fact, unlike the classic cellular communications, or Wi-Fi, in VLC the cells can be very close to each other and the handover can be very frequent.

So the handover has a higher impact on communication performances. Thanks to the directivity of LEDs, the signals is confined into a precise area, and so users can be orthogonalised depending on the position in the room, by spatial division multiple access. For other users in the same room, time division multiple access is considered. It is interesting to know which is the best cell size for maximizing the average rate achieved by users.

The following sections present the work published in [72] where the optimization of the average user net rate is taken into account.

4.3.1 Footprint-based rate optimazion problem

Assuming a rectangular room with x indicating one dimension and y the other. This leads to have a room area equating xy as depicted in Fig. 4.6 with room height given by h. The analysis carried out is valid for any plane parallel to floor, where the height of plane depends on where devices accessing are expected to be. Once recognized that the LED footprint is a

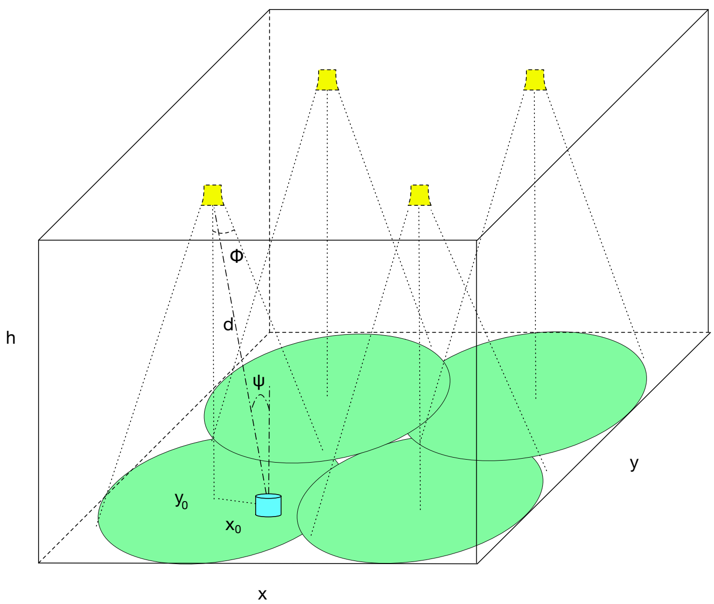

Fig. 4.6: Representation of a room with four LEDs and their footprint.

circle of A_{LED} area, the number of *cells* N_{c} is approximately given by

$$N_{\text{c}} = \frac{xy}{A_{\text{LED}}}. \tag{4.14}$$

Some words must be spent about the relationship in (4.14). The assumption of rectangular area badly fits with circled footprint. This is because if tangent circled are assumed, some zones of the room may result uncovered by LEDs. In order to solve this issue, partially overlapping LEDs coverage is considered. Once assumed the presence in the room of U users accessing the medium in an orthogonal fashion (for example TDMA as in [73]), the average rate achieved by a user in a cell is given by

$$\bar{R}_{\mathrm{u}} = \begin{cases} \frac{R_{\max} N_{\mathrm{c}}}{U}, & N_{\mathrm{c}} \leq U \\ R_{\max} & N_{\mathrm{c}} > U \end{cases} \tag{4.15}$$

$R_{\max}$ being the maximum rate and the term U/N_{c} measures the rate per user per cell. A quick look to the expression (4.15) shows how, when only one cell is considered, the rate per user is $R_{\max}/U$. More the expression is differentiated for $N_{\mathrm{c}} \leq U$ and $N_{\mathrm{c}} > U$. In fact, if $N_{\mathrm{c}} \leq U$, under the assumption of uniformly distribution for the users, the average rate per user is given by $\frac{R_{\max} N_{\mathrm{c}}}{U}$ while when the number of user is smaller than the number of cells ($N_{\mathrm{c}} > U$), it is possible to argue that a user accesses with an average rate equating the maximum rate under the hypothesis of non-adaptive modulation (still under the assumption of users uniformly spatially distributed). When a user moves within the room, it may happen that another LED, with respect to the current one, provides connection, so handover procedure must be operated. Assuming that this happens with the transmission of D_{HO} control data at a rate equal to R_{HO} so the handover time duration is $\Delta_{\mathrm{HO}} = D_{\mathrm{HO}}/R_{\mathrm{HO}}$. Hence, the objective is to maximize the average user net rate (also named average equivalent rate $\bar{R}_{\mathrm{eq}}$) expressed as

$$\bar{R}_{\mathrm{eq}} = \eta \bar{R}_{\mathrm{u}} \tag{4.16}$$

η being a term able to take into account for the time spent in handover procedures with respect to communication time. In other words, the equivalent rate $\bar{R}_{\mathrm{eq}}$ is the average user net rate with respect to the transmission of data and signalling for managing the connection by LEDs. The term η is defined as follows

$$\eta = \frac{\frac{D}{\bar{R}_{\mathrm{u}}}}{\frac{D}{\bar{R}_{\mathrm{u}}} + T_{\mathrm{O}}} = \frac{1}{1 + \frac{\bar{R}_{\mathrm{u}}}{D} T_{\mathrm{O}}}. \tag{4.17}$$

Before proceeding, it is in need to remark that has been assumed an error free system since the rate loss, induced by possible required retransmissions caused by the non-zero Bit Error Rate (and expected to be smaller than 10^{-3} for a VLC), is negligible since it impacts for less than 0.01% of the rate thus meaning that the code rate of a possible Forward Error Correction coding allowing the achievement of the performance is close to unity. Furthermore, the term D is the amount of data that must be transmitted by LEDs to the user measured in bit, T_{O} is the signalling time. This latter can be detailed in the following way

$$T_{\mathrm{O}} = T_S + \bar{N}_{\mathrm{HO}} \frac{D_{\mathrm{HO}}}{R_{\mathrm{HO}}}. \tag{4.18}$$

In particular, T_S is the time requested for setting up the connection and D_{HO} is the data to be transmitted for handover procedure at a rate R_{HO}, while $\bar{N}_{\mathrm{HO}}$ is the average number of handovers of a user. This last can be evaluated by considering the distance walked by a user at $\bar{v}$ average speed during the download of a file of D length at a rate of $\bar{R}_{\mathrm{u}}$. Hence, the number of expected handovers is considered as the multiple of the cell diameter $2\sqrt{A_{\mathrm{LED}}/\pi}$, so:

$$\bar{N}_{\mathrm{HO}} = \frac{D\alpha\bar{v}}{2\bar{R}_{\mathrm{u}}} \sqrt{\frac{\pi}{A_{\mathrm{LED}}}} \tag{4.19}$$

where α is a number between 0 and 1 and measures the probability of moving of the most moving user. Hence, α approaching 0 indicates that the most moving user has low probability of moving or moves within a single cell, while α values close to 1 means that the most moving user is always moving in a straight way. It is worth highlighting that, choosing a value for α means to optimize the network by assuming that at least one user will have, as weighted average speed, $\alpha\bar{v}$. This does not imply that all the users must share that value. Hence, $\alpha\bar{v}$ fixes the worst case with respect to the number of handover procedures. Moreover, should be specified that the network planner should consider that when a D value is considered, not all the α values are reasonable. In fact, large D, and consequently long download times, will lead to consider high α values since it is expected that some user can move. On the other hand, when the download takes short time, the movements are really limited. In this sense, α is application dependent, since it depends on the expected amount of data to be downloaded, hence on the service offered by the network. Since the values of $\bar{R}_{\mathrm{u}}$ depend on the relationship between N_{c} and U, once assigned U, it is possible to check for the maximum of the following quantity with respect to A_{LED}

$$\bar{R}_{\mathrm{eq}} = \frac{\frac{R_{\max} N_{\mathrm{c}}}{U}}{1 + \frac{\alpha\bar{v} D_{\mathrm{HO}}}{2R_{\mathrm{HO}}} \sqrt{\frac{\pi}{A_{\mathrm{LED}}}} + T_{\mathrm{S}} \frac{R_{\max} N_{\mathrm{c}}}{UD}} \tag{4.20}$$

that can be expanded, using (4.14), to show whole dependence on A_{LED} as

$$\bar{R}_{\mathrm{eq}} = \frac{xyR_{\max}}{UA_{\mathrm{LED}} + \frac{\alpha\bar{v} D_{\mathrm{HO}}}{2R_{\mathrm{HO}}} \sqrt{\frac{\pi}{A_{\mathrm{LED}}}} + T_{\mathrm{S}} \frac{xyR_{\max}}{D}} \tag{4.21}$$

The maximum of the expression in (4.21) can be derived with respect to the dimension of LED footprint by equating to 0 the first derivative of $\bar{R}_{\text{eq}}$, by stating

$$\frac{\partial \bar{R}_{\text{eq}}(A_{\text{LED}})}{\partial (A_{\text{LED}})} = 0. \tag{4.22}$$

The equation in (4.22) can be expanded as follows

$$\left(\frac{-xyR_{\max}\left(U - \frac{\alpha \bar{v} D_{\text{HO}}}{2R_{\text{HO}}}\sqrt{\pi}0.5(A_{\text{LED}}^{-3/2})\right)}{\left(UA_{\text{LED}} + \frac{\alpha \bar{v} D_{\text{HO}}}{2R_{\text{HO}}}\sqrt{\frac{\pi}{A_{\text{LED}}}} + T_{\text{S}}\frac{xyR_{\max}}{D}\right)^2} \right) = 0 \tag{4.23}$$

that has its zero when numerator is zero that is achieved for

$$A_{\text{LED}} = \left(\frac{\alpha \bar{v} D_{\text{HO}} \sqrt{\pi}}{4UR_{\text{HO}}} \right)^{\frac{2}{3}}. \tag{4.24}$$

A final check must be performed. If the A_{LED} leads to a number of N_{c} higher than U, maximum value of R_{eq} must be find by substituting in (4.20) $R_{\max}$ in place of $\bar{R}_{\text{u}}$. It is really important to note that despite of the parameters used, i.e. room dimension, number of users, maximum rate, α, etc., this analytic approach can be always used since it offers a network planning tool that presents a different perspective with respect to literature. More, dealing with possible heuristic approaches, the proposed analytic tool allows also to evaluate how much far from the optimal solution the heuristic is.

4.3.2 Numerical results

The reference system is the one depicted in Fig. 4.6 where the LEDs placement as well as light emission is qualitatively represented. The emission from a variety of LED LOS transmitters is usually modelled using a generalized LOS Lambertian radiant intensity [3]. It is worth noticing that the modulation formats, as well as the bandwidth, are transparent with respect to this analysis, thus meaning that despite of transmitter and receiver architectures, this approach is valid starting from the $R_{\max}$ value granted by the physical layer. If not specified elsewhere it is assumed to have a room of $4 \times 4 \times 3$ m^3 covered by VLC links achieving a maximum rate of $R_{\max}$ =100 Mb/s for downloading a file of 1 Mb, with a handover data of D_{HO}= 10 KBytes and a value of user speed set to $2m/s$ with $\alpha = 0.5$. The rate for handover R_{HO} is 50 Mb/s and $U = 6$, while T_{S} =100μs.

System performance

By observing Fig. 4.7, it is possible to appreciate two interesting elements regarding the average user net rate R_{eq} as in (4.21). The first one is the non-monotonic behavior with respect to A_{LED}. This can be justified by observing that having very low values of A_{LED} leads to several handover procedures and this reduces the average user net rate. On the other hand, having

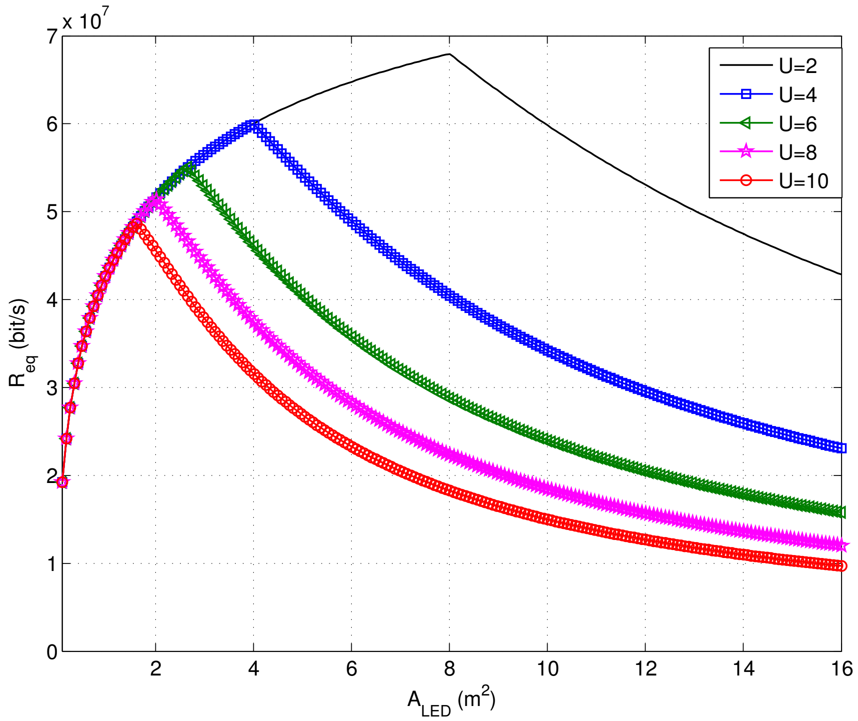

Fig. 4.7: Average user net rate achieved for A_{LED} values when different users in the network are present.

high values for A_{LED} means that in the same cell there are more users with respect to low A_{LED} values so reducing the average net rate per user. The second interesting aspect is tied to the same behavior of the curves for different U values. This can be justified by observing that the $\bar{R}_u$ value as in (4.15) equates $R_{\max}$ when $N_{\mathrm{c}} \geq U$ so the same behavior of the curves is justified by the fact that $\bar{R}_u$ equates $R_{\max}$. It is interesting to underline how the A_{LED} value allowing to achieve the maximum average user net rate changes when U changes. This is in line with what has been reported in (4.24).

By considering the effect of R_{HO} on the average user net rate, it is shown in Fig. 4.8 R_{eq} when different sizes of LED footprint are considered. It is possible to appreciate that very low rate, of the order of 100 Kb/s - 1 Mb/s induces very low values of rate since this means that the handover requires a more time to be performed. So, by increasing R_{HO} few time is spent for signaling and consequently the average user net rate increases. Interestingly,

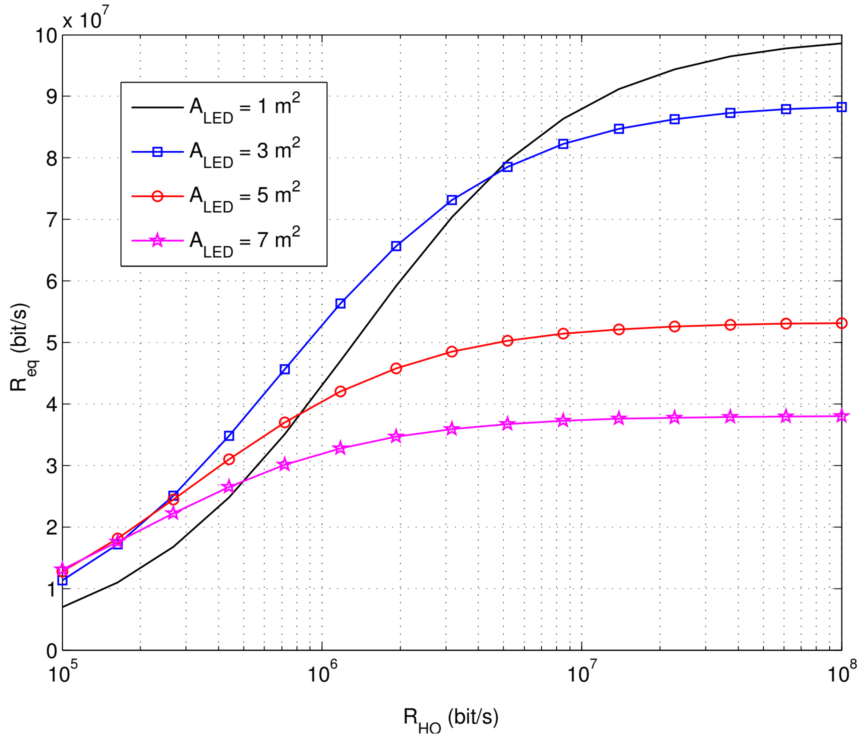

Fig. 4.8: Average user net rate achieved for R_{HO} values when different footprint sizes are accounted for.

the case of $A_{\text{LED}} = 1m^2$ is the worst at low R_{HO} while it presents the best solution for high values of R_{HO}. This can be justified by observing that $A_{\text{LED}} = 1m^2$ means to have 16 LEDs so the handover may be very frequent. However, if R_{HO} approaches $R_{\max}$ the signaling time is negligible with respect to the time spent for data. On the other hand, for slower handover procedures the average user net rate is dramatically decreased and having a high number of cells is no more worth. Having a lower number of cells (high A_{LED} values) generally leads to medium/low values of average user net rate since the cells are denser so the rate is limited by the number of users. Last, in Fig. 4.9, the average user net rate is reported as a function of α when footprint size ranges from $1m^2$ to $7m^2$ with a step size of $2m^2$. Having $\alpha = 0$ means that no user is moving in the room so the case of $A_{\text{LED}} = 1m^2$

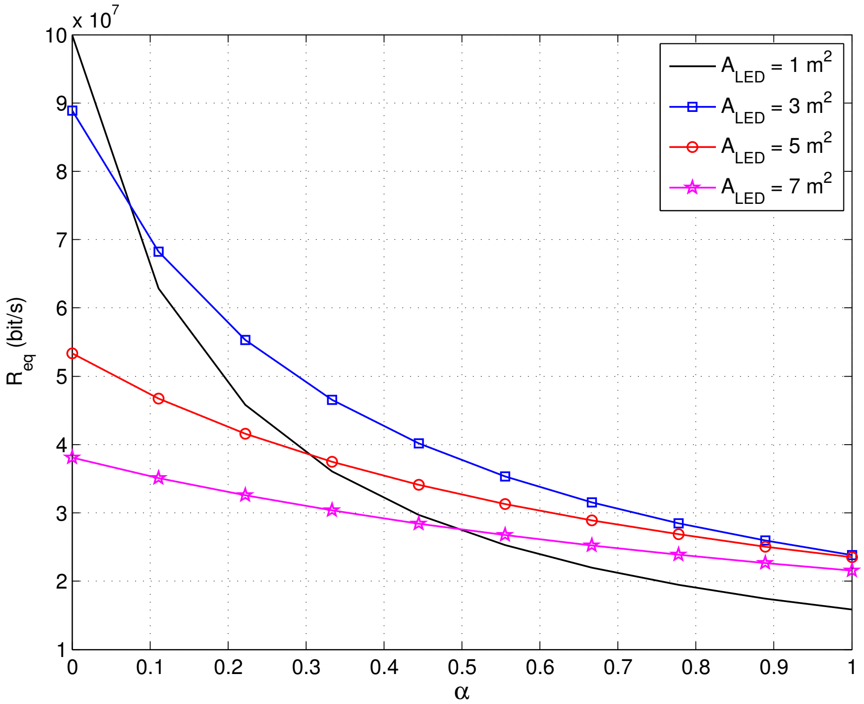

Fig. 4.9: Average user net rate achieved by considering the effect of α for different footprint size.

outperforms the others since no handovers occur and, in this regard, the cell user density is lower till one user per cell. When are considered higher α values it is assumed that handovers occur $A_{\text{LED}} = 1m^2$ solution is no more the best performing since the case $A_{\text{LED}} = 3m^2$ achieves higher net rate values. All the curves are decreasing with respect to α since higher is this parameter higher is the probability of moving of the most moving user and consequently the expected number of handover procedures increases.

Chapter 5

MIMO PPM Space-Time Block Coding

Considering the overall VLC system, the communication bottle-neck is at the transmitter side. Indeed, white off-the shelf LEDs have a modulation bandwidth in the order of few MHz, due to the long decay time of the phosphor, and even with the filtering of the blue component of the spectrum the modulation bandwidth can reach only 20 MHz without using post-equalization techniques.

For this reason, bandwidth-efficient encoding schemes, such as Pulse Amplitude Modulation (PAM) and Quadrature Amplitude Modulation (QAM), are used to increase data rate, assuming that a higher requirement for signal power is met. These have been combined with Discrete Multi-Tone (DMT) modulation to reach data rates of more than 800 Mbit/s in the lab [74,75].

The main drawback of bandwidth-efficient modulation schemes and multi-carrier schemes such as DMT is the power inefficiency. This inefficiency depends on the fact that QAM-like modulations loaded on sub-carriers are power inefficient, and moreover there is a requirement for additional energy in order to map the constellation in the first quadrant, and so a bias light is needed. Even if in the literature some schemes proposed an interesting modified version of DMT reducing the bias requested for enabling transmission (see [76] and [77]), they well perform under the assumption of Additive White Gaussian Noise (AWGN) environment without taking care of path-loss (that in general reduces the distance among symbols) and, more, these contributions do not solve the lack of power efficiency typical of QAM modulations operated on OFDM sub-carriers. The power efficient issue can grow particularly if the uplink transmission is considered.

However, within a room there is more than a single transmitter (lighter), in fact, typically, a high number of array of LEDs are present. A natural way to improve system performance is the use of spatial diversity. This requires the knowledge of how many and which LEDs are able to serve an end-user especially in large rooms; as a consequence, information about positioning can help to solve the LED discovery task. Despite this, having a module for transmission/reception and one for positioning can be expensive, so it strongly motivates the use of impulsive schemes, such as Non-Return-to-Zero or PPM for VLC, since those are schemes that can be used for both positioning and transmission. Thus the scheme used for localization presented in the previous chapter can be easily modified and integrated within a transmission scheme that uses PPM modulation. Therefore, the adoption of PPM transmission schemes can be helpful for localization, since it is possible to use the same transmitter controller (see [78]). It is furthermore interesting to evaluate how this power efficient modulation can be stressed in terms of transmission rate.

The use of MIMO together with a space-time coding technique can provide large gains in spectral efficiency. For instance, reference [79] combines Orthogonal Frequency Division Modulation (OFDM) with Spatial Modulation to provide better spectral efficiency. MIMO can highly increase the transmission capacity of a wireless optical communication system, while it does not excessively increase the spectral bandwidth [80]. Moreover, through the use of spatial diversity, it is possible to mitigate channel fading. In this chapter it is presented the use of a MIMO PPM space-time block coding transmission technique with relaxed orthogonality constraints.

Before proceeding to analyse the characteristics of the MIMO PPM modulation scheme shown in this chapter, it is mandatory to see what are the related works , dealing with MIMO techniques, from which comparison are given in the numerical results of this chapter. In the work of [81], Fath and Haas a performance comparison of VLC MIMO techniques used in indoor application is given. Several 4×4 setups with different transmitter spacing and receiver array positions are considered, as well as different MIMO algorithms *i.e.*, Repetition Coding (RC), Spatial Multiplexing (SMP), and Spatial Modulation (SM). The SM approach is a combined MIMO and digital modulation technique. Results have assessed that SM is more robust to high channel correlation, as compared to SMP, while enabling larger spectral efficiency as compared to RC. However, in [82], the authors show significant performance improvements over the work in [81], by using imaging receivers.

SM has recently been established as a promising transmission concept [83, 84], belonging to the single-RF large-scale MIMO wireless systems family. Indeed, SM can be regarded as a MIMO scheme that possesses a larger set of radiating elements, and takes advantage of the whole antenna-array at the transmitter, whilst using a limited number of RF chains. In this way, SM-MIMOs can provide high-rate systems. Again, Fath and Haas in [85] have addressed the performance of optical SM, while using narrow wavelength (colored) LEDs. Indeed, they proved that colored LEDs can improve the performance of SM by more than 10 dB, due to the fact that the responsivity of photo-diodes is a function of the optical wavelength.

Experimental studies related to VLC systems have been presented in references [86–89]. In [86], Burton *et al.* provide a demonstration of an indoor non-imaging VLC MIMO system that can achieve a bit rate of 50 Mb/s over a distance of 2 m. The system has been assessed for different detection methods *i.e.*, from the basic channel inversion to space-time techniques.

The use of diversity techniques, such as Maximum Ratio Combining (MRC), can further enhance the performance of the optical wireless system, and Space-Time Block Coding (STBC) MIMO techniques have proven to be very promising [90]. As an instance, in [8] Ntogari *et al.* introduce a diffuse Alamouti-type STBC for MIMO system, and exploit DMT in order to mitigate the effect of ISI due to the channel's impulse response. The performance of STBC systems, employing two transmit elements, is compared against SISO and MRC systems. It has been proven that STBC techniques can be used to (*i*) increase the capacity of diffuse optical wireless systems, (*ii*) improve their coverage, and also (*iii*) decrease the required optical power at the transmitter.

Moreover, the works in references [10, 91–93] deal with an approach for merging PPM and MIMO. Specifically, they propose schemes employing Ultra Wide Band radio techniques in order to translate the full diversity criterion, originally developed for non orthogonal modulations [94], for the orthogonal modulation case.

Lastly, the approaches following in references [95], [96] and [97] resort to repetition coding jointly with the use of MIMO, and also compare the performance obtained with conventional STBCs even though both [96] and [97] require the use of lasers because they are proposed for outdoor scenarios. Interestingly, these schemes perform well from a BER standpoint, but do not focus on transmission rate reduction with respect to conventional STBC schemes required to achieve the error rate gain. In other words, they aim at optimizing BER despite performance degradation in the transmission speed.

This chapter is based on the publication [98], where it is investigated the use of an optical MIMO technique jointly with PPM in order to improve the data rates, but, at the same time, taking into account the need for a reliable data transfer. PPM is known to be a power efficient modulation format, while it is bandwidth inefficient, so, as anticipated, the use of a MIMO technique can compensate the bandwidth drawback, exploiting the spatial domain. Moreover, an off-line tool for VLC system planning, including error probability and transmission rate, is presented in order to solve the trade-off between transmission rate and BER.

5.1 Space-Time PPM Block Coding

The system model introduced in the previous chapter can be easily adapted to the MIMO transmission, in fact here the main difference is to have only one user in the network. So the received signal can be simply rewritten in the following way:

$$\mathbf{Y} = \mathbf{X}\mathbf{H} + \mathbf{W}, \tag{5.1}$$

Before proceeding the discussion, it is in need to recall some important aspects of the MIMO model. The channel is flat w.r.t. the frequency response (*i.e.*, *LOS* scenario). We assume n_T and n_R as the number of LEDs and photodiodes at the transmitter and the receiver sides, respectively. The wireless-optical link is characterized by different LEDs placed on the ceiling of a room. The LEDs are required to be positioned in a way that could guarantee the sufficient light coverage (illumination), provide the communication reliability and reduce the ambiguity in indoor positioning (e.g., [99]). Moreover, the LED placement should be achieved to guarantee diversity gain, that is, spatial uncorrelation among channels. As will appear clearer in what follows, the channel features strongly influence the performance not only in terms of attenuation.

In Eq. 5.1 $\mathbf{Y}$ is the $[L \times n_R]$ matrix collecting the L-PPM symbols received by the n_R photodiodes and $\mathbf{H}$ is a $[n_T \times n_R]$ matrix, where each element in the position (i, j) is the channel path between the i-th transmitting LED and the j-th receiving photodiode. The term $\mathbf{W}$ is a $[L \times n_R]$ matrix, describing thermal and ambient noise. Last, $\mathbf{X}$ is the STBC $[L \times n_T]$ matrix that carries information according to the cardinality of L-PPM and the number of transmitting LEDs. As previously anticipated, PPM is chosen for its easy implementation, since the circuit generating pulses is the same as for On-Off Keying. It is well known from the literature that PPM is a good modulation format for reducing BER, while it has poor performance in terms of rate. This effect is counterbalanced by the use of the MIMO architecture, as it will be shown later in this work.

Equation (5.1) is a discrete-time representation of what is present at the receiver photodiodes. Each of the n_R photodiodes receives n_T analog signals coming from the n_T transmitting LEDs and filtered by the channels. The analog baseband signal can be represented by resorting to (2.5), where $X(t)$ is the signal emitted by a generic LED. When multiple LEDs are available at the transmitter side, the columns of $\mathbf{X}$ are the discrete time representation of what is emitted by the LEDs. In particular, by selecting the i-th column and by spanning its elements, we can identify what the i-th LED is transmitting; whereas by observing the n-th row, it is possible to appreciate, at n-th time, what all available LEDs are emitting.

The corresponding (analog baseband) signal *i.e.*, $y_j(t)$, measured at the output of the j-th receive photodiode[1] over a signaling period $T_s = T_p + T_g$ (with T_p the pulse period, and being T_g a guard-time interval), can be expressed in its general form as

$$
\begin{aligned}
y_j(t) &= \frac{1}{\sqrt{n_T}} \sum_{i=1}^{n_T} h_{ij}(t) * X^{(i)}(t) + W_j(t) = \\
&= \frac{1}{\sqrt{n_T}} \sum_{i=1}^{n_T} \left[\sum_{n=0}^{V} h_n(i,j) X^{(i)}(t - \tau_n(i,j)) \right] + W_j(t), \\
&\qquad \text{with } \; 0 \le t \le T_s, \; 1 \le j \le n_R,
\end{aligned} \tag{5.2}
$$

where $w_j(t)$ are the noise components at each receive photodiode, $h_{ij}(t)$ is the continuous time channel impulse response related to the channel from the i-th LED to the j-th photodiode, while $h_n(i,j)$ is the amplitude of one out of $(V+1)$ paths associated to the $\tau_n(i,j)$ delay of $h_{ij}(t)$. The normalization is to reconcile the need for equal power transmitters, that is, to compare links with the same power emitted. Moving from $y_j(t)$ to $\mathbf{y}_j[n]$ can be obtained by sampling the output at the pulse period T_p, as

$$
\mathbf{y}_j[n] = y_j(t)\big|_{t=\left[\frac{T_p}{2}+nT_p\right]}, \quad 0 \le n \le L-1. \tag{5.3}
$$

The element $\mathbf{y}_j[n]$ is the row vector representing what we receive at n-th discrete slot on each of L available photodiodes.

Dealing with the propagation scenarios, as described in chapter 2.3.1 , in the *LOS* case, the channel matrix can be represented by scalar coefficients h_{ij}, due to a very small channel length modeling the link connectivity among

[1]We assume a uniform distribution of the light on the surface of photodetector.

very close transmitting LEDs and receiving photodiodes. This reflects on good values –*i.e.*, low attenuation– of coefficients and severe path diversity loss. For the *ND-LOS* case, the reduced current at the photodiode means that the components of $\mathbf{Y}$ are smaller: this reflects on higher importance of the noise term since the $\mathbf{X}$ components are more attenuated. Lastly, the *NLOS* scenario models the partial / total absence of alignment between LEDs and photodiodes [100], and this may cause pulse overlapping if the PPM transmission rate is higher than the reciprocal of channel delay spread.

In regard to channel features, notice that different propagation scenarios imply different received signal properties. We make a special distinction between path diversity and spatially singular channels. When a *LOS* channel is considered, it is possible to have high spatial correlation so giving rise to only coding gain and no diversity gain. This does not mean to have singular channel matrices. On the other hand in the *NLOS* scenario the statistical uncorrelation among paths is highly possible.

5.1.1 Space-Time PPM Block Coding with rate issues

The matrix $\mathbf{X}$ logically describes the presence of a pulse on the time axis and the space (due to the LEDs' deployment). By considering the signal period T_s, the time length of each column is $L \cdot T_s$. Thus, the maximum rate in Spatial Multiplexing is

$$\mathcal{R}_{SM} = \frac{1}{L \cdot T_s} \log_2(L^{n_T}), \tag{5.4}$$

which becomes $\mathcal{R}_{SM} = T_s^{-1}$ in the case of $n_T = 2$ and $L = 2$, while for a single LED link (*i.e.*, $n_T = 1$) the data rate is $\mathcal{R} = 0.5 \cdot T_s^{-1}$. Notice that an increase of L without reducing T_s decreases the value of $\mathcal{R}$, while an increase of the number of LEDs / photodiodes increases the rate. So, the achievement of high rate values is due to both the possibility of having several LEDs / photodiodes, that can be installed also in small rooms, and the LED ability to quickly operate the electrical-to-optical conversion, this latter related to the modulation bandwidth of LEDs.

The expression given in (5.4) does not take into account the estimation of the channel. Without explaining here the rational leading to estimate the channel, we can anticipate that the transmission is *frame-oriented* with a frame length of N slots. Each frame is comprised of a number of N_e slots (with $N_e << N$), dedicated to channel estimation, while N_d slots (*i.e.*, $N_d = N - N_e$) are used for data transmission.

Notice that, starting from the value of T_s, we can argue that the need for a new channel estimation is due when the channel changes, and this happens after a time $T_{channel}$ [s]. This value can be of the order of seconds since it depends on two main aspects. The first one is represented by the changes of propagation environment due to modifications in the room (*e.g.*, people walking, tables and reflective objects close to transmitter or receiver), while the second aspect is the user mobility. For the latter aspect, a sensor able to measure the receiver movement can be taken into account so to proceed with channel estimation when something changes. A conservative way of setting the time to wait for a new estimation is essentially due to the speed of a (pedestrian) user; so half a second can be a reasonable value. The value of N is given by $N = \lfloor T_{channel}/LT_s \rfloor$.

The information-based transmission rate *i.e.*, the rate of the data transmission by considering that some symbols are used for channel estimation, can be written as

$$\mathcal{R}_{(N_d,N_e)} = \frac{N_d}{(N_d+N_e)L \cdot T_s} \log_2(L^{n_T}). \tag{5.5}$$

In the general case of n_T transmitting LEDs and L-PPM modulation, the maximum number of possible matrix codewords (when SMP is considered) is L^{n_T}, and the l-th matrix (with $l \leq L^{n_T} \in \mathbb{R}^+$) is given by

$$\mathbf{C}_l = \begin{bmatrix} c_{11}^{(l)} & c_{12}^{(l)} & \dots & c_{1j}^{(l)} & \cdots & c_{1n_T}^{(l)} \\ c_{21}^{(l)} & c_{22}^{(l)} & \dots & c_{2j}^{(l)} & \cdots & c_{2n_T}^{(l)} \\ \vdots & \vdots & \vdots & \vdots & \vdots & \vdots \\ c_{i1}^{(l)} & c_{i2}^{(l)} & \dots & c_{ij}^{(l)} & \cdots & c_{in_T}^{(l)} \\ \vdots & \vdots & \vdots & \vdots & \vdots & \vdots \\ c_{L1}^{(l)} & c_{L2}^{(l)} & \dots & c_{Lj}^{(l)} & \cdots & c_{Ln_T}^{(l)} \end{bmatrix}, \tag{5.6}$$

which, in a more compact form, can be expressed as

$$\mathbf{C}_l = \left[\mathbf{c}_1^{(l)} \; \mathbf{c}_2^{(l)} \; \cdots \; \mathbf{c}_j^{(l)} \; \cdots \; \mathbf{c}_{n_T}^{(l)} \right], \tag{5.7}$$

being $\mathbf{c}_j^{(l)}$ the $[L \times 1]$ column vector representing the signal emitted by the j-th LED (related to the l-th codeword), under the following two constraints:

$$\sum_{i=1}^{L} c_{ij}^{(l)} = 1, \qquad \text{and} \qquad c_{ij}^{(l)} \in \{0,1\}, \tag{5.8}$$

thus meaning that each column vector must contain all zeros with the exception of a sole 1. The expression used for evaluating rate implicitly contains some performance parameters like L, n_T together with $N_d + N_e$ and

T_s. Since SMP allows high bit rate without taking care of error probability, in order to accomplish the task of achieving a minimum required rate, and guarantee a (required) maximum bit error probability for an assigned transmitting power, we must tackle with the following problem [2]:

$$\text{find a STBC,} \tag{5.9a}$$

$$\text{s.t.} \sum_{i=1}^{L} \sum_{j=1}^{n_T} c_{ij}^{(l)} c_{ij}^{(m)} = 0, \;\; l \neq m, \;\; l, m \in \mathfrak{M}, \;\; |\mathfrak{M}| = M, \tag{5.9b}$$

$$M \geq 2^{\frac{\mathcal{R}^\star L T_s (N_d + N_e)}{N_d}}, \tag{5.9c}$$

$$\sum_{i=1}^{L} c_{ij}^{(l)} = 1, \;\; \text{and} \;\; c_{ij}^{(l)} \in \{0, 1\}, \tag{5.9d}$$

$$\Pr\{e\} \leq \Pr\{e\}^\star. \tag{5.9e}$$

The first constraint is related to the choice of proposing codewords retaining the property of being trace orthogonal (see [101] for a non-orthogonal modulation case), that is, having

$$\text{Tr}\{\mathbf{C}_j^T \mathbf{C}_i\} = \begin{cases} 0 & j \neq i \\ n_T & j = i \end{cases} \tag{5.10}$$

The number of codewords must be at least M – the minimum value (from (14c)) required to achieve the minimum rate $\mathcal{R}^\star$. Moreover, M is the cardinality of $\mathfrak{M}$ that is the set containing all possible codewords retaining the property of being trace orthogonal. The constraints in (14d) are the same as reported in (5.8), while the last constraint (14e) is related to the error probability, whose expression will be detailed in Subsection 5.1.3, once introduced the receiver structure in Subsection 5.1.2.

The above problem is not feasible for each value of $\mathcal{R}^\star$ and $\Pr\{e\}^\star$ (and also optical transmission power). Moreover, without the constraint (14d), it is also possible to have multiple pairs (L, n_T) guaranteeing the minimum rate $\mathcal{R}^\star$, even if each pair can lead to different $\Pr\{e\}$.

Remark - On illumination issue

Before providing a simple example, let us remark here that we do not consider illumination in the above problem. The additional constraint should be on the received power at photodiodes expressed in lux (or equivalently in Watts). In this context it seems that PPM, exhibiting low Peak to Average Power Ratio (PAPR), can induce flickering and/or dimming. In this,

[2] To be solved *offline*, when the VLC system is provisioned and installed.

we must differentiate the light emitted by LEDs and the light perceived by human eye. By resorting to the second Bloch's law (see chapter 3 in reference [102]) stating that the human eye is unable to distinguish two light flashes as different if they are sufficiently close in time. With operating frequencies well exceeding 1KHz we can argue that the light received by the human eye will be perceived as continuous. Moreover, since we deal with MIMO-PPM, there is always one LED in an ON state, so this solves the illumination issue.

A quick and simple example is that obtained by assuming a $(L = 2)$-PPM, performed over $(n_T = 2)$ LEDs; the matrix dimension is then $[2 \times 2]$. The maximum allowed number of matrix is L^{n_T} and the codewords are listed below

$$\mathbf{C}_1 = \begin{bmatrix} 1 & 0 \\ 0 & 1 \end{bmatrix}, \mathbf{C}_2 = \begin{bmatrix} 0 & 1 \\ 1 & 0 \end{bmatrix},$$

$$\mathbf{C}_3 = \begin{bmatrix} 1 & 1 \\ 0 & 0 \end{bmatrix}, \mathbf{C}_4 = \begin{bmatrix} 0 & 0 \\ 1 & 1 \end{bmatrix}. \tag{5.11}$$

By using all the matrices it is possible to achieve SMP while selecting only matrices $\mathbf{C}_3$ and $\mathbf{C}_4$, and also it is possible to achieve an orthogonal space-time block coding (in fact we have $\mathbf{C}_3^T\mathbf{C}_4 = \mathbf{0}_{2\times2}$). Having Orthogonal STBC (OSTBC) means having TO-STBC. Using $\mathbf{C}_1$ and $\mathbf{C}_2$ allows having TO even if it does not guarantee OSTBC. This leads to use only 2 codewords, while the simultaneous use of 4 codewords allows achieving twice the data rate.

5.1.2 Receiver Architecture

Before introducing the receiver architecture, we analyze the properties retained by the space-time block codewords. As stated in the constraint (14.a), the codewords are trace-orthogonal. Usually this property is not guaranteed at the receiver since the rows and columns of the transmitted coderwords are mixed by the channel. As a consequence, the channel knowledge at the receiver is fundamental to perform a correct detection/decoding process.

It is reasonable to assume that some pilot pulses can be transmitted, allowing the receiver to acquire sufficient information about the propagation environment. The receiver is comprised of two different logical operations that are (*i*) the *channel estimation*, and (*ii*) the *data detection*, as depicted in Fig. 5.1.

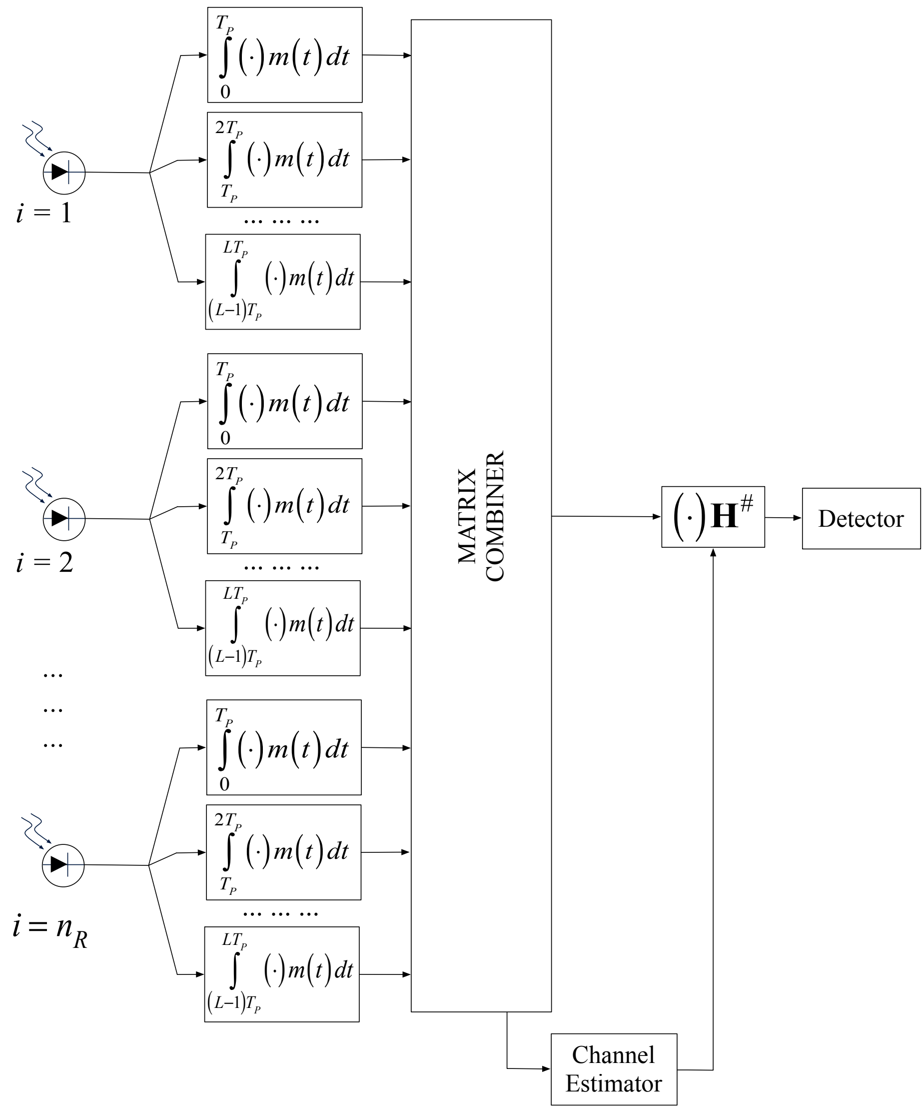

Fig. 5.1: Block scheme of the receiver architecture. The i inputs are the signals received by n_R photodiodes, with $i = \{1, 2, \cdots, n_R\}$, each one filtered by an integrator bank. The matrix combiner collects all the filter outputs representing the estimated channel paths. The matrix (pseudo)-inversion operation is adopted for data detection.

Channel estimation

The channel estimation task requires special training sequences. By considering the channel representation in (5.1), it appears evident that for a matrix $\mathbf{C}$ equal to identity (*i.e.*, when $L = n_T$), the received matrix $\mathbf{Y}$ equates $(\mathbf{H}+\mathbf{W})$, thus meaning that in the estimation procedure the only source of error is noise. This implicitly means that a number of L symbols (with L equals to n_T) is needed for the estimation procedure.

Let us observe the receiver architecture depicted in Fig. 5.1. At the i-th photodiode, the i-th signal is filtered by an integrator bank, in order to compare it with $m(t)$ that is the receiver mask (in this case, set equal to $x(t)$, so as to implement the matched filter). Moreover, each integrator is time-shifted, so that it can capture the energy on different L-PPM symbols/intervals; this is operated by each branch corresponding to each photodiode.

The matrix combiner collects all the filter outputs that represent the estimated channel paths. This simple estimation requires only $n_T \cdot T_s$ seconds,[3] under the simplifying assumption of a flat (frequency) channel, which is reasonable in very short range applications. Otherwise, mechanisms such as presented in reference [21] can reduce the delay spread, confirming the importance of channel estimation. This kind of estimation can be also improved via the transmission of more extensive pilot symbols (corresponding to N_e), so as to gather more energy. One important issue is related to how frequently pilot symbols are required to be sent in order to acquire channel information. The pilot rate, that is the rate used for sending pilots, depends on channel coherence time. We can argue that changes incur over a time horizon of seconds since the channel changes due to (*i*) movements performed by the receiver (user) or (*ii*) reflecting objects in the room. So setting pilot rate of the order of half a second should be sufficient to have sufficiently fresh estimates. ■

Data detection

In the more general case of signal spread by the channel, the performance of the estimator is strongly affected by synchronization. Under the quite satisfied assumption of minimum phase channel [21], we are required to have synchronization and a sufficient guard time in order to avoid pulse overlap and also a good estimation of the main path. Minimum phase channels are characterized to have main paths in the first samples. In order to avoid temporal ISI, it suffices to introduce guard times. However, if the channel is not minimum phase and presents long delays and main components in the middle of channel impulse response, the guard times are not suitable, and other mechanisms (*e.g.*, cyclic prefix), should be used.

As stated before, the presence of the channel mixes the spatial components, and even in the absence of noise, the trace properties of the matrices are altered due to channel. This suggests to spatially *solve* the channel by

[3] This expression is due to the single receiver, which receives $Y = H$, in low noise condition. Thus, the channel is obtained by the output of each photodiode.

inverting it via a matrix inversion operation (in the case of squared matrix), or via the use of a pseudo-inverse matrix (used for rectangular matrix), as shown in Fig. 5.1. From a computational point of view, this operation is inexpensive because it can be implemented through a shift register storing data and a simple algorithm (e.g., QR or Singular Value Decomposition) to operate the pseudo-inversion before a matrix product.

After the optical-to-electrical conversion operated by the photodiode, the received matrix $\mathbf{Y}$ should be processed in order to obtain a decision variable (*i.e.*, $\mathbf{Z}$) defined as follows

$$\mathbf{Z} = \mathbf{Y}\mathbf{H}^{\sharp} = \mathbf{X} + \mathbf{W}\mathbf{H}^{\sharp}, \tag{5.12}$$

where the symbol $^{\sharp}$ means (*i*) inversion or (*ii*) pseudo-inversion operation, depending on the matrix dimension *i.e.*, (*i*) squared or (*ii*) rectangular, respectively. This is a spatial Zero Forcing procedure (ZF).

Once obtained the decision variable $\mathbf{Z}$, the decided codeword will be

$$\hat{\mathbf{C}} = \arg\max_{i} \mathrm{Tr}\{\mathbf{C}_i^T \mathbf{Z}\}. \tag{5.13}$$

This decision mechanism directly comes from reference 5.12. When the space-filtered noise $\mathbf{W}\mathbf{H}^{\sharp}$ in (5.12) is negligible, $\mathbf{Z}$ approaches $\mathbf{X}$, and since the matrices are trace orthogonal we can recognize the transmitted codeword. Finally, the detection mechanism is applied to N_d consecutive matrix codewords. Notice that the following three steps: *i)* matrix inversion, *ii)* the product of the received matrix by the pseudo-inverse, and *iii)* data detection are quite simple to implement and not costly from a computational standpoint since L and n_T, n_R are limited to be in the range $[2, 16]$ for L, and $[1, 16]$ for n_T and/or n_R.

One important aspect is related to possible rank deficient property of the channel matrix. It is worthwhile noting that the channel estimation is affected by noise. So, even though the matrix rank is deficient (due to correlation among channels), the effect of noise affects the spatial correlation that is lost. This meanse we have a performance loss due to imperfect channel estimation, even if pseudoinversion can be still performed.

5.1.3 Performance evaluation

Starting from the orthogonality exhibited in the trace sense, it is possible to evaluate the performance in terms of bit error probability that leads to solve possible ambiguities in determining the n_T and M values needed for meeting constraints. The bit error probability $\Pr\{e\}$ can be upper-bounded by the so called Union-Bound as follows[4]:

$$\Pr\{e\} \leq \int_{\mathbf{H}} \sum_{i=1}^{M} \sum_{j=1, j\neq i}^{M} \Pr\{\hat{\mathbf{X}} = \mathbf{C}_j | \mathbf{C}_i, \mathbf{H}\} \Pr\{\mathbf{H}\}. \tag{5.14}$$

The role played by the channel is conditioning. It is reasonable that different statistical modeling *LOS*, *ND-LOS*, and *NLOS* lead to different $\Pr\{e\}$. Moreover, the inequality holds for the conditioned probability, and since the average on channel statistics is performed at right and left side (with the same weight that is channel probability density function) this holds also the unconditioned error probability. The upper bound for the term $\Pr\{\hat{\mathbf{X}} = \mathbf{C}_j | \mathbf{C}_i, \mathbf{H}\}$ can be evaluated starting from the detection criterion in (5.13), so the transmitted codeword $\mathbf{C}_i$ is –wrongly– decoded as $\mathbf{C}_j$ with the following pairwise upper bound on probability:

$$\Pr\{\hat{\mathbf{X}} = \mathbf{C}_j | \mathbf{C}_i, \mathbf{H}\} \leq \Pr\{\mathrm{Tr}\{\mathbf{C}_j^T \mathbf{Z}\} > \mathrm{Tr}\{\mathbf{C}_i^T \mathbf{Z}\}\}, \tag{5.15}$$

that can be rewritten as:

$$\begin{gathered} \Pr\{\hat{\mathbf{X}} = \mathbf{C}_j | \mathbf{C}_i, \mathbf{H}\} \leq \\ \Pr\{\mathrm{Tr}\{\mathbf{C}_j^T \mathbf{C}_i + \mathbf{C}_j^T \mathbf{W} \mathbf{H}^\sharp\} > \mathrm{Tr}\{\mathbf{C}_i^T \mathbf{C}_i + \mathbf{C}_i^T \mathbf{W} \mathbf{H}^\sharp\}\}, \end{gathered} \tag{5.16}$$

where we replaced $\mathbf{Z} = \mathbf{C}_i + \mathbf{W}\mathbf{H}^\sharp$.

Once noted that $\mathrm{Tr}\{\mathbf{A} + \mathbf{B}\} = \mathrm{Tr}\{\mathbf{A}\} + \mathrm{Tr}\{\mathbf{B}\}$, $\mathrm{Tr}\{\mathbf{C}_j^T \mathbf{C}_i\} = 0$, and $\mathrm{Tr}\{\mathbf{C}_i^T \mathbf{C}_i\} = n_T$, we can rewrite the probability in (5.16) as follows

$$\begin{gathered} \Pr\{\hat{\mathbf{X}} = \mathbf{C}_j | \mathbf{C}_i, \mathbf{H}\} \leq \\ \Pr\{\mathrm{Tr}\{\mathbf{C}_j^T \mathbf{W} \mathbf{H}^\sharp\} > n_T + \mathrm{Tr}\{\mathbf{C}_i^T \mathbf{W} \mathbf{H}^\sharp\}\}\}. \end{gathered} \tag{5.17}$$

This last can be evaluated by resorting to a multivariate Gaussian distribution. Even if the nature of noise is different (Gaussian and Poisson), under the hypothesis of several light sources / reflections, the central limit theorem allows assuming the white noise as Gaussian. Then, by considering the linear combination induced among the noise samples by $\mathbf{C}_j$, $\mathbf{C}_i$, and $\mathbf{H}^\sharp$ –still providing a Gaussian random variable–, and also starting from a spatially white correlation for $\mathbf{W}$, once vectorized it through the $vec(.)$

[4]We indicate with $\hat{\mathbf{X}}$ the detected codeword according to (5.13). So, we implicitly state that $\hat{\mathbf{X}} \equiv \hat{\mathbf{C}}$ even if, for sake of readability, we prefer here, to use the symbolic representation of the detected codeword $\hat{\mathbf{X}}$ related to the transmitted codeword $\mathbf{X}$.

operator, the new linearly combined noise variable $\mathfrak{n}$ should be higher[5] than n_T, *i.e.*

$$\Pr\{\hat{\mathbf{X}} = \mathbf{C}_j | \mathbf{C}_i, \mathbf{H}\} \ \leq \ \Pr\{\mathfrak{n} > n_T\}. \tag{5.18}$$

The Union Bound cannot be expressed in closed form since it depends on channel statistics. As anticipated, this implicitly suggests that the problem described in (5.9) should be tackled off-line during system planning and setup. Once the channel statistics are known (and this depends on several parameters and propagation scenarios), it is possible to determine the L, n_T and n_R combination for meeting the constraints on $\mathcal{R}^\star$, and $\Pr\{e\}^\star$. There is no algorithm to solve this but it should be simply computed for exhaustive search. This may appear costly, however since we are working with small numbers $L = 2, 4, 8, 16$, and the maximum rate is upper-bounded by SMP, giving indication of the feasibility of the system, we can conclude that this can be implemented with MATLAB calculus tools in few seconds. Other approaches as binary programming can be pursued to speed up the solution searching. As a conclusive remark about computational costs, we can argue that this is an off-line project tool for TO-SBTC, thus time saving is not an issue.

5.2 Numerical Results

The simulations have been developed under the parameter assumptions collected in Table 4.1 if not differently specified, both under the optimistic assumption of *perfect* channel knowledge at the receiver, and *imperfect* channel state information (at the receiver) due to estimation errors. The BER simulations are obtained via Monte-Carlo method. The channel model between each LED and photodiode has been obtained through the CandLES simulator [42]. In the simulations we assumed that the PPM time shift Δ equates $T_s = 12.98 \cdot 10^{-9}$ s. Also, the numerical results are averaged over the spatial area described by the assumptions reported in Table 4.1.

In the simulations, the SNR is referred both to optical and thermal noise in order to evaluate a worst case scenario. In particular, the overall noise is

[5] As an example, let us consider the code represented by matrices $\mathbf{C}_3$ and $\mathbf{C}_4$, then (5.18) becomes

$$\begin{aligned}&\Pr\{\hat{\mathbf{X}} = \mathbf{C}_4 | \mathbf{C}_3, \mathbf{H}\} = \\ &= \Pr\{(w_{21} - w_{11})(h^\sharp_{11} + h^\sharp_{12}) - (w_{22} - w_{12})(h^\sharp_{21} + h^\sharp_{22}) > n_T\}.\end{aligned}$$

given by

$$\mathcal{N} = 2q(I_p + I_d)\Delta f + 4k_pTF\Delta f/R_f, \tag{5.19}$$

where I_p [A] is the average current, I_d [A] the dark current, Δf [Hz] the detector bandwidth, q electron charge, k_p [JK^{-1}] Boltzmann constant, T [K] the temperature, F noise factor, and R_f [Ω] amplifier feedback resistance. From (5.19), it follows that

$$SNR = \frac{(RP_r^{(opt)})^2}{2q(I_p + I_d)\Delta f + 4k_pTF\Delta f/R_f}, \tag{5.20}$$

that represents a worst case since optical and thermal noise components are simultaneously considered. Here R is the photodiode responsivity and $P_r^{(opt)}$ is the received optical power.

The tri-dimensional plot in Fig. 5.2 shows the simultaneous effect on achievable rate of the number L of PPM symbols and of the number n_T of LEDs, according to (5.4). The two surfaces are related to the SMP scenario, that is an upper bound for rate, and the transmission rate obtained by using TO-STBC. >From a feasibility point of view, the TO-STBC rate indicates the maximum achievable transmission rate under the constraint on the codewords to maintain the TO property. This implicitly means that a rate over-bounding the STBC rate, for an assigned value of L and n_T, cannot retain the TO properties so its BER is higher with respect to the one obtained with TO.

By increasing L from 2 to 16, the value of $\mathcal{R}$ related to SMP decreases from 38.5 Mbit/s to 19 Mbit/s, when only 1 LED-photodiode pair is considered, while for 8 LED-photodiode pairs, the achievable rate falls from 308 Mbit/s to 154.5 Mbit/s (with *blue* filter). This suggests that increasing the order of L-PPM modulation is not worth, while increasing the number of LEDs / photodiodes allows achieving very high rates. The limitation given by the L-PPM order may be fixed by adapting the T_s value to make the product $(L \cdot T_s)$ in (5.4) constant. In order to do so, a technological issue should be tackled since, as previously anticipated, this is strictly tied to the ability of LEDs to quickly perform the electrical-to-optical conversion. Regarding the STBC rate, its behavior with one LED is the same of SMP, while for $L = 16$ the maximum rate is around 150 Mbit/s.

Fig. 5.3 depicts the BER obtained for different values of L, and n_T, n_R in a *NLOS* scenario. Notice how while passing from $(L = n_T = n_R = 2)$ (with a rate of 38 Mbit/s) to $(L = 4, n_T = n_R = 2)$ (same rate), the BER decreases with the same slope since only a *coding gain*, in SNR sense, is obtained. The gain offered by the $(L = n_T = n_R = 4)$ configuration, with a rate of 156 Mbit/s, quickly achieves 10^{-9} at an SNR less than 14 dB, even if

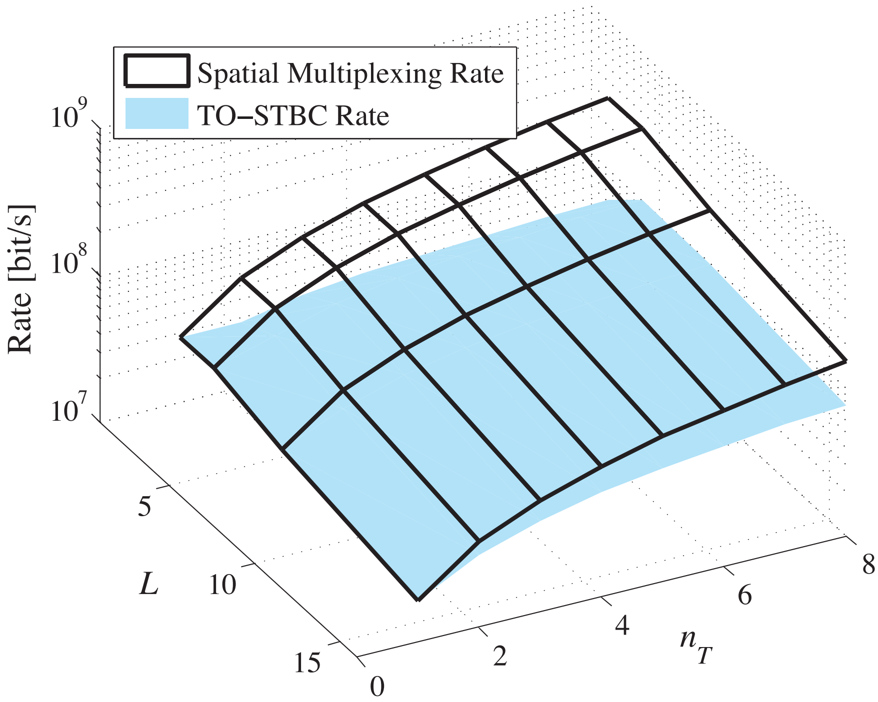

Fig. 5.2: Achievable rates for different values of L and n_T, when SM and STBC are considered.

this configuration requires 2 more LEDs and 2 more photodiodes, w.r.t. the previous two configurations. The above gain can be observed also in terms of diversity. In fact the slope of $n_T = 4, n_R = 4$ and $L = 4$ case is higher since we are increasing the dimension of the MIMO system so leading to higher diversity gain). All the above results are obtained in line with the problem in (5.9) by asking for matrices to be TO.

Furthermore, due to the important role of channel knowledge, we evaluated the channel robustness, as compared to an *imperfect* channel knowledge for statistically modeled channels. Even if the channel is slowly time-variant, when the relative positions between LEDs and photodiodes change, and new reflections are present, the propagation scenario is different. So, a sporadic pilot signaling is needed via pilots for channel knowledge acquisition. Under the hypothesis of having a data link layer able to operate error detection, the new estimation may be performed once an error has been detected. Alternatively, this can also be operated in real devices via accelerometer sensors, able to detect receiver movements.

In Fig. 5.4, increasing values of σ_h^2 refers to a imperfect channel state information detection; in practical scenarios, this may be due to users

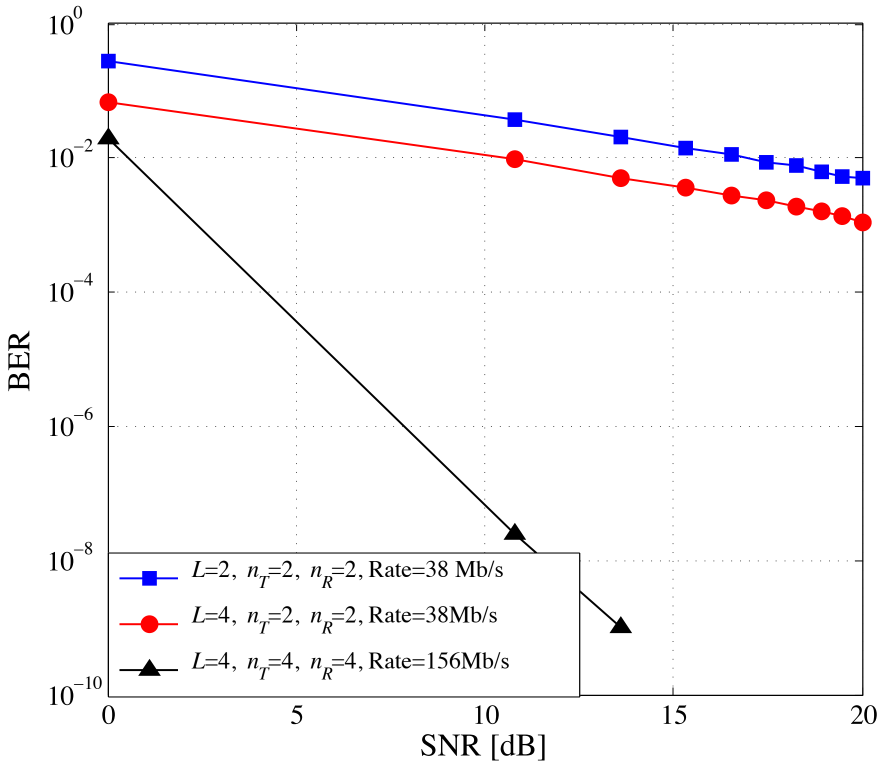

Fig. 5.3: BER vs. SNR for MIMO-PPM with different values of L, n_T and n_R in NLOS scenario.

moving in the room (*i.e.*, interferers), photodiode moved or external light sources added to the LED signal at the photodiode (*i.e.*, ambient noise).

The channel model is obtained through the use of CandLES simulator, and the comparison with Maximum Likelihood (ML) and Minimum Mean Square Error (MMSE) has been reported. We considered the term σ_h^2 related to the amplitude of channel $h(t)$, formally defined as

$$\sigma_h^2 = 1 - \frac{\int_T |\hat{h}(t)|^2 dt}{\int_T |h(t)|^2 dt}, \tag{5.21}$$

being $\hat{h}(t)$ the estimation of the channel.

Under the assumption that the channel is perfectly known at the receiver, the performance in terms of BER are the same and the curves are very closed to the following ranking: ML better than MMSE, and MMSE better than ZF. When the knowledge is corrupted by errors *i.e.*, $\sigma_h^2 = 0.2$, the BER increases, and also the performance hierarchy changes. ZF operated on $\mathbf{Z}$ is better than MMSE and ML, because ZF results to be less sensible to channel

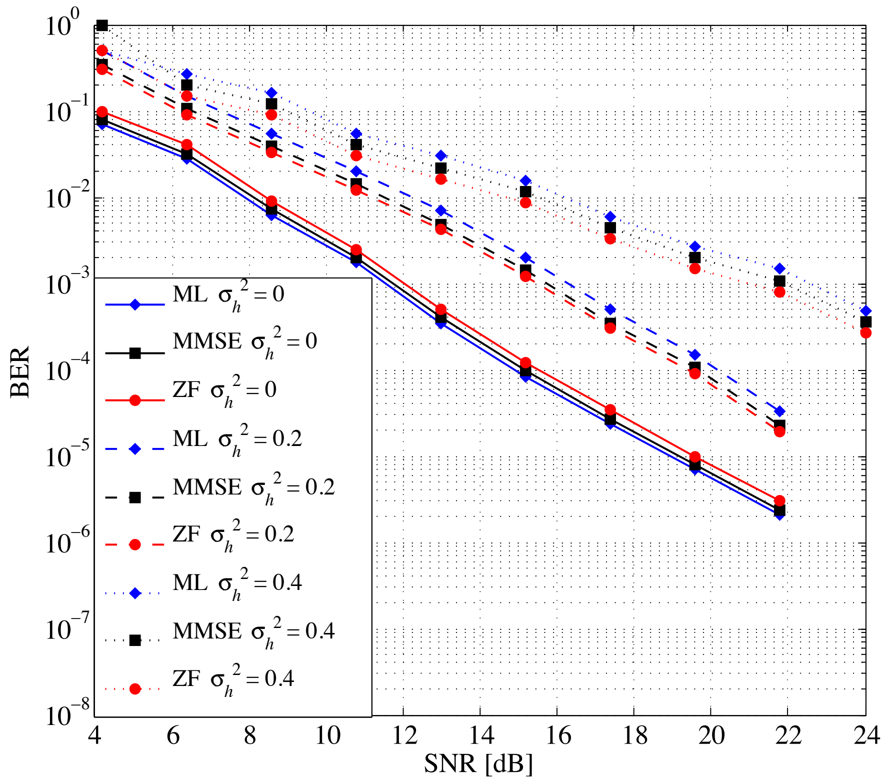

Fig. 5.4: BER vs. SNR for MIMO-PPM with different level of estimation errors, in the case of $[2 \times 2]$ system with 2-PPM.

estimation errors, thanks to trace operator w.r.t. the effect induced on the other approaches. The same behavior is experienced when $\sigma_h^2 = 0.4$, even if the BER values are higher (around 10^{-3} at $SNR = 18$ dB), while the perfect channel knowledge assures BER values below 10^{-6}, for the same SNR.

In order to validate the proposed technique w.r.t. other existing contributions, we provide a performance comparison, and considered the schemes proposed by Ntogari *et al.* in [8], Popoola *et al.* in [9], Abou-Rjeily in [10] since they represent recent works that are the best candidates for comparison purpose. The results are obtained assuming:

1. 4 LEDs and 1 photodiode with 4-PPM, for the solution in [9] since in this shape that scheme has been developed,

2. 2 LEDs and 2 photodiode, for the Alamouti code presented in [8] since the Alamouti-like scheme has been proposed for 2×1 and 2×2 systems,

3. 4 LEDs and 1 photodiode with a 4-PPM, for the one proposed by

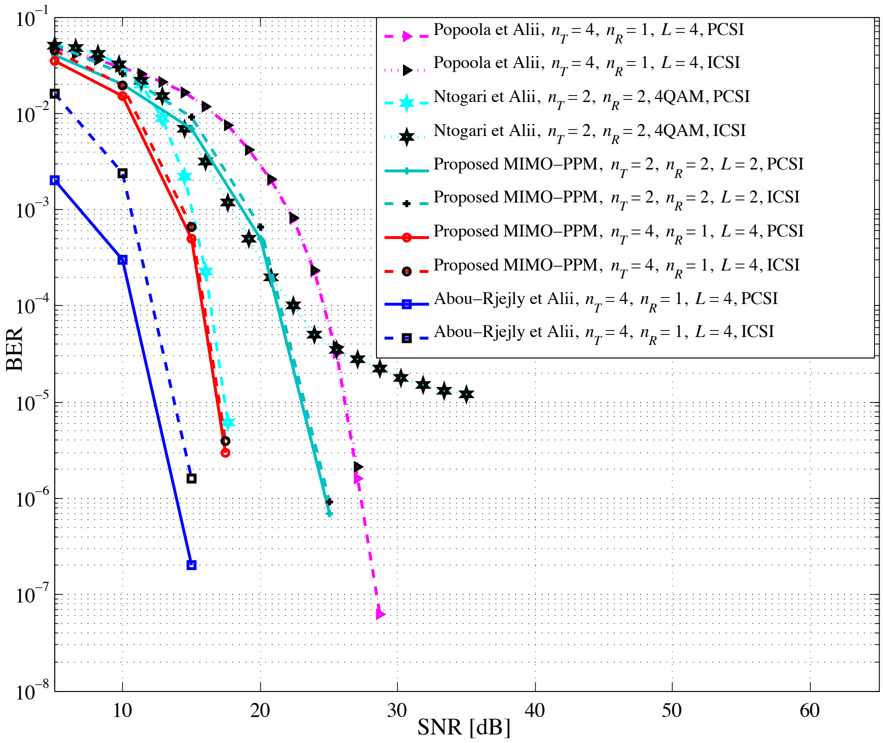

Fig. 5.5: BER vs. SNR for different approaches, in room center scenario. The proposed scheme MIMO-PPM is compared to the works by Ntogari *et al.* [8], Popoola *et al.* [9] and Abou-Rjeily *et al.* in [10].

Abou-Rjeily in [10],

4. 4 LEDs and 1 photodiode with 4-PPM, and 2 LEDs and 2, 2-PPM of the proposed TO-STBC for a fair comparison.

The simulation scenario is the same as depicted in [9], *i.e.*, the position of the user is evaluated (*i*) "under" and (*ii*) "far away" the LED, corresponding respectively to the *room center*, and the *room corner*. We have tested the various techniques in two different propagation scenarios, respectively under the assumptions of *perfect* ($\sigma_h^2 = 0$) and *imperfect* ($\sigma_h^2 = 0.15$) channel knowledge. For comparison purpose, we assumed for the three techniques common room configuration parameters, as shown in Table 4.1.

Consider Fig. 5.5 and the behavior of the receiver in the *center* of the room. The Abou-Rjeily *et alii* approach outperforms the others because at low SNR it achieves very low BER.
In the case of Imperfect Channel State Information (ICSI) the performance is, as expected, not as satisfactory. For both the n_T, n_R, L configurations

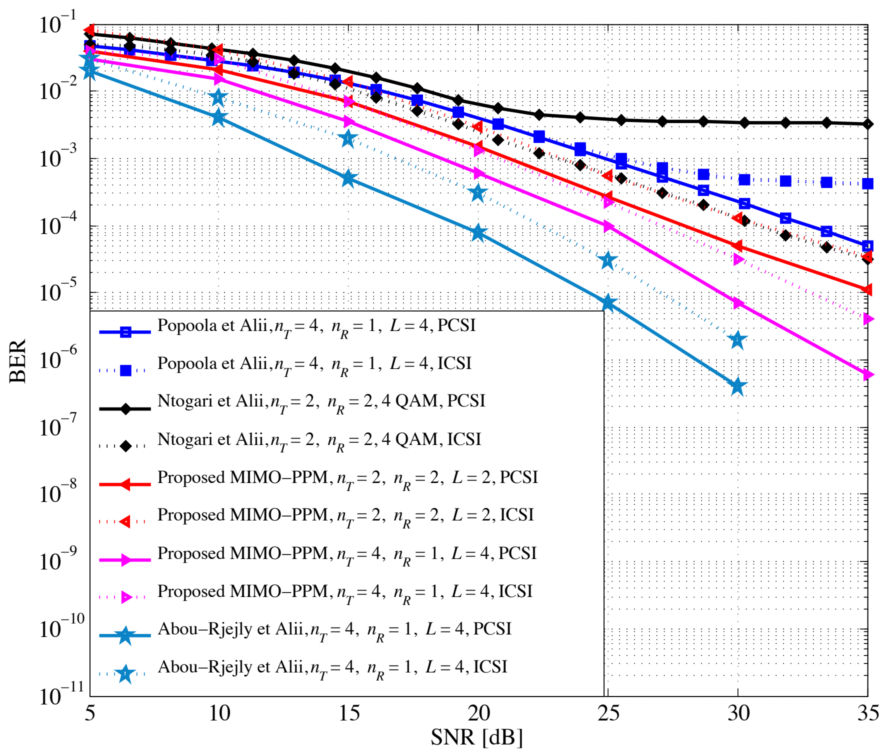

Fig. 5.6: BER vs. SNR for different approaches, in room corner scenario. The proposed scheme MIMO-PPM is compared to the works by Ntogari *et al.* [8], Popoola *et al.* [9] and Abou-Rjeily *et al.* in [10].

described before, our proposed scheme is able to perform better w.r.t. the ones of Popoola's and Ntogari's one, while it fails w.r.t. [10]. The gap is 5 dB. Not surprisingly, all the systems compared here under the ICSI case show worse performance compared to Perfect Channel State Information (PCSI). A particular note should be given for the Ntogari's (Alamouti-like) scheme that presents an error floor when ICSI is considered.

A different behavior occurs when the receiver is far from the LEDs (*i.e.*, in the room *center*) as reported in Fig. 5.6. The SNR values achieving low BERs are higher w.r.t. the previous case. Also in this case, the scheme proposed in reference [10] has the best performance; our TO-STBC differs by approximatively 5 dB. On the other hand, the TO-STBC performs better w.r.t. the schemes proposed in [8] by Ntogari *et al.*, and Poopola *et al.*

When performance is evaluated in the cornervposition with ICSI, BER increases in all schemes.

The above comparison is perhaps not entirely fair because each system uses different assumptions about achievable transmission rates. In the

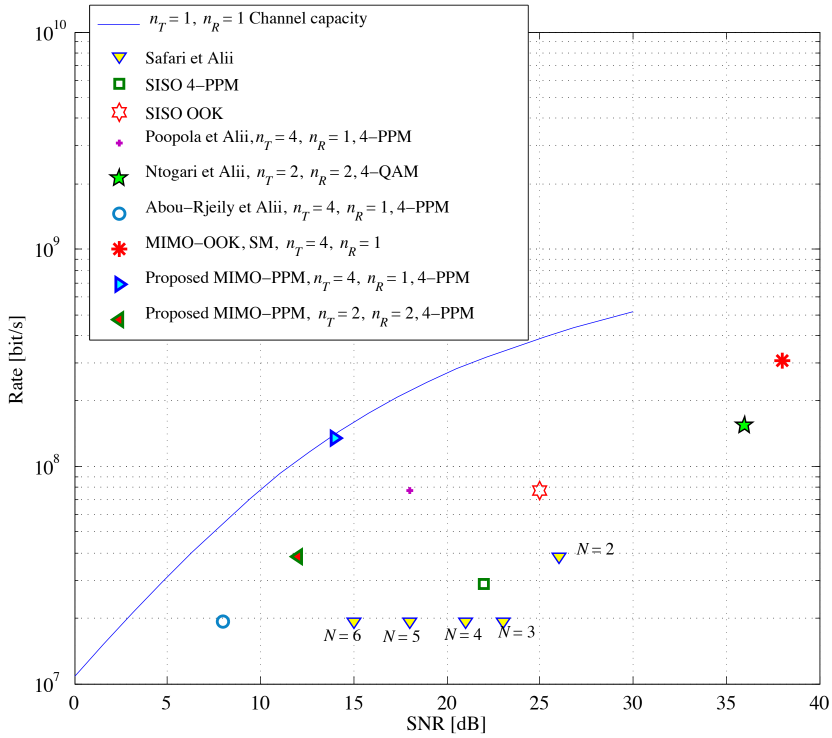

Fig. 5.7: Rate vs. SNR at BER 10^{-5} for different schemes with respect to traditional SISO channel Shannon capacity.

performed simulations, all the considered systems are compared under the assumption of the same pulse duration, and the same power transmission level. An interesting way of showing the possibilities offered by the above cited systems is reported in Fig. 5.7, where for a BER of 10^{-5}, the SNR needed and the transmission rate $\mathcal{R}$ are reported and compared to the Shannon capacity curves for the simple case $n_T = n_R = 1$. Note that the Shannon curve does not consider the features typical of the optical link (no negative signals and Gaussian and Poisson disturbance), so in this sense it is a bit optimistic since, due to a bias optical signal, the power to be spent must be higher so it is an upper bound.

Safari *et al.* [95] is able to achieve the target BER with a very low SNR; however, at the expense of reducing transmission rate of the PAM-based modulation due to the repetition coding used (N in the plot indicates the number of repetitions of the same symbol). On the other hand, the target BER the scheme proposed by Poopola *et al.* [9] achieves a very good transmission rate (*i.e.*, 77 Mbit/s), at the expense of transmission power. This is not a heavy drawback if we resort to a downlink scheme, although it strongly increases the negative effect if an uplink is considered. A modestly higher performance, expressed in terms of rate, is achieved by Ntogari *et al.* [8] under the assumption of 4-QAM even if it requires perfect channel knowledge and high transmission power. They achieve 150 Mbit/s. The MIMO-OOK (independent OOK transmission of 4 different LEDs as SM) performs well in terms of rate (300 Mbit/s), while fails on power efficiency. SISO-OOK is under MIMO-OOK in terms of rate even if it requires less power to achieve the target BER. SISO 4-PPM is a bit worse w.r.t. SISO OOK due to the spectral inefficiency of PPM while it gains in terms of SNR.

Regarding the contribution in reference [10] that exhibits the best considered BER, it clearly is in the left part of the plot because low SNR is required for the target BER. Since that scheme presents matrices of dimensions $Ln_T \times n_T$, this reduces its rate because $Ln_T T_s$ are needed to transmit a codeword. Finally, the proposed TO-STBC performs well for the $n_T = 4, n_R = 1$, 4-PPM because it is at the same level of MIMO-OOK with a considerable gain in terms of power. It has half of the rate of Ntogari's approach but with less power, more robustness w.r.t. channel knowledge, and has simplicity of realization. The $n_T = 2, n_R = 2, 2$-PPM scheme is in-between w.r.t. $n_T = 4$, $n_R = 1$, 4-PPM performances of the proposed scheme, and the one of reference [94].

Chapter 6

Camera as Receiver

VLC systems can be divided into two groups, the first is formed by photodiode-based communication systems, while the second by image sensors, like optical cameras, as receivers. A camera sensor is essentially a very dense two-dimensional array of photodiodes, where each photodiode represents a single pixel. The VLC subgroup that uses cameras is often called Optical Camera Communication (OCC) system. In [44], instead, VLC have been grouped into two categories, the systems able to achieve very high data rate and those reaching only low data rate. If the high data rate ones requires specialized high-speed photodiode receivers, whereas the low data rate can be realized using existing hardware available in mobile devices. OCC belongs to this latter systems. The low data rate issue of OCC is due to the low frame rate of available camera in the market, for instance, the typical frame rate of smarthpones is 30 frame/s, or, at best, few models can reach an acquisition of 120 frame/s.

There has been a growing interest in OCC, since cost effective, because can take advantage of the already available hardware present on a broad range of electronics devices like smartphones, tablets and laptops. For this reason the IEEE 802.15.7 task group is now focusing its attention also on OCC.

Instead of using LEDs lighting as transmitters, in this systems can be also used display screens, which in modern devices are composed of Organic LEDs (OLED), in order to create image patterns to convey information. The patterns produced can be detected from the images acquired by the camera, because even lights coming from slightly different directions can be separated and projected over distant pixels.

OCC can enable unique mobile wireless device use cases, such as localization based services for indoor navigation or dedicated marketing information [103], Device-to-Device communications, augment reality or

Vehicle-to-Vehicle and Vehicle-to-Infrastructure communication [104].

The challenge is to improve the communication data rate, which, as said before, is limited by the camera slow frame rate. In order to overcame this issue, in [105] it is proposed to exploit the rolling shutter effect. In this way the receiver can detect row-by-row the intensity changes, so that the sampling rate is improved by a factor which is proportional to the number of rows of the camera and in this way higher transmitting frequency are supported.

In Fig. 6.1 a representation of a typical MIMO OCC is provided, due to the high spatial resolution of the camera, the light signal passing through the imaging lens is projected on different positions of the image sensor. In this way, the signals coming from multiple sources are spatially separated. So, because of the camera lens properties, another way to overcome the low frame rate issue consists in using optical MIMO techniques in order to increase considerably the data rate through spatial multiplexing. Regarding works in the literature dealing with MIMO OCC, in [106] the author introduces a simple protocol that acquaints the receiver about how to process the MIMO data stream. It is proposed, moreover, a novel modulation for OCC systems. Instead, in [107] and [108] the Multiple-Input transmitter is a display, symbols are represented by group of pixels and at the receiver, object detection techniques are used to decode symbols. The interested reader can find in [109] the performance analysis of these systems, where a display is used as transmitter.

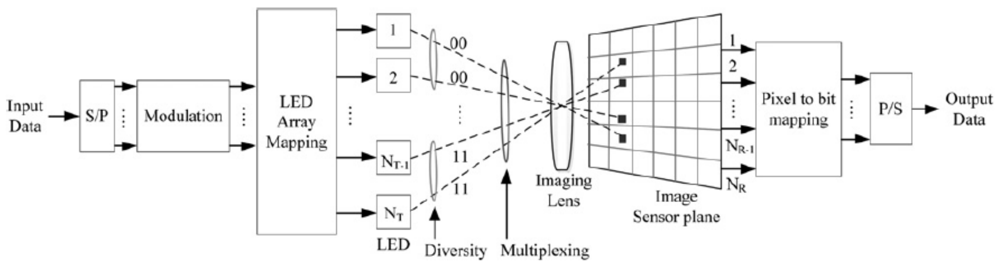

Fig. 6.1: Example of an OCC MIMO system [11].

Despite this, in Multiple Input OCC system, an important source of performance degradation is the spatial intersymbol interference that can occur both when the receiver is in mobility and when there is a long distance between the transmitter and the receiver; in those cases the received image is affected by blur. Optical channel blurring is a primary issue in OCC systems, but, so far, just a few works have tried to address this problem, expecially without *a priori* knowledge of the channel.

6.1 Spatial Fractionally Spaced Equalizer

In Spatial Fractional Sampling (SFS) systems, the spatial sampling interval is a fraction of the spatial symbol duration in pixels, thus, at receiver side, it is possible to take advantage of the information redundancy associated with the transmitted signal. By using image-based receiver, the degree of freedom for describing the transmitted symbols, i.e. the spatial resolution, can be very high, and this aspect is even more evident when the number of pixels composing the camera grows. For both LEDs-to-camera and display-to-camera transmission, due to the high spatial resolution at receiver side, symbol detection is based on the evaluation of a *group* of pixels instead of a single pixel. Then, it is possible to state that there is an intrinsic SFS of the signal where the number of pixels between consecutive symbols measures the fractional sampling factor. Therefore, in OCC systems, it is possible to exploit the potential of fractionally spaced equalizers [110]-[13] to counteract the blurring effect introduced by the optical propagation channel.

Having an higher spatial sampling rate leads to a received signal that is ciclostationary, which is a remarkable property that leads to carry out blind channel estimation using only second order statistics [111]. Under some conditions, even non-minimum phase channels are identifiable from the output data. Moreover, the equalizer for a Finite Impulse Response (FIR) channel is a FIR filter too [112].

In [113] and [114] the authors use a multichannel Spatial Fractionally Spaced Equalizer (SFSE) for blind blur estimation and blind image restoration. In [113] they show that if at least three images are available, it is possible to use the properties of single-input multiple-output image data in order to derive algorithms for blind image restoration when the multiple FIR channels are co-prime. Interestingly, in MIMO OCC systems several images are not needed to get a multichannel FIR, since in a single camera acquisition are present several *sub-images* that refers to the symbols transmitted.

To find the equalizer, it is possible to either estimate the channel first and then calculate the equalizer or directly estimate the equalizer [115]. This latter case is computationally more efficient and attractive for recursive implementations, in fact, here a spatial semi-blind equalization scheme based on a novel Recursive Least-Squares (RLS) algorithm is presented.

The presented adaptive OCC SFSE has also a filter coefficients updating procedure based on Minimum Mean Square Error (MMSE) nonlinear symbol estimation, and a semiblind approach it is investigated to drive the convergence of the RLS algorithm based on the cornice of known (active) symbols needed for image detection and alignment.

The RLS algorithm is used for OCC SFS equalization, addressing an issue of primary importance in the field, *i.e.*, the spatial interference occurring in MIMO OCC. It is proposed a way to suppress the intersymbol interference without a priori knowledge of the optical channel taking advantages of the high number of receiver elements (pixels) at the receiver side, exploiting the intrinsic fractionally sampling nature of the camera.

6.1.1 System Model

In this section it is introduced the model of the optical communication link (Fig. 6.2), where s_n are the transmitted real valued symbols of an M-ary, equiprobable, constellation. The On-Off Keying (OOK) is considered, it is extensively used in VLC [116], [34] mainly because it is a simple modulation. In the generic frame t, $N = N_1 \times N_2$ spatial symbols $s^{(t)}[n_1, n_2]$ are simultaneously transmitted, with $n_1 = 0, ..., N_1 - 1$, $n_2 = 0, ..., N_2 - 1$ representing the discrete spatial coordinates. Denoting the continuous spatial coordinates by z_1 and z_2, and defining the transmitter shaping filter impulse response as $g_{\mathrm{T}}(z_1, z_2)$, the analog spatial transmitted signal in the t-th frame is written:

$$b_a^{(t)}(z_1, z_2)=\sum_{l_1=0}^{N_1-1}\sum_{l_2=0}^{N_2-1} s^{(t)}[l_1, l_2]\, g_{\mathrm{T}}(z_1-l_1D_1, z_2-l_2D_2) \tag{6.1}$$

where D_1 and D_2 are the distance between two consecutive transmitted symbols along the z_1 and z_2 spatial coordinates, respectively. After the transit through the optical propagation channel the transmitted signal is represented by $x_a^{(t)}(z_1, z_2) = (b_a^{(t)} * h)(z_1, z_2)$. Defining $g_a(z_1, z_2) = (h * g_{\mathrm{T}})(z_1, z_2)$ it is possible to write:

$$x_a^{(t)}(z_1, z_2)=\sum_{l_1=0}^{N_1-1}\sum_{l_2=0}^{N_2-1} s^{(t)}[l_1, l_2]\, g_a(z_1-l_1D_1, z_2-l_2D_2) \tag{6.2}$$

Hence at the receiver the signal becomes:

$$y_a^{(t)}(z_1, z_2) = x_a^{(t)}(z_1, z_2) + v_a^{(t)}(z_1, z_2) \tag{6.3}$$

where $v(z_1, z_2)$ is a realization of Additive White Gaussian Noise (AWGN), with mean value equal to zero, variance σ_v^2 and spatially statistically independent from the symbols.

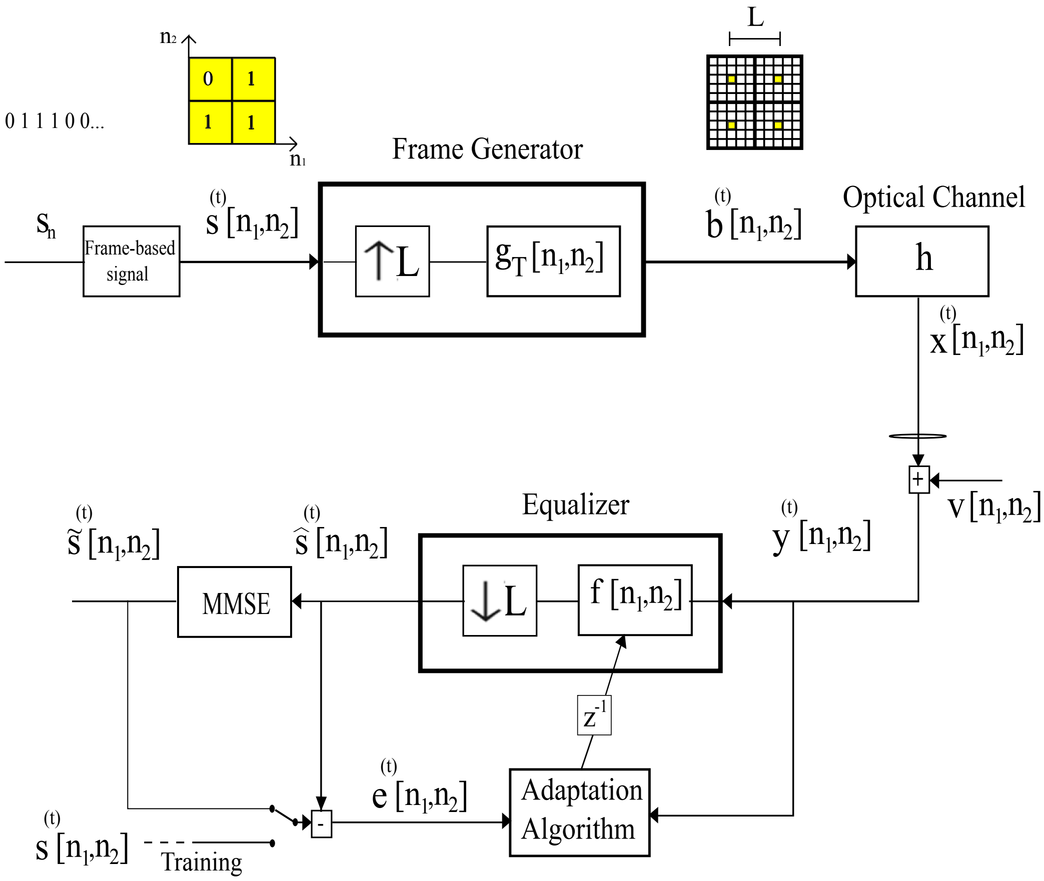

Fig. 6.2: Equivalent discrete space-time system block diagram.

Performing the spatial sampling at fractional rate L, the digital received signal is:

$$y^{(t)}[n_1, n_2] = y_a^{(t)}\left(n_1 \frac{D_1}{L_1}, n_2 \frac{D_2}{L_2}\right) \tag{6.4}$$

For simplicity it is considered $D = D_1 = D_2$ and $L = L_1 = L_2$. After the SFS, the overall impulse response can be written as $g[n_1, n_2] = g_a\left(n_1 D/L, n_2 D/L\right)$ and the matrix of pixels obtained at the receiver camera, with fractional factor L is:

$$\begin{aligned} y^{(t)}[n_1, n_2] &= x_a^{(t)}\left(n_1 \frac{D_1}{L_1}, n_2 \frac{D_2}{L_2}\right) + v_a^{(t)}\left(n_1 \frac{D_1}{L_1}, n_2 \frac{D_2}{L_2}\right) \\ &= \sum_{l_1=0}^{N_1-1} \sum_{l_2=0}^{N_2-1} s^{(t)}[l_1, l_2] g[n_1 - l_1 L, n_2 - l_2 L] + v^{(t)}[n_1, n_2] \end{aligned} \tag{6.5}$$

The parameter L depends on the number of pixels composing a camera frame and the number of symbols transmitted within one frame. In summary, L is equal to the row distance (measured in pixels) between two adjacent symbols in the received digital signal $y^{(t)}[n_1, n_2]$.

In the following, to simplify the notation, pair of indices n_1, n_2 will be indicated with a bidimensional index $\underline{n} \stackrel{\text{def}}{=} [n_1, n_2]$ and similarly for spatial radian frequencies ω_1, ω_2 indicated with $\underline{\omega} \stackrel{\text{def}}{=} [\omega_1, \omega_2]$; moreover, it is omitted the t apex when not strictly necessary, *i.e.* when a single frame is considered.

In order to write bidimensional convolutions and similars with only one summation thus simplifying the writing of subsequent analytical developments, let define $\mathcal{S}_f$ as the bidimensional finite set that collects the bidimensional indices where the SFSE coefficients $f[\underline{k}]$ are defined, so that the equalized signal is written:

$$\hat{s}[\underline{n}] = \sum_{\underline{k} \in \mathcal{S}_f} f[\underline{k}] \cdot y[\underline{n}L - \underline{k}] \tag{6.6}$$

In absence of noise, (6.6) perfectly recovers the symbols when the equalizer frequency response $F(e^{j\underline{\omega}}) = \sum_{\underline{k} \in \mathcal{S}_f} f[\underline{k}]\, e^{j\underline{\omega}^{\mathrm{T}}\underline{k}}$ satisfies the Nyquist Zero-Intersymbol Interference (ISI) criterion:

$$\frac{1}{L^2} \sum_{l_1=0}^{L-1} \sum_{l_2=0}^{L-1} F\left(e^{j\underline{\omega} + j\frac{2\pi}{L}\underline{l}}\right) \cdot G\left(e^{j\underline{\omega} + j\frac{2\pi}{L}\underline{l}}\right) = 1. \tag{6.7}$$

The spatial frequency response $G(e^{j\underline{\omega}}) = G_{\mathrm{T}}(e^{j\underline{\omega}}) \cdot H(e^{j\underline{\omega}})$ includes the transmitter filter and the optical channel and can have some zeros due to nulls of $H\left(e^{j\underline{\omega}}\right)$. It is important to notice that is not possible to have Zero-ISI when for a spatial radian frequency $\underline{\omega}$ it occurs $\sum_{l_1=0}^{L-1} \sum_{l_2=0}^{L-1} G\left(e^{(j\underline{\omega} + j2\pi\underline{l})/L}\right) = 0$.

Remark on support design - An important feature that can be exploited is the possibility to choose different shapes for the support $\mathcal{S}_f$, which in turn depends on the blur spatial occupation. As it will be shown later in the numerical results, this feature allows to select only the most useful pixels in the equalization filtering (6.6), thus reducing the computational complexity, and at the same time to discard pixels that can slow the convergence of the RLS algorithm. Moreover, also "sparse" supports can be enclosed within this notation as exemplified in Fig. 6.3.

It is also important to notice that removing ISI by simply meeting the Nyquist criterion (6.7) can lead the SFSE achieved by $f[\underline{n}]$ to excessively

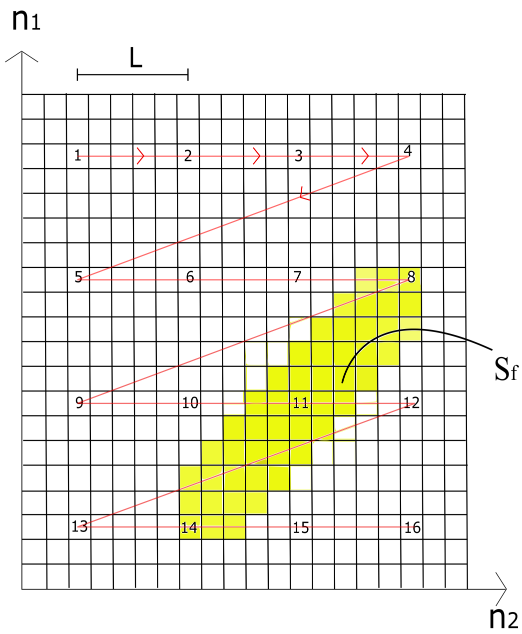

Fig. 6.3: Example of a received frame with 16 symbols and fractional factor L equal to 5. With the red arrow it is shown the lexicographic order followed by the RLS algorithm. In yellow it is represented a filter support for the case of the eleventh symbol.

amplify the noise $v[\underline{n}]$ for those spatial frequencies where the Signal-to-Noise Ratio (SNR) is really low. Therefore, the equalization filter synthesis $f[\underline{n}]$ must follow some appropriate optimality criterion.

6.1.2 MMSE SFSE

Due to the spatial fractional sampling, the received signal $y[\underline{n}]$ in (6.5) turns out to be spatially ciclostationary so that its autocorrelation is defined as $R_y[\underline{m}-\underline{k};-\underline{k} \bmod L]=\mathrm{E}\{y[\underline{n}L-\underline{k}]\,\overline{y}[\underline{n}L-\underline{m}]\}$, where the notation $-\underline{k} \bmod L$ indicates the periodicity modulo L induced by the spatial ciclostationarity.

On the other hand, the cross-correlation between $y[\underline{n}]$ and the spatially stationary symbols $s[\underline{n}]$ does not experience any periodicity and it is defined as $R_{sy}[\underline{m}]=\mathrm{E}\{s[\underline{n}]\,\overline{y}[\underline{n}L-\underline{m}]\}$.

The synthesis of the SFSE is conducted exploiting the MMSE criterion, which in this case leads to the following normal equations [114] :

$$\sum_{\underline{k}\in\mathcal{S}_f} f[\underline{k}]\, R_y[\underline{m}-\underline{k}; -\underline{k} \mod L] = R_{sy}[\underline{m}],\ \forall \underline{m} \in \mathcal{S}_f \tag{6.8}$$

It is worth noticing that (6.8) requires the knowledge of the cross-correlation function $R_{sy}[\underline{m}]$, computable when training symbols, also known at receiver, are transmitted. In *blind* techniques, *i.e.* no training symbols are available at receiver, $R_{sy}[\underline{m}]$ shall be suitable estimated as we will show in the following paragraphs.

Finally, for both blind and not blind techniques, to solve (6.8) one can resort to Least Mean Square (LMS) or RLS adaptive filtering techniques.

6.1.3 Blind Adaptive Algorithm: RLS

In the OCC case, the RLS adaptation shall be conducted along the bidimensional discrete space $[n_1, n_2]$ for each and every frame; on the other hand, all the frame pixels are simultaneously received at a certain frame rate. In this regard, the RLS adaptation must properly take into account the *space-time* nature of the received frames.

For each and every frame, the spatial RLS adaptation replaces the MMSE estimation criterion with a least-squares, weighted space/time-average that includes all estimation errors from the initial symbol to the current one along the lexicographic scan depicted in Fig. 6.3. While the LMS adaptation technique based on the steepest descent method provides a gradual, iterative, minimization of the least-squares criterion performance index, the RLS adaptation algorithm obtains the optimal filter coefficients at each iteration [117].

Regarding imaging applications, it is possible to find the conventional RLS algorithm [118] extended to the bidimensional case in [119] or in [120], where the authors apply a 1-D RLS algorithm along both horizontal and vertical directions. In [121] the authors transform the bidimensional problem in a multichannel one, where every row (or column) is considered as a channel.

Given the above considerations, the adaptive space-time RLS algorithm described in this chapter presents novelty characteristics compared to the conventional RLS one. In fact there is a separation between once-per-frame filtering and intra-frame filter coefficients updating. Specifically,the once-per-frame filtering is *postponed* at the end of the symbol lexicographic scanning thanks to a suitable formulation of the RLS error updating. Moreover, it is used a full exploitation of the SFS of the measured image in the design and the implementation of the equalizer, which is faced with a Nyquist condition simpler than full channel inversion required when sampling is operated at strictly Nyquist rate. The equalizer support choice is flexible, well suited to the blur shape.

Specifically, the RLS cost function is defined as follows:

$$\mathcal{E}^{(t)}[n] = \sum_{i=1}^{t} \sum_{\underline{j}=0}^{\underline{n}} \lambda^{(tN+\underline{n})-(iN+\underline{j})} |e^{(i)}[\underline{j}]|^2 \tag{6.9}$$

where λ is the forgetting factor and $e^{(t)}[\underline{j}] = s^{(t)}[\underline{j}] - \hat{s}^{(t)}[\underline{j}]$ is the error measured for the $\underline{j}$-th symbol of the t-th frame. To make the subsequent developments more readable, the quantity $\tau = (tN + \underline{n}) - (iN + j)$ is introduced and the filtering (6.6) is rewritten in a more compact notation as follows:

$$\hat{s}^{(t)}[\underline{n}] = [\mathbf{f}_{\underline{n}}^{(t)}]^{\mathrm{T}} \cdot \boldsymbol{\gamma}_{y,\underline{n}}^{(t)} \tag{6.10}$$

where $\mathbf{f}_{\underline{n}}^{(t)}$ collects the filter coefficients that obtain the $\underline{n}$ symbol estimate $\hat{s}^{(t)}[\underline{n}]$ of the t-th frame, and $\boldsymbol{\gamma}_{y,\underline{n}}^{(t)}$ collects the corresponding values of $y^{(t)}[\underline{n}]$, both collected on the support $\mathcal{S}_f$ according to (6.5).

With these positions, differentiating (6.9) with respect to $\mathbf{f}_{\underline{n}}$ yields the following least-square orthogonality conditions:

$$\frac{\partial \mathcal{E}^{(t)}[n]}{\partial \mathbf{f}_{\underline{n}}^{(t)}} = -2 \sum_{i=1}^{t} \sum_{\underline{j}=0}^{\underline{n}} \lambda^{\tau} \, e^{(i)}[\underline{j}] \, \boldsymbol{\gamma}_{y,j}^{(i)} = \mathbf{0} \tag{6.11}$$

The normal equations are obtained elaborating on (6.11):

$$\left[\sum_{i=1}^{t} \sum_{\underline{j}=0}^{\underline{n}} \lambda^{\tau} \boldsymbol{\gamma}_{y,j}^{(i)} \cdot [\boldsymbol{\gamma}_{y,j}^{(i)}]^{\mathrm{T}} \right] \cdot \mathbf{f}_{\underline{n}}^{(t)} = \sum_{i=1}^{t} \sum_{\underline{j}=0}^{\underline{n}} \lambda^{\tau} \, s^{(i)}[\underline{j}] \, \boldsymbol{\gamma}_{y,j}^{(i)} \tag{6.12}$$

Now defining the time/spatial-averaged correlation matrix:

$$\mathbf{R}_{y,\underline{n}}^{(t)} = \sum_{i=1}^{t} \sum_{\underline{j}=0}^{\underline{n}} \lambda^{\tau} \boldsymbol{\gamma}_{y,j}^{(i)} \cdot [\boldsymbol{\gamma}_{y,j}^{(i)}]^{\mathrm{T}} \tag{6.13}$$

Similarly, here is the definition of the cross-correlation vector:

$$\mathbf{r}_{sy,\underline{n}}^{(t)} = \sum_{i=1}^{t} \sum_{\underline{j}=0}^{\underline{n}} \lambda^{\tau} s^{(i)}[\underline{j}] \, \boldsymbol{\gamma}_{y,j}^{(i)} \tag{6.14}$$

Hence, the filter coefficients are computed as follows:

$$\mathbf{f}_{\underline{n}}^{(t)} = [\mathbf{R}_{y,\underline{n}}^{(t)}]^{-1} \cdot \mathbf{r}_{sy,\underline{n}}^{(t)} \tag{6.15}$$

For each and every t-th frame, according to the lexicographic symbol scanning indicated by $\underline{n}$, the correlation matrix estimate is spatially updated using the following rank one modification, suitably derived from the purely time based one [117]:

$$\mathbf{R}_{y,\underline{n}}^{(t)} = \lambda \mathbf{R}_{y,\underline{n}^{(p)}}^{(t)} + \mathbf{\Gamma}_{y,\underline{n}}^{(t)} \tag{6.16}$$

where $\mathbf{\Gamma}_{y,\underline{n}}^{(t)} = \boldsymbol{\gamma}_{y,\underline{n}}^{(t)} \cdot [\boldsymbol{\gamma}_{y,\underline{n}}^{(t)}]^{\mathrm{T}}$, and $\underline{n}$ indicates the current symbol and $\underline{n}^{(p)}$ the last visited one, see also Fig. 6.3 where the lexicographic symbol scanning is illustrated.[1]

Now are described the various steps of the classical RLS algorithm, revised for spatial fractionally spaced filtering and space-time updates. It is worth noting that RLS adaptation does not require any matrix inversion as it directly updates the inverse covariance matrix $\mathbf{P}$.

Now it is introduced a novel space-time RLS algorithm in which filter coefficients updating and filtering have been well separated by properly taking into account their space-time nature. Specifically, filter coefficients updating is performed intra-frame, *i.e.* updating proceeds following a lexicographical scanning that visits all the symbols within a single frame and the obtained filter coefficients are collected in $\mathbf{f}^{(t-1)}$. On the other hand, the $\mathbf{f}^{(t-1)}$ is instead applied only once-per-frame, *i.e.* the application of the updated filter is *postponed* to the next frame, so that during all the symbol lexicographic scanning no filtering is performed. This novel technique stems from the circumstance that the whole error image computed for the $t-1$-th frame can be held along all the symbol lexicographic scanning of the t-th frame. More in detail, by introducing the symbol image equalized after the $t-1$-th frame has been RLS processed:

$$\hat{s}^{(t/t-1)}[\underline{n}] = [\mathbf{f}^{(t-1)}]^{\mathrm{T}} \cdot \boldsymbol{\gamma}_{y,\underline{n}} \tag{6.17}$$

Then, the whole error image need to conduct the RLS processing on the t-th frame is:

$$e^{(t/t-1)}[\underline{n}] = s^{(t)}[\underline{n}] - \hat{s}^{(t/t-1)}[\underline{n}] \tag{6.18}$$

[1] According to (6.16), denoting the support as $\mathcal{S}_f = \{\underline{n}^{(1)}, \underline{n}^{(2)}, \ldots, \underline{n}^{(C)}\}$, the $p \in S_f$ and $q \in S_f$ element of the matrix $\mathbf{\Gamma}_{y,\underline{n}}^{(t)}$ is:

$$(\mathbf{\Gamma}_{y,\underline{n}}^{(t)})_{p,q} = y[(-\underline{n}^{(q)} \bmod L) + \underline{n}L]\, \overline{y}[(-\underline{n}^{(q)} \bmod L) + \underline{n}L - (\underline{n}^{(p)} - \underline{n}^{(q)})]$$

Table 6.1: Algorithm I: Space-Time-RLS

Time Adaptation

1. $\mathbf{P}^{(t)} = \mathbf{P}^{(t-1)}$
2. $\mathbf{f}_{\underline{n}}^{(t)} = \mathbf{f}_{\underline{n}}^{(t-1)}$

Spatial Adaptation (Single t-th Frame)

1. $\hat{\mathbf{k}}_{\underline{n}} = \lambda^{-1}\mathbf{P}^{(t)} \cdot \boldsymbol{\gamma}_{y,\underline{n}}$
2. $v_{\underline{n}} = \hat{\mathbf{k}}_{\underline{n}}^{\mathrm{T}} \cdot \boldsymbol{\gamma}_{y,\underline{n}}, \quad \mu_{\underline{n}} = (1 + v_{\underline{n}})^{-1}$
3. $\mathbf{k}_{\underline{n}} = \mu_{\underline{n}}\hat{\mathbf{k}}_{\underline{n}}$
4. $\mathbf{P}^{(t)} = \lambda^{-1}\mathbf{P}^{(t)} - \mathbf{k}_{\underline{n}} \cdot \hat{\mathbf{k}}_{\underline{n}}^{\mathrm{T}}$
5. $\hat{s}^{(t)}[\underline{n}] = [\mathbf{f}_{\underline{n}^{(p)}}^{(t)}]^{\mathrm{T}} \cdot \boldsymbol{\gamma}_{y,\underline{n}}$
6. $e^{(t)}[\underline{n}] = s^{(t)}[\underline{n}] - \hat{s}^{(t)}[\underline{n}]$
7. $\mathbf{f}_{\underline{n}}^{(t)} = \mathbf{f}_{\underline{n}^{(p)}}^{(t)} + e^{(t)}[\underline{n}]\,\mathbf{k}_{\underline{n}}$

Next Frame: $t = t + 1$

Bearing (6.17) and (6.18) in mind, the *a posteriori error* needed in step 7 of the Space-Time RLS Algorithm I takes the following form:

$$\begin{aligned} e^{(t)}[\underline{n}] &= s^{(t)}[\underline{n}] - \hat{s}^{(t)}[\underline{n}] = s^{(t)}[\underline{n}] - [\mathbf{f}^{(t)}]^{\mathrm{T}} \cdot \boldsymbol{\gamma}_{y,\underline{n}} \\ &= \mu_{\underline{n}}(s^{(t)}[\underline{n}] - [\mathbf{f}^{(t-1)}]^{\mathrm{T}} \cdot \boldsymbol{\gamma}_{y,\underline{n}}) = \mu_{\underline{n}}\, e^{(t/t-1)}[\underline{n}] \end{aligned} \tag{6.19}$$

Stemming from the *a posteriori* error (6.19), the Space-Time RLS Algorithm I it is modified by separating inter-frame filtering update and intra-frame filter coefficients update as described in the Space-Time RLS Algorithm II.

Table 6.2: Algorithm II: Space-Time-RLS

Time Adaptation

1. $\mathbf{P}^{(t)} = \mathbf{P}^{(t-1)}$
2. $\mathbf{f}_{\underline{n}}^{(t)} = \mathbf{f}_{\underline{n}}^{(t-1)}$

Spatial Adaptation (Single th-Frame)

1. $\hat{\mathbf{k}}_{\underline{n}} = \lambda^{-1}\mathbf{P}^{(t)} \cdot \boldsymbol{\gamma}_{y,\underline{n}}$
2. $v_{\underline{n}} = \hat{\mathbf{k}}_{\underline{n}}^{\mathrm{T}} \cdot \boldsymbol{\gamma}_{y,\underline{n}}, \quad \mu_{\underline{n}} = (1 + v_{\underline{n}})^{-1}$
3. $\mathbf{k}_{\underline{n}} = \mu_{\underline{n}}\,\hat{\mathbf{k}}_{\underline{n}}$
4. $\mathbf{P}^{(t)} = \lambda^{-1}\mathbf{P}^{(t)} - \mathbf{k}_{\underline{n}} \cdot \hat{\mathbf{k}}_{\underline{n}}^{\mathrm{T}}$
5. $\mathbf{f}^{(t)} = \mathbf{f}^{(t)} + \mu_{\underline{n}} e^{(t/t-1)}[\underline{n}]\,\mathbf{k}_{\underline{n}}$

Next Frame: $t = t + 1$

Postponed Filtering

1. $\hat{s}^{(t/t-1)}[\underline{n}] = (f^{(t-1)} * y^{(t)})[\underline{n}]$
2. $e^{(t/t-1)}[\underline{n}] = s^{(t)}[\underline{n}] - \hat{s}^{(t/t-1)}[\underline{n}]$

It is worth noting that during the space coefficients updating phase only the error updating $e^{(t)}[\underline{n}] = \mu_{\underline{n}} e^{(t/t-1)}[\underline{n}]$ is performed, without any unnecessary filtering; the updated filter $\mathbf{f}^{(t)}$ is applied only once per frame.

Finally, both the RLS algorithms are initialized as follows:

1. $\mathbf{f}^{(0)} = \delta_f$
2. $\hat{s}^{(0)}[\underline{n}] = (f^{(0)} * y^{(0)})[\underline{n}]$
3. $e^{(0)}[\underline{n}] = \tilde{s}^{(0)}[\underline{n}] - \hat{s}^{(0)}[\underline{n}]$
4. $\mathbf{P}^{(\mathbf{0})} = \epsilon \mathbf{I}$

where $\delta_{\mathbf{f}}$ is a vector with only a single element different from zero and ϵ is a small initialization value. Moreover, the RLS Algorithm II starts with $\mu_{\underline{0}} = 1$.

As any RLS algorithm, differently than LMS, convergence does not depend on the input correlation matrix eigenvalue spread, *i.e.* it fastly converges even when the eigenvalue spread is large. On the other hand, this value is paid with an increased computational complexity in comparison with the LMS algorithm; we report in Tab.6.3 the computation complexity of RMS and LMS algorithm evaluated in the case at hand. It is worth to highlight that since the two-dimensional RLS algorithm is more complex than the LMS one, it is very interesting to investigate on sparse equalizer supports with reduced cardinality in order to mitigate the overall number of filtering operation.

Table 6.3: Computational Complexity: C is the cardinalty of the equalizer support $\mathcal{S}_f$.

	ST-RLS	PF-ST-RLS	LMS
flop	$O(NC(C+2+S_I))$	$O(NC(C+2)+(S_I C)))$	$O(NC)$

6.1.4 Nonlinear Symbol Estimation

Apart from the initial frames dedicated to training, the symbols $s[\underline{n}]$ are not available at receiver. The so-called Decision Directed (DD) technique substitutes "true" symbols with those obtained through hard-detection of the equalized signal. It is also well-known that such a hard-estimation based technique does not guarantee global convergence while satisfactory results are obtained replacing the hard-estimation with the soft-estimation given by the nonlinear unconditional MMSE estimate, which here takes the following form:

$$\begin{aligned}\tilde{s} = \mathrm{E}\left\{s|\hat{s}\right\} &= \int_S s\, p_{S|\hat{S}}(s|\hat{s})p_{\mathrm{s}}(\mathbf{s}), ds \\ &= \frac{\displaystyle\int_S s\, p_{\hat{S}|S}(\hat{s}|s)p_{\mathrm{s}}(\mathbf{s})ds}{\displaystyle\int_S p_{\hat{S}|S}(\hat{s}|s)p_{\mathrm{s}}(\mathbf{s})ds}\end{aligned} \tag{6.20}$$

Very interestingly, differently from the case of natural image restoration [122], in our OCC scenario the nonlinear estimate (6.20) can take fully advantage of the *a priori* probabilistic description of the transmitted symbols, see [123],[124].[2]

For OOK transmission, the MMSE estimator (6.20) is:

$$\frac{\tilde{s}}{A} = -\left[1 - \exp\left(\frac{2\hat{s}/A}{\mathrm{NSR}}\right)\right]\left[1 + \exp\left(\frac{2\hat{s}/A}{\mathrm{NSR}}\right)\right]^{-1} \tag{6.21}$$

[2]At convergence $R_{\hat{s}y}[\underline{m}] = \alpha R_{sy}[\underline{m}]$, this condition means that $s[\underline{n}]$ belongs to the class of Bussgang processes and hence the equalization scheme is called "Bussgang Equalization". A generalization of Bussgang Theorem is found in [125],[126].

where $A \in \{-1, 1\}$,[3] $\mathrm{NSR} = \sigma_w^2/\sigma_s^2$ is the noise-to-signal ratio and σ_w^2 measures the variance of the residual ISI plus noise measured at the equalizer output.

6.1.5 Semiblindness

The adaptive SFSE can be synthesized also in a semiblind fashion since the nonlinear MMSE estimate (6.20) can be replaced by known symbols when these latter are available. In OCC systems with mobile receivers, the presence of known symbols is not limited to initial synchronization frames, where all the symbols can be used to drive the RLS convergence, but is needed for the important task of detection and alignment of the region of interest. Hence, a fraction of training symbols can be used also in frames dedicated to information transmission.

In particular, it is considered a cornice of white training symbols added to the transmitted image (see Fig. 6.4). This is useful for several reasons: i) allows for the identification of the region of interest when transmitter and receiver are not aligned; ii) allows for estimating the NSR thus enabling a proper adaptation of the nonlinearity (6.20); iii) allows to avoid the estimation of the symbols on the cornice, which are the most difficult to equalize since they are isolated on the image border.

6.2 Numerical Results

In this Section it is discussed the SFSE estimation accuracy through numerical simulations. In particular, it is considered the transmission trough an optical channel whose finite impulse response has the following bidimensional Gaussian shape:

$$h[n_1, n_2] = \frac{\exp(-\frac{1}{2}[n_1\, n_2]\mathbf{K}^{-1}[n_1\, n_2]^T)}{2\pi\sigma_1\sigma_2\sqrt{1-\rho^2}}$$
$$\mathbf{K} = \begin{bmatrix} \sigma_1^2 & \rho\,\sigma_1\sigma_2 \\ \rho\,\sigma_1\sigma_2 & \sigma_2^2 \end{bmatrix} \tag{6.22}$$

This is a very frequently encountered channel model in image processing for both out-of-focus as well as moving blur. Moreover, in OCC systems the blur introduced by the camera lens is usually modeled as a bidimensional

[3]This follows mapping the non-negative values $0 - 255$ of the received signal $y[\underline{n}]$ to the interval $[-1, 1]$.

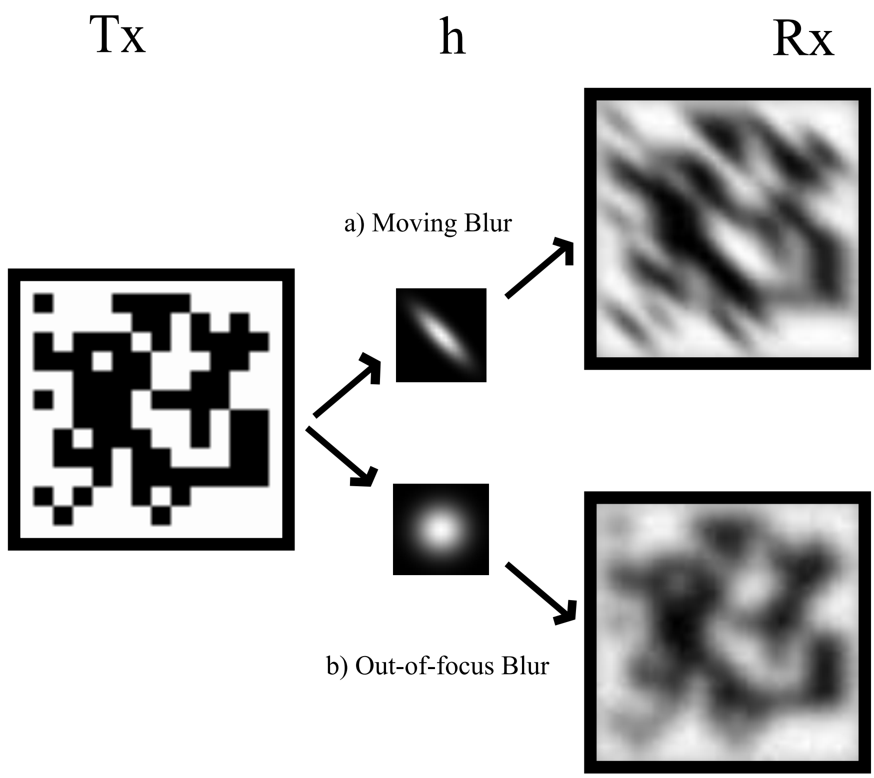

Fig. 6.4: Example of the transmitted (Tx) and received (Rx) images for both a) moving and b) out-of-focus blur.

Gaussian shaped function, as described in [127–129] where the blur is discussed in terms of LED sources spatial interference. In particular, the contribution of the n-th LED source to the received signal-to-noise power ratio is given by:

$$\mathrm{SNR}_n = P_n^{(\mathrm{T})} \sum_{i,j} \frac{Q_n^2(i,j)}{P^{(\mathrm{SN})}(i,j)} \tag{6.23}$$

In (6.23), $P_n^{(\mathrm{T})}$ is the squared optical power transmitted by the n-th LED source, $P^{(\mathrm{SN})}(i,j)$ is the shot noise power and Q_n is the channel DC gain [129] for the camera pixel (i,j):

$$Q_n(i,j) = \frac{(m+1)A_{lens}}{2\pi d^2} cos(\psi) cos^m(\phi) c_n(i,j) \tag{6.24}$$

where ϕ is the angle of irradiance, ψ is the angle of incidence, m is the Lambertian order that characterizes the light beam directivity, and $c_n(i,j)$

is the concentration ratio given by:

$$c_n(i,j) = \frac{4}{\pi}\left[\frac{f}{d}\frac{l_n}{s} + \frac{\sqrt{\sigma_1\sigma_2}}{s}\right]^{-2} I_n(i,j) \tag{6.25}$$

where s, f, l_n respectively are the camera pixel edge length, the camera focal length and the size of the n-th transmit element and

$$I_n(i,j) = \begin{cases} 1 & \forall (i - i_n^{(\mathrm{ref})})^2 + (j - j_n^{(\mathrm{ref})})^2 \le \left[\frac{fl_n}{2sd} + \frac{\sqrt{\sigma_1\sigma_2}}{2s}\right]^2 \\ 0 & \text{otherwise} \end{cases}$$

The blur used in the experiments has a size such that one symbol interferes with the surrounding 8 others.

6.2.1 Synthetic experiments

To evaluate the estimation accuracy of the proposed equalizer numerical experiments are carried out in The Mathworks MATLAB/Simulink® computer programming framework. The image has dimension $70{\times}70$ pixels, the transmitted symbols per frame are $12{\times}12$ and the fractional sampling rate is $L = 5$. If not differently specified along the experiments, the signal-to-noise ratio (SNR) measured at the channel output is fixed to $30\mathrm{dB}$.
In the next figures is plotted the Bit Error Rate (BER), averaged over 500 MonteCarlo runs, obtained by our proposed semiblind adaptive Bussgang SFSE; if not different specified, two synchronization frames are used for training the equalizer at the beginning of the transmission.

In Fig. 6.5 the case of out-of-focus blur is considered or different levels of the AWGN power. It is possible to appreciate that our scheme reduces the BER close to the ideal AWGN channel limit after 8 frames for $\mathrm{SNR} = 40\mathrm{dB}$ and after 9 frames for $\mathrm{SNR} = 35\mathrm{dB}$, *i.e.* when SNR is higher than $30\mathrm{dB}$, the AWGN does not affect the effectiveness of the equalization. Instead, as expected, for low SNR scenarios performance get worse, but still, compared to the initial condition, a significant improvement is present.

In Fig.6.6 and Fig.6.7, the presented semiblind adaptive Bussgang SFSE is compared with the ideal Fully Trained (FT) equalizer, in which all the transmitted symbols are used for training, and the blind DD equalizer, all using the novel Postponed Filtering Space-Time RLS algorithm; also shown is the case of totally blind equalization in which the synchronization frames are not used. In particular, Fig. 6.6 refers to a high SNR scenario where all

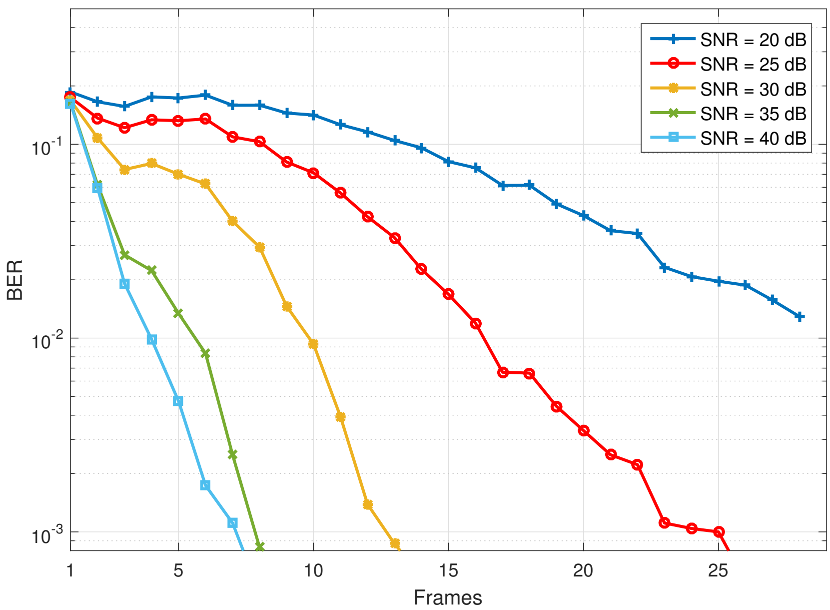

Fig. 6.5: BER comparison for different values of SNR. Out-of-Focus blur.

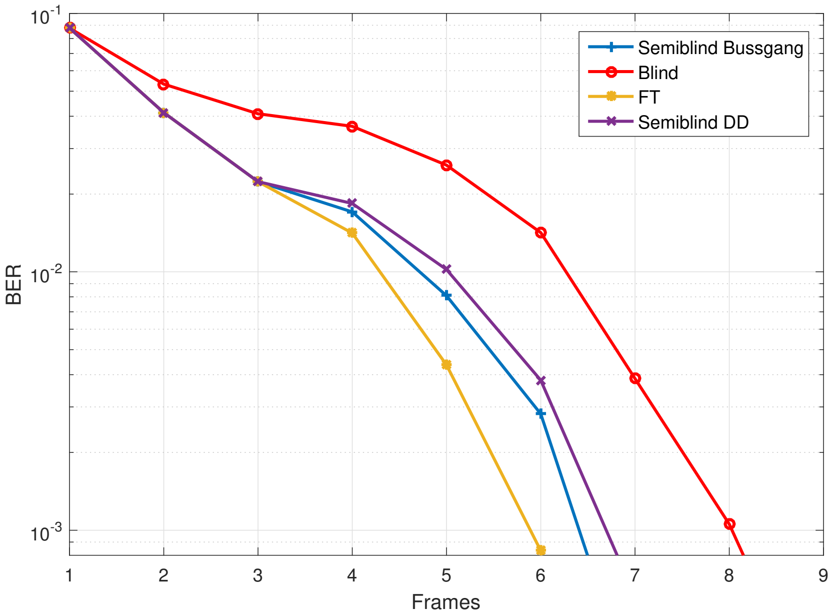

Fig. 6.6: Our semiblind space-time PF-RLS Bussgang equalizer is compared, in a high SNR scenario, with the fully trained space-time PF-RLS, the blind space-time PF-RLS DD and the semiblind space-time PF-RLS DD equalizers.

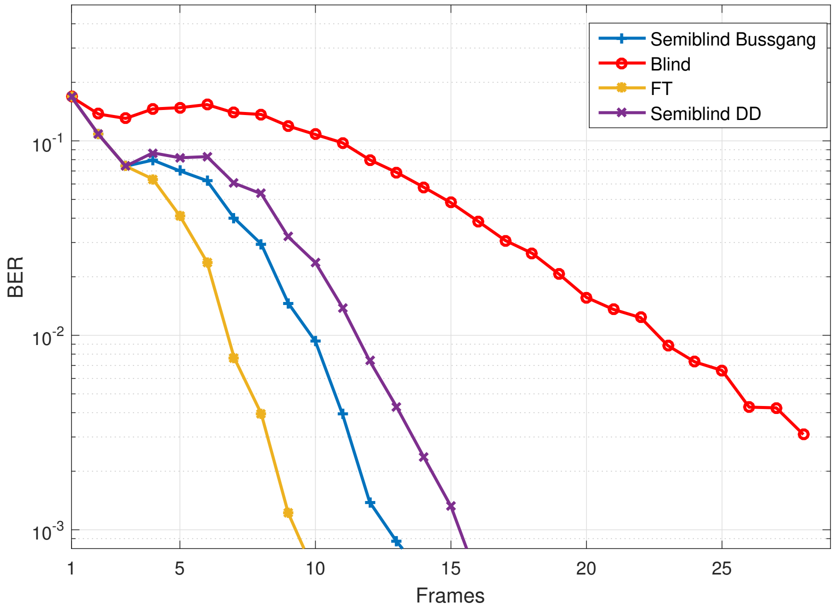

Fig. 6.7: Our semiblind space-time PF-RLS Bussgang equalizer is compared, in a low SNR scenario, with the fully trained space-time PF-RLS, the blind space-time PF-RLS DD and the semiblind space-time PF-RLS DD equalizers.

the equalizers reach a BER of 10^{-3} in less than 9 frames; in detail, the proposed equalizer obtains the same result of FT one frame later. Interestingly enough, in this case even the totally blind approach is able to open the receiver eye. Instead, in the low SNR scenario of Fig.6.7 the convergence of the totally blind equalizer is significantly slower than the others; in this figure it is also appreciated the accuracy worsening of the DD equalizer.

Finally, in Fig. 6.8 the estimation accuracy of the Bussgang and DD equalizers are compared with the estimation accuracy of the LMS adapted semiblind DD equalizer and the blind DD equalizer. As expected, the LMS adaptation get worst performance *w.r.t.* RLS. It is possible to see that the LMS algorithm can not succeed in the suppression of the spatial interference. Moreover, it is evident that using the pure blind DD equalizer without training frames it is not possible to improve the BER.

In Fig.6.9 the learning curves of the Mean Square Error (MSE) measured at the equalizer output are presented.

$$\text{MSE} = E\{(s^{(t)}[\underline{n}] - \hat{s}^{(t)}[\underline{n}])^2\}$$

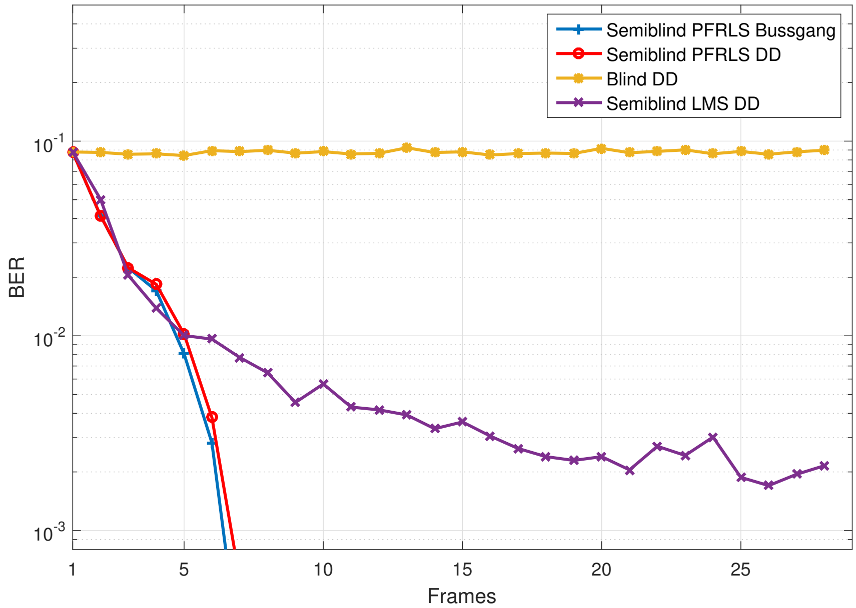

Fig. 6.8: Under out-of-focus blur, our semiblind space-time PF-RLS Bussgang equalizer is compared with semiblind space-time PF-RLS DD, the semiblind LMS DD equalizer and the totally blind DD equalizer.

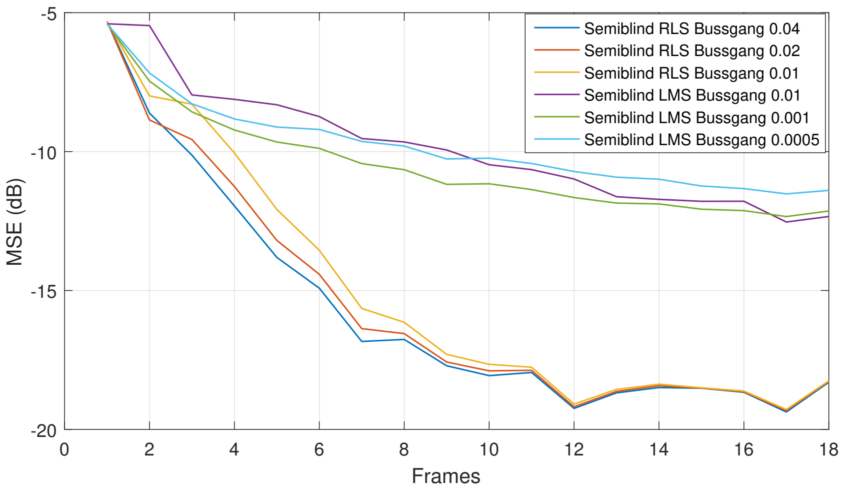

Fig. 6.9: MSE learning curves of Semiblind LMS Bussgang equalizer for various learning rates values and Semiblind RLS Bussgang equalizer for various initialization values.

In Fig. 6.9 that refers to the same scenario of Fig. 6.8 considering different initialization value ϵ of the inverse covariance matrix $\mathbf{P}^{(0)}$. In particular, it can be appreciated that the parameter ϵ has impact only on the initial transient phase, while convergence is still reached at iteration frame 12 for all the three values of ϵ. Moreover, a comparison with the LMS algorithm is provided using different learning rates. It is well appreciated that the RLS algorithm, differently than the LMS one, convergence is independent of the input correlation matrix eigenvalue spread. From a communication prospective, it is interesting to note also that even if the convergence is reached at the frame 12, the point in which the detection can be considered successful, e.g. FEC threshold BER 10^{-3}, is reached few frames earlier.

6.2.2 Sparse FIR Support

Given the high resolution obtained by the fractional sampling at receiver, reduction of computational complexity achieved by FIR equalizers having sparse support $\mathcal{S}_f$ is worth to be addressed.

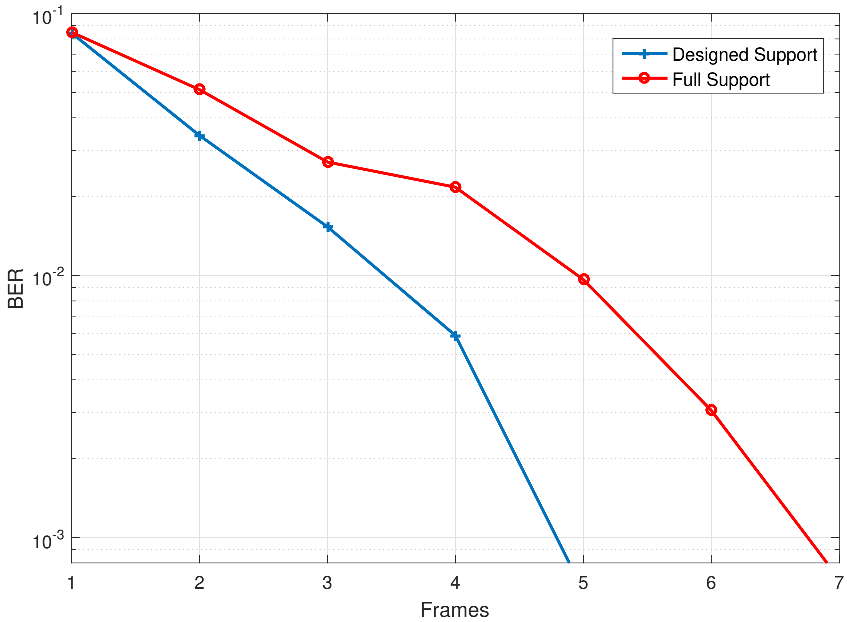

Fig. 6.10: Comparison between full support and reshaped support under moving blur interference.

To this regard, Fig. 6.10 reports the BER obtained in the case of moving blur optical channel of Fig.6.4. We compared two of the presented semiblind SFSE, one using the full support of 19×19 pixels, the other using the support depicted in Fig.6.3. Notice that the blur shape can be easily inferred looking at the autocorrelation of the signal $y[\underline{n}]$.

Interestingly enough, using a sparse support yields better performance; this is explained because using a filter with too many coefficients slows the convergence of the algorithm. Moreover, the equalization is more accurate because only the pixels carrying the most useful information about the inter-symbol spatial interference are selected in the support $\mathcal{S}_f$.

Chapter 7

Conclusion

VLC represents a new frontier of communication, paving the way for new opportunities in the information and communication technology sector. It is a *green* form of communication, which reduces electromagnetic pollution and energy consumption, especially where it is possible to provide illumination and data transfer at the same time.

Throughout this thesis several research challenges have been investigated. The primary objective of LEDs is to provide illumination service, so that the light could bring data in an indiscernible way. This has motivated the need of studying modulation techniques that provides good luminous efficiency and good color rendering index. In this thesis has been investigated a CSK modulation in which the good color rendering properties of the constellation used it is granted by transmitting a combination of colors that are metameric equivalent. At the same time the data rate of the transmission has been improved also considering the time domain. CPPM modulation has been merged with CSK to guarantee good temporal illumination property, as well as to neglect dimming and flickering issues that can arise when high cardinality PPM modulation is used. In fact, in such a modulation, within a symbol period, there is a considerable amount of time in which the signal is equal to zero, *i.e.* high PAPR. The receiver is based on a single photodiode (rather than three) with a bank of pass-band filters able to detect colors that have a different power spectral distribution but are metamerically equivalent, while the CPPM is based on timebased matched filters. The studies on multicolored (RGB) LEDs has been extended to the case in which every color carries interdependent steam of data, studying the inter-color (self) interference, and applying an equalizer that reduces the effect of self-interference and, at the same time, it uses interference for detection since it carries also useful information. Moreover, test results have been provided with an Arduino board.

Indoor positioning, using light, is an emerging application, that can boost indoor location-based services as personalized marketing advertising, precise indoor navigation or augmented intelligence. A centralized visible light localization scheme has been presented, using a lateration positioning algorithm that is an hybrid linear combination of RSS and TDOA, which leads to a system that is more resilient to the presence of different impairments, such as the possibility of having channel multipath effect that generates overlapped pulses, or amplitude fluctuations, *i.e.* shadowing, due to the presence of noise. Numerical results show that positioning estimation in the order of cm can be reached with the system presented.

Thanks to the directivity of the light transmitters, with the knowledge of the indoor users position it is possible to understand which LED will give them connection, and which not. So it is possible to apply a spatial division multiplexing to reduce interference and to adapt the number of transmitting elements, *i.e.* the degree of freedom of the MIMO technique used. For this reason the localization task is important also to improve the MIMO communication performances. In this thesis has been presented a MIMO-PPM scheme based on STBC under the constraint of matrices to be trace orthogonal (TO-STBC). The TOSTBC architecture aims at finding the trade-off between a low BER and a high data rate without requiring a complex hardware implementation.

Last, it has been exploited the intrinsic fractionally sampled nature of OCC images, in order to directly equalize the blur introduced by the optical channel. So it has been presented a novel system architecture for OCC equalization, which reduces the spatial intersymbol interference occurring when multiple transmitters are used and the received images are affected by blur. Numerical results shown that using the semiblind adaptive fractionally spaced FIR equalizer presented in chapter 6, BER values that tends to zero can be obtained after few transmitted frame for both out-of-focus and moving blur.

Appendix A

Published Papers

A.1 Journal Papers

J-4 S. Pergoloni, M. Biagi, S. Colonnese, R. Cusani and G. Scarano, "*Optimized LEDs Footprinting for Indoor Visible Light Communication Networks,*" in IEEE Photonics Technology Letters, vol. 28, no. 4, pp. 532-535, Feb.15, 15 2016.

J-3 M. Biagi, S. Pergoloni and A. M. Vegni, "*LAST: A Framework to Localize, Access, Schedule, and Transmit in Indoor VLC Systems,*" in Journal of Lightwave Technology, vol. 33, no. 9, pp. 1872-1887, May.1, 1 2015.

J-2 M. Biagi, A. M. Vegni, S. Pergoloni, P. M. Butala and T. D. C. Little, "*Trace-Orthogonal PPM-Space Time Block Coding Under Rate Constraints for Visible Light Communication,*" in Journal of Lightwave Technology, vol. 33, no. 2, pp. 481-494, Jan.15, 15 2015.

J-1 S. Pergoloni, M. Biagi, S. Rinauro, S. Colonnese, R. Cusani and G. Scarano, "*Merging Color Shift Keying and Complementary Pulse Position Modulation for Visible Light Illumination and Communication,*" in Journal of Lightwave Technology, vol. 33, no. 1, pp.

A.2 Conference Proceedings

C-8 S. Pergoloni, M. Biagi, S. Colonnese, R. Cusani and G. Scarano, "*Camera Communication Deblurring: a Semiblind Spatial Fractionally-Spaced Adaptive Equalizer with Flexible Filter Support Design,*" 2016 International Conference on Image Processing Theory, Tools and Applications (IPTA), Oulu, Finland, pp. 0-0.

C-7 S. Pergoloni, M. Biagi, S. Colonnese, R. Cusani and G. Scarano, "*Coverage optimization of 5G atto-cells for visible light communications access,*" 2015 IEEE International Workshop on Measurements & Networking (M&N), Coimbra, 2015, pp. 1-5.

C-6 S. Pergoloni, M. Biagi, S. Colonnese, G. Scarano and R. Cusani, "*On the mutual information of the VLC channel in the presence of external ambient lighting,*" 2015 IEEE 14th Canadian Workshop on Information Theory (CWIT), St. John's, NL, 2015, pp. 139-142.

C-5 A. Petroni, S. Pergoloni, M. Biagi, S. Colonnese, R. Cusani and G. Scarano, "*Adaptive PPM Acoustic Detection in very Shallow Water Reservoir,*" OCEANS 2015 - MTS/IEEE Washington, Washington, DC, 2015, pp. 1-4.

C-4 A. Petroni, S. Pergoloni, M. Biagi, S. Colonnese, R. Cusani and G. Scarano, "*Acoustic bathymetric mapping in very shallow water reservoir,*" OCEANS 2015 - MTS/IEEE Washington, Washington, DC, 2015, pp. 1-4.

C-3 M. Biagi, S. Rinauro, S. Colonnese, S. Pergoloni, G. Scarano and R. Cusani, "*Trace-orthogonal pulse position modulation space time block coding for underwater links,*" 2014 Oceans - St. John's, St. John's, NL, 2014, pp. 1-5.

C-2 M. Biagi, S. Rinauro, S. Colonnese, S. Pergoloni, R. Cusani and G. Scarano, "*Near-sea multi-target opportunistic multiple-input multiple-output detection,*" 2014 Oceans - St. John's, St. John's, NL, 2014, pp. 1-5.

C-1 S. Pergoloni, M. Biagi, S. Colonnese, R. Cusani and G. Scarano, "*Merging Color Shift Keying and complementary Pulse Position Modulation for visible light illumination and communication,*" 2014 Euro Med Telco Conference (EMTC), Naples, 2014, pp. 1-6.

Bibliography

[1] S. Dimitrov and H. Haas, *Principles of LED Light Communications: Towards Networked Li-Fi*. Cambdrige university press, 2015.

[2] T. Komine and M. Nakagawa, "Fundamental analysis for visible-light communication system using LED lights," *Consumer Electronics, IEEE Transactions on*, vol. 50, no. 1, pp. 100–107, Feb 2004.

[3] J. M. Kahn and J. R. Barry, "Wireless infrared communications," *Proceedings of the IEEE*, vol. 85, no. 2, pp. 265–298, February 1997.

[4] P. M. Butala, J. C. Chau, and T. D. C. Little, "Metameric modulation for diffuse visible light communications with constant ambient lighting," in *2012 International Workshop on Optical Wireless Communications (IWOW)*, Oct 2012, pp. 1–3.

[5] S. Rajagopal, R. D. Roberts, and S. K. Lim, "Ieee 802.15.7 visible light communication: modulation schemes and dimming support," *IEEE Communications Magazine*, vol. 50, no. 3, pp. 72–82, March 2012.

[6] M. Noshad and M. Brandt-Pearce, "Application of expurgated ppm to indoor visible light communications part i: Single-user systems," *Journal of Lightwave Technology*, vol. 32, no. 5, pp. 875–882, March 2014.

[7] C. H. Yeh, Y. F. Liu, C. W. Chow, Y. Liu, P. Y. Huang, and H. K. Tsang, "Investigation of 4-ASK modulation with digital filtering to increase 20 times of direct modulation speed of white-light LED visible light communication system," *Opt. Express*, vol. 20, no. 15, pp. 16 218–16 223, Jul 2012. [Online]. Available: http://www.opticsexpress.org/abstract.cfm?URI=oe-20-15-16218

[8] G. Ntogari, T. Kamalakis, and T. Sphicopoulos, "Performance analysis of space time block coding techniques for indoor optical wireless systems," *Selected Areas in Communications, IEEE Journal on*, vol. 27, no. 9, pp. 1545 –1552, december 2009.

[9] W. Popoola, E. Poves, and H. Haas, "Spatial pulse position modulation for optical communications," *Lightwave Technology, Journal of*, vol. 30, no. 18, pp. 2948 –2954, sept.15, 2012.

[10] C. Abou-Rjeily and W. Fawaz, "Space-time codes for mimo ultra-wideband communications and mimo free-space optical communications with ppm," *Selected Areas in Communications, IEEE Journal on*, vol. 26, no. 6, pp. 938–947, 2008.

[11] N. Saha, M. S. Ifthekhar, N. T. Le, and Y. M. Jang, "Survey on optical camera communications: challenges and opportunities," *IET Optoelectronics*, vol. 9, no. 5, pp. 172–183, 2015.

[12] R. Gregory, *Eye and Brain: The Psychology of Seeing*, ser. McGraw-Hill paperbacks. McGraw-Hill, 1978. [Online]. Available: https://books.google.it/books?id=0ZNqAAAAMAAJ

[13] A. B. Watson, "Temporal sensitivity," *Handbook of perception and human performance*, vol. 1, pp. 6–1, 1986.

[14] D. H. Kelly, "Visual responses to time-dependent stimuli.∗ i. amplitude sensitivity measurements†," *J. Opt. Soc. Am.*, vol. 51, no. 4, pp. 422–429, Apr 1961. [Online]. Available: http://www.osapublishing.org/abstract.cfm?URI=josa-51-4-422

[15] A. K. Jain, *Fundamentals of Digital Image Processing*. Prentice-Hall, Inc., 1989.

[16] G. Scarano, *Elaborazione delle Immagini*, 2013.

[17] Z. Ghassemlooy, W. Popoola, and S. Rajbhandari, *Optical Wireless Communications: System and Channel Modelling with MATLAB*. CRC publisher, USA, August 2012.

[18] "Ieee standard for local and metropolitan area networks–part 15.7: Short-range wireless optical communication using visible light," *IEEE Std 802.15.7-2011*, pp. 1–309, Sept 2011.

[19] V. Jungnickel, V. Pohl, S. Nonnig, and C. von Helmolt, "A physical model of the wireless infrared communication channel," *IEEE Journal on Selected Areas in Communications*, vol. 20, no. 3, pp. 631–640, Apr 2002.

[20] R. Ramirez-Iniguez, S. M. Idrus, and Z. Sun, *Optical Wireless Communications*. CRC Press, 2008.

[21] H. L. Minh, D. O'Brien, G. Faulkner, L. Zheng, K. Lee, D. Jung, Y. Oh, and E. T. Won, "100-mb/s nrz visible light communications using a postequalized white led," *IEEE Photonics Technology Letters*, vol. 21, no. 15, pp. 1063–1065, 2009.

[22] J. Ding, C. L. I, and Z. Xu, "Indoor optical wireless channel characteristics with distinct source radiation patterns," *IEEE Photonics Journal*, vol. 8, no. 1, pp. 1–15, Feb 2016.

[23] "http://visiblelightcomm.com/top-10-visible-light-communications-applications/."

[24] G. Cossu, A. M. Khalid, P. Choudhury, R. Corsini, and E. Ciaramella, "3.4 gbit/s visible optical wireless transmission based on rgb led," *Opt. Express*, vol. 20, no. 26, pp. B501–B506, Dec 2012. [Online]. Available: http://www.opticsexpress.org/abstract.cfm?URI=oe-20-26-B501

[25] Y. Wang, R. Li, Y. Wang, and Z. Zhang, "3.25-gbps visible light communication system based on single carrier frequency domain equalization utilizing an rgb led," in *OFC 2014*, March 2014, pp. 1–3.

[26] R. Drost and B. Sadler, "High precision indoor positioning using lighting led and image sensor," in *Computer and Information Technology (ICCIT), 2011 14th International Conference on*, Dec 2011, pp. 309–314.

[27] E. Monteiro and S. Hranilovic, "Constellation design for color-shift keying using interior point methods," in *2012 IEEE Globecom Workshops*, Dec 2012, pp. 1224–1228.

[28] ——, "Design and implementation of color-shift keying for visible light communications," *Journal of Lightwave Technology*, vol. 32, no. 10, pp. 2053–2060, May 2014.

[29] S. Pergoloni, M. Biagi, S. Rinauro, S. Colonnese, R. Cusani, and G. Scarano, "Merging color shift keying and complementary pulse position modulation for visible light illumination and communication," *Journal of Lightwave Technology*, vol. 33, no. 1, pp. 192–200, Jan 2015.

[30] E. A. Lee and D. G. Messerschmitt, *Digital Communication, 2nd ed.* Kluwer, 1994.

[31] M. Rahaim, T. Borogovac, and J. B. Carruthers, "CandLES: Communications and lighting emulation software," in *Proc. of the fifth*

ACM International Workshop on Wireless Network Testbeds, Experimental Evaluation and Characterization. ACM, 2010.

[32] J. B. Carruthers, S. M. Carroll, and P. Kannan, "Propagation modelling for indoor optical wireless communications using fast multi-receiver channel estimation," *Optoelectronics, IEE Proceedings*, vol. 150, no. 5, pp. 473–481, 2003.

[33] J. R. Barry, *Wireless Infrared Communications*. Kluwer, 1994.

[34] M. Biagi, T. Borogovac, and T. D. C. Little, "Adaptive receiver for indoor visible light communications," *Journal of Lightwave Technology*, vol. 31, no. 23, pp. 3676–3686, Dec 2013.

[35] G. Cossu, A. M. Khalid, P. Choudhury, R. Corsini, and E. Ciaramella, "3.4 gbit/s visible optical wireless transmission based on RGB LED," *Opt. Express*, vol. 20, no. 26, pp. B501–B506, Dec 2012. [Online]. Available: http://www.opticsexpress.org/abstract.cfm?URI=oe-20-26-B501

[36] F.-M. Wu, C.-T. Lin, C.-C. Wei, C.-W. Chen, Z.-Y. Chen, and K. Huang, "3.22-gb/s WDM visible light communication of a single RGB LED employing carrier-less amplitude and phase modulation," in *Optical Fiber Communication Conference/National Fiber Optic Engineers Conference 2013*. Optical Society of America, 2013, p. OTh1G.4. [Online]. Available: http://www.osapublishing.org/abstract.cfm?URI=OFC-2013-OTh1G.4

[37] OSRAM, *LEDs, New Light Sources for Display Backlighting Application Note*. OSRAM TLT, 2015. [Online]. Available: http://www.osram-os.com/Graphics/XPic2/00102586_0.pdf

[38] S. Rodriguez Perez, R. Perez Jimenez, O. B. Gonzalez Hernandez, J. A. Rabadan Borges, and B. Rodriguez Mendoza, "Concentrator and lens models for calculating the impulse response on IR-wireless indoor channels using a ray-tracing algorithm," *Microwave and Optical Technology Letters*, vol. 36, no. 4, pp. 262–267, 2003. [Online]. Available: http://dx.doi.org/10.1002/mop.10738

[39] Luxeon Star LEDs, *Rebel LEDs datasheet*. Luxeon Star LEDs, 2016. [Online]. Available: http://www.luxeonstar.com/luxeon-rebel-leds

[40] TELSTORE, *C7718 data sheet*. TELSTORE, 2016.

[41] Vishay, *Vishay BpW34 data sheet*. Vishay, 2016. [Online]. Available: http://www.vishay.com/docs/81521/bpw34.pdf

[42] M. Rahaim, T. Borogovac, and J. B. Carruthers, "CandLES: Communications and lighting emulation software," in *WiNTECH '10: Proceedings of the fifth ACM international workshop on Wireless network testbeds, experimental evaluation and characterization*. ACM, 2010.

[43] H. Liu, H. Darabi, P. Banerjee, and J. Liu, "Survey of wireless indoor positioning techniques and systems," *IEEE Transactions on Systems, Man, and Cybernetics, Part C (Applications and Reviews)*, vol. 37, no. 6, pp. 1067–1080, Nov 2007.

[44] A. Jovicic, J. Li, and T. Richardson, "Visible light communication: opportunities, challenges and the path to market," *IEEE Communications Magazine*, vol. 51, no. 12, pp. 26–32, December 2013.

[45] A. Hiyama, J. Yamashita, H. Kuzuoka, K. Hirota, and M. Hirose, "Position tracking using infra-red signals for museum guiding system," in *Proceedings of the Second International Conference on Ubiquitous Computing Systems*, ser. UCS'04. Springer-Verlag, 2005, pp. 49–61.

[46] M. Hazas and A. Hopper, "Broadband ultrasonic location systems for improved indoor positioning," *Mobile Computing, IEEE Transactions on*, vol. 5, no. 5, pp. 536–547, May 2006.

[47] S. Mazuelas, A. Bahillo, R. Lorenzo, P. Fernandez, F. Lago, E. Garcia, J. Blas, and E. Abril, "Robust indoor positioning provided by real-time rssi values in unmodified wlan networks," *Selected Topics in Signal Processing, IEEE Journal of*, vol. 3, no. 5, pp. 821–831, Oct 2009.

[48] B. Alavi and K. Pahlavan, "Modeling of the toa-based distance measurement error using uwb indoor radio measurements," *Communications Letters, IEEE*, vol. 10, no. 4, pp. 275–277, Apr 2006.

[49] S. Beauregard, Widyawan, and M. Klepal, "Indoor pdr performance enhancement using minimal map information and particle filters," in *Position, Location and Navigation Symposium, 2008 IEEE/ION*, May 2008, pp. 141–147.

[50] M. Angermann and P. Robertson, "Footslam: Pedestrian simultaneous localization and mapping without exteroceptive sensors," *Proceedings of the IEEE*, vol. 100, no. Special Centennial Issue, pp. 1840–1848, May 2012.

[51] C. Fischer, K. Muthukrishnan, M. Hazas, and H. Gellersen, "Ultrasound-aided pedestrian dead reckoning for indoor navigation," in *Proceedings of the First ACM International Workshop on Mobile Entity Localization and Tracking in GPS-less Environments*, ser. MELT '08. New York, NY, USA: ACM, 2008, pp. 31–36. [Online]. Available: http://doi.acm.org/10.1145/1410012.1410020

[52] M. Addlesee, R. Curwen, S. Hodges, J. Newman, P. Steggles, A. Ward, and A. Hopper, "Implementing a sentient computing system," *Computer*, vol. 34, no. 8, pp. 50–56, Aug 2001.

[53] J. Nah, R. Parthiban, and M. Jaward, "Visible light communications localization using tdoa-based coherent heterodyne detection," in *Photonics (ICP), 2013 IEEE 4th International Conference on*, Oct 2013, pp. 247–249.

[54] S.-Y. Jung, S. Hann, and C.-S. Park, "Tdoa-based optical wireless indoor localization using led ceiling lamps," *Consumer Electronics, IEEE Transactions on*, vol. 57, no. 4, pp. 1592–1597, November 2011.

[55] S.-H. Yang, E.-M. Jeong, D.-R. Kim, H.-S. Kim, Y.-H. Son, and S.-K. Han, "Indoor three-dimensional location estimation based on led visible light communication," *Electronics Letters*, vol. 49, no. 1, pp. 54–56, January 2013.

[56] ——, "Three-dimensional localization based on visible light optical wireless communication," in *Ubiquitous and Future Networks (ICUFN), 2013 Fifth International Conference on*, July 2013, pp. 468–469.

[57] S.-Y. Jung, C.-K. Choi, S. H. Heo, S. R. Lee, and C.-S. Park, "Received signal strength ratio based optical wireless indoor localization using light emitting diodes for illumination," in *Consumer Electronics (ICCE), 2013 IEEE International Conference on*, Jan 2013, pp. 63–64.

[58] Y. Kim, J. Hwang, J. Lee, and M. Yoo, "Position estimation algorithm based on tracking of received light intensity for indoor visible light communication systems," in *Ubiquitous and Future Networks (ICUFN), 2011 Third International Conference on*, June 2011, pp. 131–134.

[59] D. Iturralde, C. Azurdia-Meza, N. Krommenacker, I. Soto, Z. Ghassemlooy, and N. Becerra, "A new location system for an underground mining environment using visible light communications," in *Communication Systems, Networks Digital Signal Processing (CSNDSP), 2014 9th International Symposium on*, July 2014, pp. 1165–1169.

[60] P. Hu, L. Li, C. Peng, G. Shen, and F. Zhao, "Pharos: Enable physical analytics through visible light based indoor localization," in *Twelfth ACM Workshop on Hot Topics in Networks (HotNets-XII)*, 2013.

[61] M. S. Rahman, M. M. Haque, and K.-D. Kim, "Location-based services: Back to the future," *International Journal of Electrical and Computer Engineering (IJECE)*, vol. 1, no. 2, pp. 161–170, December 2011.

[62] M. Rahman, M. Haque, and K.-D. Kim, "High precision indoor positioning using lighting led and image sensor," in *Computer and Information Technology (ICCIT), 2011 14th International Conference on*, Dec 2011, pp. 309–314.

[63] C. Sertthin, E. Tsuji, M. Nakagawa, S. Kuwano, and K. Watanabe, "A Switching Estimated Receiver Position Scheme for Visible Light Based Indoor Positioning System," in *Proc. of 4th Intl. Conf. on Wireless Pervasive Computing*, Melbourne, Australia, February 2009, pp. 64–68.

[64] H.-S. Kim, D.-R. Kim, S.-H. Yang, Y.-H. Son, and S.-K. Han, "Mitigation of inter-cell interference utilizing carrier allocation in visible light communication system," *Communications Letters, IEEE*, vol. 16, no. 4, pp. 526–529, April 2012.

[65] P. Rutten, "Wideband optical position sensor with normalization," Aug. 16 2012, uS Patent App. 13/261,267. [Online]. Available: http://www.google.com/patents/US20120206735

[66] M. Biagi, S. Pergoloni, and A. M. Vegni, "Last: A framework to localize, access, schedule, and transmit in indoor vlc systems," *Journal of Lightwave Technology*, vol. 33, no. 9, pp. 1872–1887, May 2015.

[67] M. Biagi, T. Borogovac, and T. Little, "Adaptive receiver for indoor visible light communications," *Lightwave Technology, Journal of*, vol. 31, no. 23, pp. 3676–3686, Dec 2013.

[68] E. D. Kaplan and C. J. Hegarty, *Understanding GPS: principles and applications, 2nd Edition*. Artech House Mobile Communications Series, 2006, ch. Concept of ranging using TOA measurements.

[69] B. Cheng, R. Hudson, F. Lorenzelli, L. Vandenberghe, and K. Yao, "Distributed gauss-newton method for node localization in wireless sensor networks," in *Signal Processing Advances in Wireless Communications, 2005 IEEE 6th Workshop on*, June 2005, pp. 915–919.

[70] K. E. Atkinson, *An Introduction to Numerical Analysis*. John Wiley & Sons, Inc, 1989.

[71] E. Baccarelli, M. Biagi, C. Pelizzoni, and N. Cordeschi, "Optimal mimo uwb-ir transceiver for nakagami-fading and poisson-arrivals," *Journal of Communications*, vol. 3, no. 1, 2008. [Online]. Available: http://ojs.academypublisher.com/index.php/jcm/article/view/03012740

[72] S. Pergoloni, M. Biagi, S. Colonnese, R. Cusani, and G. Scarano, "Optimized leds footprinting for indoor visible light communication networks," *IEEE Photonics Technology Letters*, vol. 28, no. 4, pp. 532–535, Feb 2016.

[73] M. Biagi, A. M. Vegni, and T. D. C. Little, "LAT Indoor MIMO-VLC –Localize, Access and Transmit–," in *Proc. of Intl. Workshop on Optical Wireless Communications (IWOW 2012)*, Pisa, Italy, October 22 2012.

[74] J. Vucic, C. Kottke, S. Nerreter, K. Langer, and J. Walewski, "513 Mbit/s visible light communications link based on dmt-modulation of a white led," *Journal of Lightwave Technology*, vol. 28, no. 24, 2010.

[75] J. Vucic, C. Kottke, K. Habel, and K.-D. Langer, "803 Mbit/s Visible Light WDM Link based on DMT Modulation of a Single RGB LED Luminary," in *Optical Fiber Communication Conference and Exposition (OFC/NFOEC) and the National Fiber Optic Engineers Conference*, March 2011.

[76] J. Armstrong and B. Schmidt, "Comparison of asymmetrically clipped optical ofdm and dc-biased optical ofdm in awgn," *Communications Letters, IEEE*, vol. 12, no. 5, pp. 343–345, 2008.

[77] L. Chen, B. Krongold, and J. Evans, "Performance analysis for optical ofdm transmission in short-range im/dd systems," *Lightwave Technology, Journal of*, vol. 30, no. 7, pp. 974–983, 2012.

[78] M. Biagi, A. Vegni, and T. Little, "LAT Indoor MIMO-VLC –Localize, Access and Transmit–," in *Proc. of Intl. Workshop on Optical Wireless Communications*, Pisa, Italy, October 22 2012.

[79] P. Butala, H. Elgala, and T. Little, "Sample Indexed Spatial Orthogonal Frequency Division Multiplexing ," *Chinese Optics Letters (to appear)* , vol. 12, 2014.

[80] S. M. Hass, S. J. H., and V. Tarokh, “Space-time codes for wireless optical communications,” *EURASIP Journal of Applied Signal Processing*, vol. 3, pp. 211–220, 2002.

[81] T. Fath and H. Haas, “Performance Comparison of MIMO Techniques for Optical Wireless Communications in Indoor Environments,” *IEEE Transactions on Communications*, vol. 61, pp. 733–742, February 2013.

[82] P. Butala, H. Elgala, and T. Little, “Performance of Optical Spatial Modulation and Spatial Multiplexing with Imaging Receiver,” in *IEEE WCNC'14*, Istanbul, Turkey, April 2014.

[83] M. Di Renzo, H. Haas, A. Ghrayeb, S. Sugiura, and L. Hanzo, “Spatial modulation for generalized mimo: Challenges, opportunities, and implementation,” *Proceedings of the IEEE*, vol. 102, no. 1, pp. 56–103, Jan 2014.

[84] J. Esch, “Prolog to "spatial modulation for generalized mimo: Challenges, opportunities, and implementation",” *Proceedings of the IEEE*, vol. 102, no. 1, pp. 53–55, Jan 2014.

[85] T. Fath and H. Haas, “Optical Spatial Modulation using Colour LEDs,” in *IEEE ICC 2013 - Optical Networks and Systems*, June 2013, pp. 3938–3942.

[86] A. Burton, H. L. Minh, Z. Ghassemlooy, E. Bentley, and C. Botella, “Experimental demonstration of 50-mb/s visible light communications using 4 $, times,$ 4 mimo,” *Photonics Technology Letters, IEEE*, vol. 26, no. 9, pp. 945–948, May 2014.

[87] F.-M. Wu, C.-T. Lin, C.-C. Wei, C.-W. Chen, H.-T. Huang, and C.-H. Ho, “1.1-gb/s white-led-based visible light communication employing carrier-less amplitude and phase modulation,” *Photonics Technology Letters, IEEE*, vol. 24, no. 19, pp. 1730–1732, Oct 2012.

[88] A. Khalid, G. Cossu, R. Corsini, M. Presi, and E. Ciaramella, “1 gbit/s visible light communication link based on phosphorescent white led,” in *Photonics in Switching (PS), 2012 International Conference on*, Sept 2012, pp. 1–3.

[89] J.-h. Choi, E.-b. Cho, Z. Ghassemlooy, S. Kim, and C. Lee, “Visible light communications employing ppm and pwm formats for simultaneous data transmission and dimming,” *Optical*

and Quantum Electronics, pp. 1–14, 2014. [Online]. Available: http://dx.doi.org/10.1007/s11082-014-9932-0

[90] D. Gesbert, M. Shafi, D. shan Shiu, P. Smith, and A. Naguib, "From Theory to Practice: An Overview of MIMO Space-Time Coded Wireless Systems," *IEEE J. Sel. Areas Commun.*, vol. 21, pp. 281–302, April 2003.

[91] C. Abou-Rjeily and M. Bkassiny, "Unipolar space-time codes with reduced decoding complexity for th-uwb with ppm," *Wireless Communications, IEEE Transactions on*, vol. 8, no. 10, pp. 5086–5095, 2009.

[92] C. Abou-Rjeily, "Orthogonal space-time block codes for binary pulse position modulation," *Communications, IEEE Transactions on*, vol. 57, no. 3, pp. 602–605, 2009.

[93] C. Abou-Rjeily and Z. Baba, "Achieving full transmit diversity for ppm constellations with any number of antennas via double position and symbol permutations," *Communications, IEEE Transactions on*, vol. 57, no. 11, pp. 3235–3238, 2009.

[94] V. Tarokh, N. Seshadri, and A. R. Calderbank, "Space-time codes for high data rate wireless communication: performance criterion and code construction," *IEEE Trans. Inf. Theor.*, vol. 44, no. 2, pp. 744–765, Sep. 2006. [Online]. Available: http://dx.doi.org/10.1109/18.661517

[95] M. Safari and M. Uysal, "Do we really need ostbcs for free-space optical communication with direct detection?" *Wireless Communications, IEEE Transactions on*, vol. 7, no. 11, pp. 4445–4448, 2008.

[96] X. Song and J. Cheng, "Subcarrier intensity modulated mimo optical communications in atmospheric turbulence," *Optical Communications and Networking, IEEE/OSA Journal of*, vol. 5, no. 9, pp. 1001–1009, Sept 2013.

[97] E. Bayaki and R. Schober, "On space-time coding for free-space optical systems," *Trans. Comm.*, vol. 58, no. 1, pp. 58–62, Jan. 2010. [Online]. Available: http://dx.doi.org/10.1109/TCOMM.2010.01.080142

[98] M. Biagi, A. M. Vegni, S. Pergoloni, P. M. Butala, and T. D. C. Little, "Trace-orthogonal ppm-space time block coding under rate constraints for visible light communication," *Journal of Lightwave Technology*, vol. 33, no. 2, pp. 481–494, Jan 2015.

[99] A. Vegni and M. Biagi, "An indoor localization algorithm in a small-cell led-based lighting system," in *Indoor Positioning and Indoor Navigation (IPIN), 2012 International Conference on*, Nov 2012, pp. 1–7.

[100] R. M. R. Mesleh, H. Helgala and H.Haas, "Performance of optical spatial modulation with transmitters-receivers alignment," *IEEE Communication Letters*, vol. 15, no. 1, pp. 79–81, 2011.

[101] S. Barbarossa, "Trace-orthogonal design of mimo systems with simple scalar detectors, full diversity and (almost) full rate," in *Signal Processing Advances in Wireless Communications, 2004 IEEE 5th Workshop on*, 2004, pp. 308–312.

[102] A. K. Jain, *Fundamentals of Digital Image Processing*. Prentice Hall, 1989.

[103] J. Armstrong, Y. Sekercioglu, and A. Neild, "Visible light positioning: a roadmap for international standardization," *Communications Magazine, IEEE*, vol. 51, no. 12, pp. 68–73, December 2013.

[104] T. Yamazato, I. Takai, H. Okada, T. Fujii, T. Yendo, S. Arai, M. Andoh, T. Harada, K. Yasutomi, K. Kagawa, and S. Kawahito, "Image-sensor-based visible light communication for automotive applications," *Communications Magazine, IEEE*, vol. 52, no. 7, pp. 88–97, July 2014.

[105] C. Danakis, M. Afgani, G. Povey, I. Underwood, and H. Haas, "Using a cmos camera sensor for visible light communication," in *Globecom Workshops (GC Wkshps), 2012 IEEE*, Dec 2012, pp. 1244–1248.

[106] R. Roberts, "A mimo protocol for camera communications (camcom) using undersampled frequency shift on-off keying (ufsook)," in *Globecom Workshops (GC Wkshps), 2013 IEEE*, Dec 2013, pp. 1052–1057.

[107] R. Boubezari, H. L. Minh, Z. Ghassemlooy, A. Bouridane, and A. Pham, "Data detection for smartphone visible light communications," in *Communication Systems, Networks Digital Signal Processing (CSNDSP), 2014 9th International Symposium on*, July 2014, pp. 1034–1038.

[108] T. Nguyen, N. T. Le, and Y. M. Jang, "Practical design of screen-to-camera based optical camera communication," in *Information Networking (ICOIN), 2015 International Conference on*, Jan 2015, pp. 369–374.

[109] B. W. Kim, H. C. Kim, and S. Y. Jung, "Display field communication: Fundamental design and performance analysis," *Journal of Lightwave Technology*, vol. 33, no. 24, pp. 5269–5277, Dec 2015.

[110] G. Jacovitti, G. Panci, and G. Scarano, "Bussgang-zero crossing equalization: an integrated hos-sos approach," *Signal Processing, IEEE Transactions on*, vol. 49, no. 11, pp. 2798–2812, Nov 2001.

[111] L. Tong, G. Xu, and T. Kailath, "Blind identification and equalization based on second-order statistics: a time domain approach," *Information Theory, IEEE Transactions on*, vol. 40, no. 2, pp. 340–349, Mar 1994.

[112] C. Papadias and D. Slock, "Fractionally spaced equalization of linear polyphase channels and related blind techniques based on multichannel linear prediction," *Signal Processing, IEEE Transactions on*, vol. 47, no. 3, pp. 641–654, Mar 1999.

[113] G. Giannakis and R. Heath, "Blind identification of multichannel fir blurs and perfect image restoration," *Image Processing, IEEE Transactions on*, vol. 9, no. 11, pp. 1877–1896, Nov 2000.

[114] G. Panci, P. Campisi, S. Colonnese, and G. Scarano, "Multichannel blind image deconvolution using the bussgang algorithm: spatial and multiresolution approaches," *Image Processing, IEEE Transactions on*, vol. 12, no. 11, pp. 1324–1337, Nov 2003.

[115] G. Giannakis and S. Halford, "Blind fractionally spaced equalization of noisy fir channels: direct and adaptive solutions," *Signal Processing, IEEE Transactions on*, vol. 45, no. 9, pp. 2277–2292, Sep 1997.

[116] S. Rajagopal, R. Roberts, and S.-K. Lim, "IEEE 802.15.7 visible light communication: modulation schemes and dimming support," *Communications Magazine, IEEE*, vol. 50, no. 3, pp. 72–82, March 2012.

[117] S. J. Orfanidis, *Optimum Signal Processing*. McGraw-Hill, 2007.

[118] E. Eleftheriou and D. Falconer, "Tracking properties and steady-state performance of rls adaptive filter algorithms," *IEEE Transactions on Acoustics, Speech, and Signal Processing*, vol. 34, no. 5, pp. 1097–1110, Oct 1986.

[119] A. M. Sequeira and C. W. Therrien, "A new 2-d fast rls algorithm," in *Acoustics, Speech, and Signal Processing, 1990. ICASSP-90., 1990 International Conference on*, Apr 1990, pp. 1401–1404 vol.3.

[120] M. Muneyasu, E. Uemoto, and T. Hinamoto, “A novel 2-d adaptive filter based on the 1-d rls algorithm,” in *Circuits and Systems, 1997. ISCAS '97., Proceedings of 1997 IEEE International Symposium on*, vol. 4, Jun 1997, pp. 2317–2320 vol.4.

[121] M. Chellali and V. K. Ingle, “Adaptive image restoration using the multichannel recursive least squares algorithm,” in *Acoustics, Speech, and Signal Processing, 1991. ICASSP-91., 1991 International Conference on*, Apr 1991, pp. 2521–2524 vol.4.

[122] S. Colonnese, P. Campisi, G. Panci, and G. Scarano, “Blind image deblurring driven by nonlinear processing in the edge domain,” *EURASIP Journal on Advances in Signal Processing*, vol. 2004, no. 16, pp. 1–14, 2004.

[123] A. Neri, G. Scarano, and G. Jacovitti, “Bayesian iterative method for blind deconvolution,” pp. 196–208, 1991. [Online]. Available: http://dx.doi.org/10.1117/12.49777

[124] G. Panci, S. Colonnese, P. Campisi, and G. Scarano, “Blind equalization for correlated input symbols: A bussgang approach,” *Trans. Sig. Proc.*, vol. 53, no. 5, pp. 1860–1869, May 2005. [Online]. Available: http://dx.doi.org/10.1109/TSP.2005.845477

[125] G. Scarano, “Cumulant series expansion of hybrid nonlinear moments of complex random variables,” *IEEE Transactions on Signal Processing*, vol. 39, no. 4, pp. 1001–1003, Apr 1991.

[126] G. Scarano, D. Caggiati, and G. Jacovitti, “Cumulant series expansion of hybrid nonlinear moments of /et,” *IEEE Transactions on Signal Processing*, vol. 41, no. 1, pp. 486–, Jan 1993.

[127] N. T. Le, M. A. Hossain, C. H. Hong, T. Nguyen, T. Le, and Y. M. Jang, “Effect of blur gaussian in mimo optical camera communications,” in *Information and Communication Technology Convergence (ICTC), 2015 International Conference on*, Oct 2015, pp. 1371–1374.

[128] Y. Ohira, S. Arai, T. Yendo, T. Yamazato, H. Okada, T. Fujii, and K. Kamakura, “Novel demodulation scheme based on blurred images for image-sensor-based visible light communication,” in *2015 IEEE Globecom Workshops (GC Wkshps)*, Dec 2015, pp. 1–6.

[129] A. Ashok, M. Gruteser, N. Mandayam, and K. Dana, “Characterizing multiplexing and diversity in visual mimo,” in *Information Sciences*

and Systems (CISS), 2011 45th Annual Conference on, March 2011, pp. 1–6.